ELECTRONIC TRANSPORT OF GRAPHENE DEVICES

SHIN YOUNGJUN

(*B. Sc, (Hons), Sungkyunkwan University*)

A THESIS SUBMITTED

FOR THE DEGREE OF DOCTOR OF PHILOSOPHY

DEPARTMENT OF ELECTRICAL AND COMPUTER ENGINEERING

NATIONAL UNIVERSITY OF SINGAPORE

2012

DECLARATION

I hereby declare that the thesis is my original work and it has been written by me in its entirety. I have duly acknowledged all the sources of information which have been used in the thesis.

This thesis has also not been submitted for any degree in any university previously.

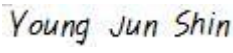

SHIN Youngjun

22 December 2012

Acknowledgements

I cannot believe that I am writing acknowledgements for my thesis at this moment. I would like to thank all those people who made this thesis possible for last 5 years in NUS.

First and foremost, I would like to acknowledge my supervisor, Professor Hyunsoo Yang. He was not only my academic advisor but also life advisor. He always had open mind to discuss everything with all students. His passion for exploring new scientific world inspired me a lot. Without his constant supports and encouragements, I could not finish my long journey as PhD candidate.

I would like to thank my other supervisor, Professor Charanjit Singh Bhatia. Thanks to him, I had a great experience of international collaboration with Hysitron. He taught me what value I should have to be the best in the world.

I would like to appreciate the support from all members of Nanocore, SEL and COE.

For the work in this thesis, I must give special thanks to collaborators. Dr. Qiu Xupeng helped me using sputtering machine and developing defect-free deposition by sputtering in Chapter 2. I could not investigate the surface properties of graphene without high quality epitaxial graphene samples from Prof Andrew Thye Shen Wee group in Chapter 3. Dr. Yingying Wang from Prof. Zexiang Shen group helped me measuring Raman spectroscopy in Chapter 3 and Raman imaging in Chapter 6. Dr. Kalon Gopinadhan and Kwon Jaehyun helped me so many times with all the electrical characterizations. Especially, Dr. Kalon did all the low temperature capacitance-voltage measurements with me in chapter 5 and gave me all the analytical advices of the role of trap charges for the hysteresis. I also really appreciated that Dr Kai-Tak Lam and Prof. Gengchiau Liang did simulations and gave

me many good theoretical advices in Chapter 4 & 6. I thank Dr Alan Kalitsov for the simulations and his analytical advices in Chapter 5 & 7.

I also really appreciate Professor Ganesh Samudra and Professor Gengchiau Liang serving on my comprehensive and oral QE committee and thank for their helpful comments on my research.

Lastly, I would express my deepest gratitude to my family. Especially, I thank my lovely wife, Hyunkyung Choo for her unconditional supports.

Table of Contents

Summary

This thesis represents mainly investigations of electronic transport of graphene devices. First of all, the surface property of graphene has been studied in order to make better contacts between graphene and metal. To understand the surface property of graphene, the wettability of epitaxial graphene on SiC has been studied by contact angle measurements. A monolayer of epitaxial graphene shows a hydrophobic characteristic and no correlation are found between different layers of graphene and wettability. Upon oxygen plasma treatment, defects are introduced into graphene, and the level of damage is investigated by Raman spectroscopy. There exists a correlation between the level of defects and the contact angle. As more defects are induced, the surface energy of graphene is increased, leading to the hydrophilic nature. Plasma treatment with optimized power and duration has been proposed to control the adhesion properties for contact fabrication.

After understanding surface properties, electrical properties of graphene are investigated. Reproducible current hysteresis is observed when high voltage bias is swept in the graphene channel. We observe that the sequence of hysteresis switching with different types of the carriers, n-type and p-type, is inverted and we propose that charging and discharging effect is responsible for the observed ambipolar switching effect supported by quantum simulations.

After studying ambipolar hysteresis of graphene, we study the hysteresis of the top gated bilayer graphene field effect transistors. Capacitance – gate voltage measurements on top gated bilayer graphene indicate that the origin of hysteresis in the channel resistance is due to charge traps present at the graphene/Al_2O_3 interface with a charging and discharging time constant of ~100 μs. On the other hand, the measured capacitance of graphene between source and drain with source-drain voltage does not show any hysteresis. It is also found that the hysteresis is present even at high vacuum conditions and cryogenic temperatures

indicating that chemical attachment is not the main source of the hysteresis. The hysteresis is not due to Joule heating effect, but is a function of the level of the applied voltage.

The tunneling characteristic of graphene from the two-terminal devices after the breakdown is studied. Negative differential conductance is also observed when a high voltage bias is applied across the graphene channel. The tunneling behavior could be attributed to the formation of nonuniform disordered graphene. We propose that the nonuniform disordered structure can introduce energy barriers in the graphene channel. This hypothesis is supported by the Raman images and the simulated results of the *I-V* characteristics from a one dimensional single-square barrier.

Stochastic transitions between an ohmic like state and an insulator like state in graphene devices are studied. It is found that the topological change in the graphene channel is involved for the observed behavior. Active radicals with an uneven graphene channel cause a local change of electrostatic potential, and simulations based on the self-trapped electron and hole mechanism can account for the observed data. Understanding electrical transport of graphene at room temperature and at high bias voltages is very important for the interconnect and transparent contact applications.

List of Tables

List of Figures

List of Abbreviations

0D: Zero Dimensional

1D: One Dimensional

2D: Two Dimensional

ITO: Indium Tin Oxide

SiO_2: Silicon Dioxide

h-BN: Hexagonal Boron Nitride

CVD: Chemical Vapor Deposition

GHz: Giga Hertz

THz: Tera Hertz

Co_2Si: Cobalt Silicon

Al_2O_3: Aluminum Oxide

FET: Field Effect Transistor

TPa: Tera Pascal

HFET: High Electron Mobility Field Effect Transistor

P: Power

T: Temperature

GaN: Gallium Nitride

MOSFET: Metal Oxide Silicon Field Effect Transistor

CNT: Carbon Nanotube

OLED: Organic Light-Emitting Diode

HOPG: Highly Oriented Pyrolitic Graphite

SiC: Silicon Carbide

LEED: Low Electron Energy Diffraction

PDMS: Polydimethysiloxane

DLC: Diamond-Like Carbon

FWHM: Full Width Half Maximum

PLD: Pulsed Laser Deposition

a-C: Amorphous Carbon

nc-G: Nanocrystalline Graphite

PECVD: Plasma Enhanced Chemical Vapor Deposition

CoFe: Cobalt Iron

MgO: Magnesium Oxide

RF: Radio Frequency

L_a: Correlation length

Ar: Argon

AFM: Atomic Force Microscopy

HF: Hydro Fluorine

UHV: Ultra-High Vacuum

EG: Epitaxial Graphene

MCG: Mechanically Cleaved Graphene

STM: Scanning Tunneling Microscopy

CCD: Charge-Coupled Device

Cr: Chrome

Au: Gold

XPS: X-ray Photoelectron Spectroscopy

TiO_2: Titanium Oxide

CDE: Charging Discharging Effect

LUMO: Lowest Unoccupied Molecular Orbital

HOMO: Highest Occupied Molecular Orbital

R: Resistance

SWCNT: Single-Walled Carbon Nanotube

CNP: Charge Neutrality Point

C_{ox}: Oxide Capacitance

C_Q: Quantum Capacitance

C_{tr}: Trap Capacitance

kHz: Kilo Hertz

MHz: Mega Hertz

DOS: Density of States

E_F: Fermi level

MIT: Metal-Insulator Transitions

SEM: Scanning Electron Microscopy

MST: Metal-Semiconductor Transition

1. Introduction

1.1 Background

Graphene is a flat monolayer of carbon atoms tightly packed into a two-dimensional (2D) honeycomb lattice, and is the mother of all graphitic materials.[1] When graphene is stacked thick enough, it becomes graphite, a three-dimensional structure. Graphene can be wrapped up into 0D bulkyball (or fullerene) or rolled into 1D carbon nanotubes can be seen from Figure 1.1. Conversely, graphene can be made by unzipping carbon nanotubes, C_{60} and exfoliating graphite.[2] Before Andre Geim and Kyota S. Novoselov found graphene by mechanical exfoliation using “Scotch tape”, various methods have been utilized in order to find atomically thin graphite, but all ended in failure.[3] Indeed, the discovery of 2D material itself is amazing because free-standing 2D material on top of non-crystalline substrates had not been expected.[1] The mechanically cleaved graphene is not only atomically thin but also highly crystalline at room temperature. The charming toy born from scotch tape has ignited enthusiasm of scientists and caused an avalanche of graphene experiments.[4-11]

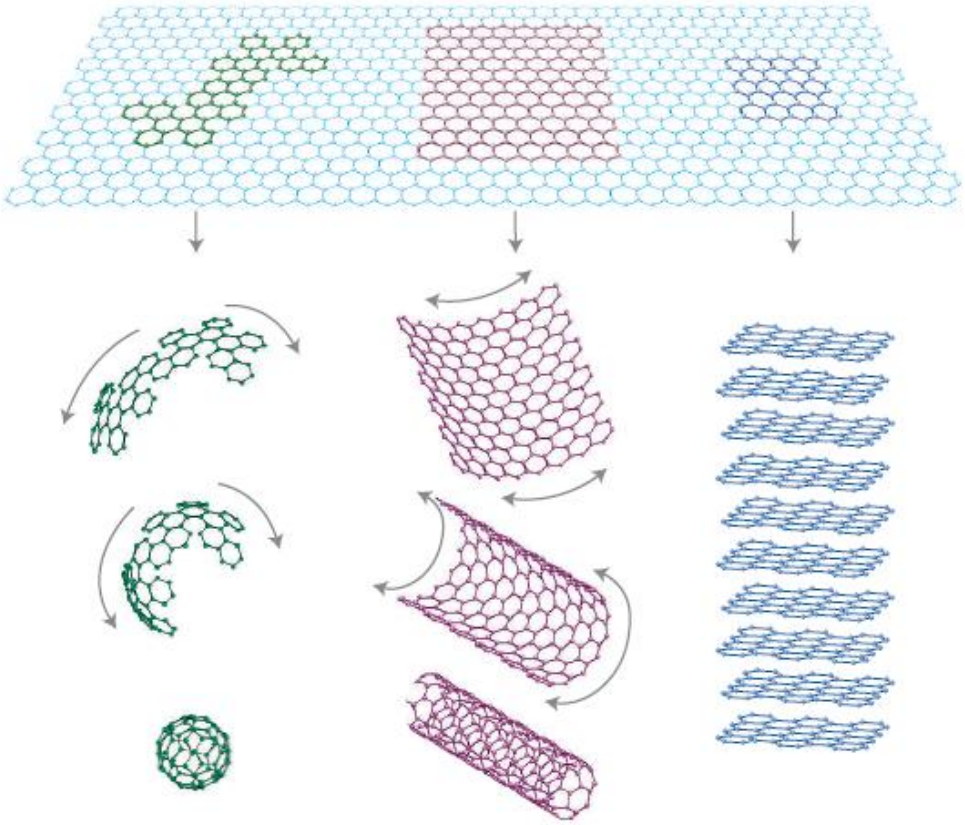

Figure 1.1.1 Mother of all graphitic forms. Graphene is a 2D building materials for carbon materials of all other dimensionalities. [1]

The pioneers, Geim and Novoselove, were motivated by the idea that the high-quality samples always produce new physics. Electrical charge carriers traveling through the chicken-wire web carbon atoms in graphene were very curious as they expected. The electronic properties of graphene are different from those of conventional three-dimensional materials.[6, 10, 12-19] Intrinsic graphene is zero-gap semiconductor (or zero-overlap semimetals) and the effective mass for holes and electrons becomes zero due to graphene's linear dispersion relation.[3] The electrical charge carriers in graphene are astonishingly different from typical electron and hole in conventional materials because of its massless property.[4] Therefore, the electrical property of graphene should be described by quantum electrodynamics rather than by conventional quantum mechanics, although the mobility of graphene is still 300 times slower than the speed of light.[20, 21] Thanks to graphene's novel

properties, relative quantum mechanics are not any more restricted to cosmology or high energy physics which require very expensive and complicated synchrotron, and scientists can play the graphene toy in the laboratory.

Graphene is attractive enough to get attention from other than scientists. Obviously, graphene seduces many engineers who are always thirsty for cheaper, stronger and faster materials for commercialized products. Graphene is very talented and versatile in terms of thermal, chemical, mechanical, optical and electrical properties. First, graphene is a super thermal conductor.[22] The measured thermal conductivity of graphene is 5.3×10^{3} $Wm^{-1}K^{-1}$ which is a many times higher than aluminum. This superior value indicates that graphene can be one of the ideal candidates for heat dissipation materials. Second, graphene is a very elastic and robust material. Breaking strength of graphene is 200 times greater than that of steel.[23] In fact, graphene is the strongest material ever tested. Since graphene is very robust and chemically inert, it can be engineered as the thinnest protection layer for magnetic films in hard disk applications.[24] As mentioned earlier, the mobility of graphene is very fast even at room temperature due to its massless characteristic. Therefore, the most outstanding part of graphene is its electrical property.[25, 26] Graphene is very suitable for radio frequency devices due to its high mobility and can replace indium tin oxide (ITO) by taking advantage of its transparency.[27-30] Graphene is also very suitable metal contacts for flexible electronics due to its outstanding mechanical properties.[31] The better the electrical properties of graphene are understood in terms of engineering, the sooner graphene can be engineered in the electronic world.

1.2 Literature Review

1.2.1 Quantum Electrodynamics

In graphene, each honeycomb structure consists of two equivalent sublattices. Every carbon atom has three nearest neighbors with an interatomic distance 1.42 angstrom and

forms one *s* and three *p* orbitals. The orbitals are hybridized to form three new planar sp^2 orbitals, each containing one electron. These orbitals, held together by sigma-bonds, are responsible for the very rigid hexagonal structure. These sigma-bonds do not contribute to the electrical property of graphene. The remaining *p* orbital perpendicular to the plane formed by the carbon atoms forms π bonds. Graphene has one electron per lattice site because each p_z contributes with one electron. Many unusual electrical properties of graphene are originated from the π orbitals. These interesting characteristics are attributed to the peculiar band structure of graphene, which can be theoretically calculated by the tight-binding approximation method. The primary shape of graphene band structure consists of two conical valleys that touch each other at the symmetry point in the Brillouin zone, called Dirac point or charge neutral point. The energy varies linearly with the magnitude of momentum at this point as can be seen from Fig. 1.2.1.1.[32] Therefore, charge carriers in an ideal graphene sheet behave like massless Dirac fermions. This conical dispersion is minimal at K and K´ points, which coincides with the Fermi level and separates conduction and valence bands, and reveals a zero bandgap and ambipolar electric field effect such that charge carriers can be tuned continuously between electrons and holes in graphene.

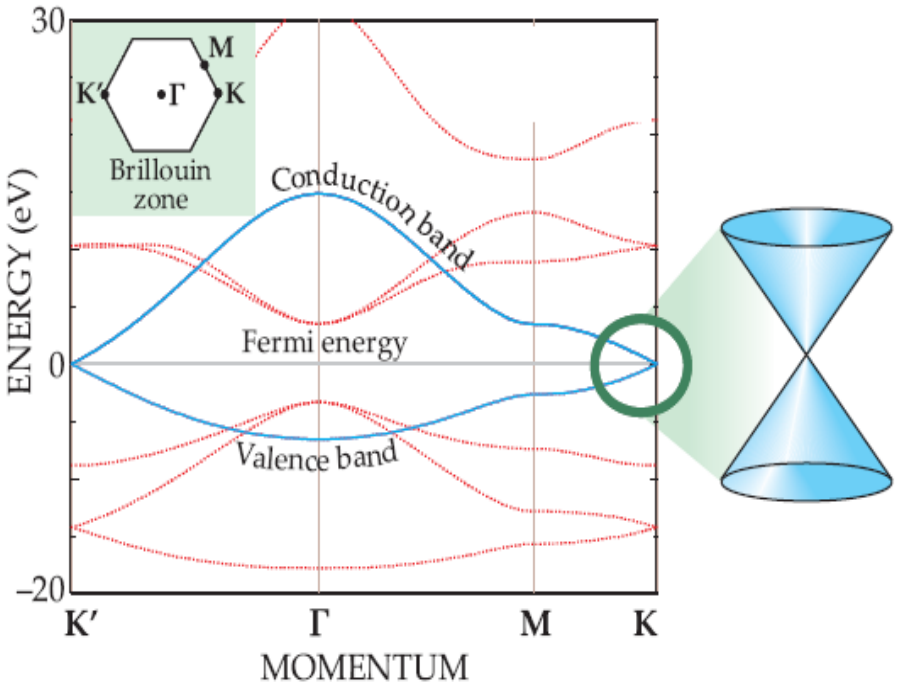

Figure 1.2.1.1 Illustration of valence and conduction band in single layer graphene. [32]

1.2.2 Electrical Properties

The most frequently highlighted advantage of graphene is ultrahigh mobility under ambient conditions. The measured mobility of mechanically exfoliated graphene on top of SiO_2-covered doped silicon wafers is in excess of 15,000 $cm^2V^{-1}s^{-1}$.[17] Upper limits of between 40,000 and 70,000, which are a few hundred times faster than the mobility of silicon, are theoretically proposed.[21, 33] If graphene can be synthesized without any charged impurities and ripples, the predicted mobility is 200,000 $cm^2V^{-1}s^{-1}$ at a carrier density of 10^{12} cm^{-2}.[17] The corresponding resistivity of graphene is 10^{-6} Ω·cm, which is much less than that of silver and is the lowest resistivity ever known at room temperature. By making suspended graphene, the mobility of graphene can be dramatically improved because scattering of graphene's charge carriers by optical phonon of SiO_2 substrates plays a major role in limiting its mobility.[34]

However, suspended graphene is not a fabrication friendly method since the graphene channel is collapsed, when any material is deposited on top of it during fabrication process. By utilizing hexagonal boron nitride (h-BN) as an under layer and a top layer of graphene, the mobility of graphene can be also increased without a suspended structure as seen from Fig. 1.2.2.1 .[35, 36] The h-BN is a very compatible dielectric substrate for graphene devices. It has only 1.7% lattice mismatch with graphite.[37] Furthermore, the energy of surface optical phonon modes of h-BN is two times larger than similar modes in SiO_2.[19] It indicates the chance of enhanced high-temperature and high-field performance of graphene devices with h-BN over typical graphene devices with conventional oxides. It has been reported that the mobility of graphene devices with h-BN bottom layer is three times larger than graphene devices fabricated on top of SiO_2. Moreover, the mobility of graphene excels 100,000 $cm^2V^{-1}s^{-1}$ at a carrier density of 10^{11} cm^{-2} at room temperature, when graphene devices are encapsulated with h-BN.[36]

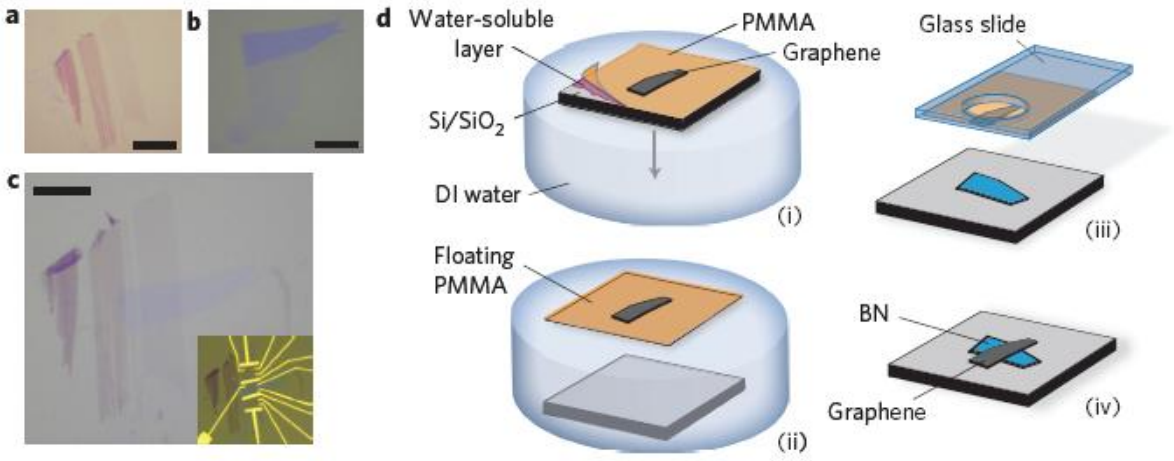

Figure 1.2.2.1 Optical images of graphene (a) and h-BN (b) before and after (c) transfer. Scale bars, 10µm. Inset: electrical contacts. (d) Schematic illustration of the transfer process used to fabricate graphene on h-BN devices. [19]

The mechanically cleaved graphene makes the best quality, but the cleaved graphene cannot be engineered for commercialized products due to its limited size and inefficient method. Therefore, we have to utilize CVD graphene for commercialization and the mobility of CVD graphene should be understood precisely. The mobility of large-scale graphene prepared by roll to roll method is greater than ~ 4000 $cm^2V^{-1}s^{-1}$.[31] However, CVD-based graphene cannot be single crystalline for an entire area, because making a thin copper film without any grain boundary is almost impossible. Graphene grown on the boundary of copper grains is not perfect crystalline.[38] The reported mobility of CVD based graphene is measured in micro scale without including the boundaries among graphene grains. Definitely, the averaged mobility including the boundaries will be much lower than the reported value. Even though large-scale graphene has its drawback, the proto-type of CVD-based and epitaxial graphene transistors shows excellent performance with its high mobility. IBM is a leading group fabricating high performance graphene transistors for radio frequency applications. By taking advantage of graphene's high carrier mobility, they successfully demonstrate a cut-off frequency of 100 GHz made of epitaxial graphene and a cut-off frequency of 155 GHz made of CVD based graphene seen from fig. 1.2.2.2.[27, 29] A higher cut-off frequency is achieved by a self-aligned nanowire gate.[30] It is very important to keep a high mobility to make high-speed transistors, since the cut-off frequency is directly proportional to its mobility. By employing a self-aligned Co_2Si-Al_2O_3 core-shell nanowire top gate, 300 GHz cut-off frequency is achieved as can be seen from 1.2.2.3. If the self-align method can be incorporated with graphene on top of h-BN, 1 THz cut-off frequency might be able to be realized.

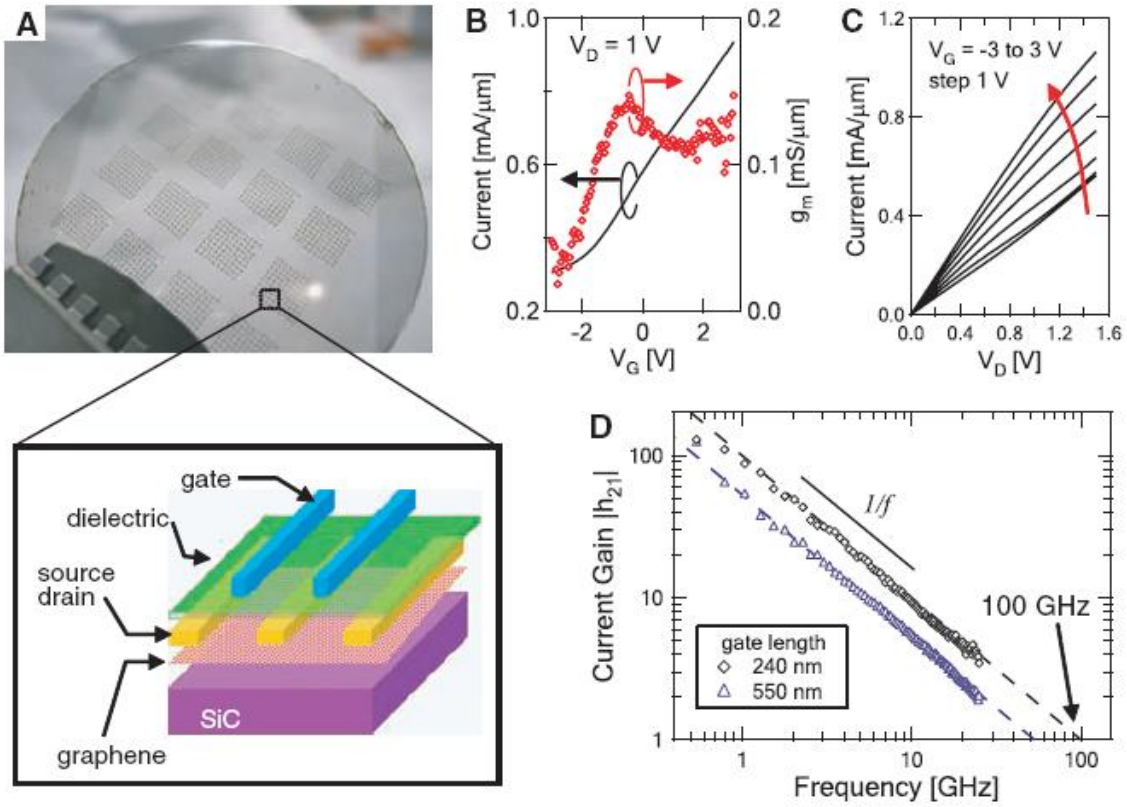

Figure 1.2.2.2 (a) Image of devices fabricated on a 2-inch graphene wafer and schematic cross-sectional view of a top-gated graphene field effect transistor (FET). (b) The drain current, I_D, of a graphene FET (gate length L_G = 240 nm) as a function of gate voltage at drain bias of 1 V with the source electrode grounded. The device transconductance, g_m, is shown on the right axis. (c) The drain current as a function of V_D of a graphene FET (L_G = 240 nm) for various gate voltages. (d) Measured small-signal current gain $|h_{21}|$ as a function of frequency f for a 240-nm-gate (◊) and a 550-nm-gate (Δ) graphene FET at V_D = 2.5 V. Cutoff frequencies, f_T, were 53 and 100 GHz for the 550-nm and 240-nm devices, respectively. [27]

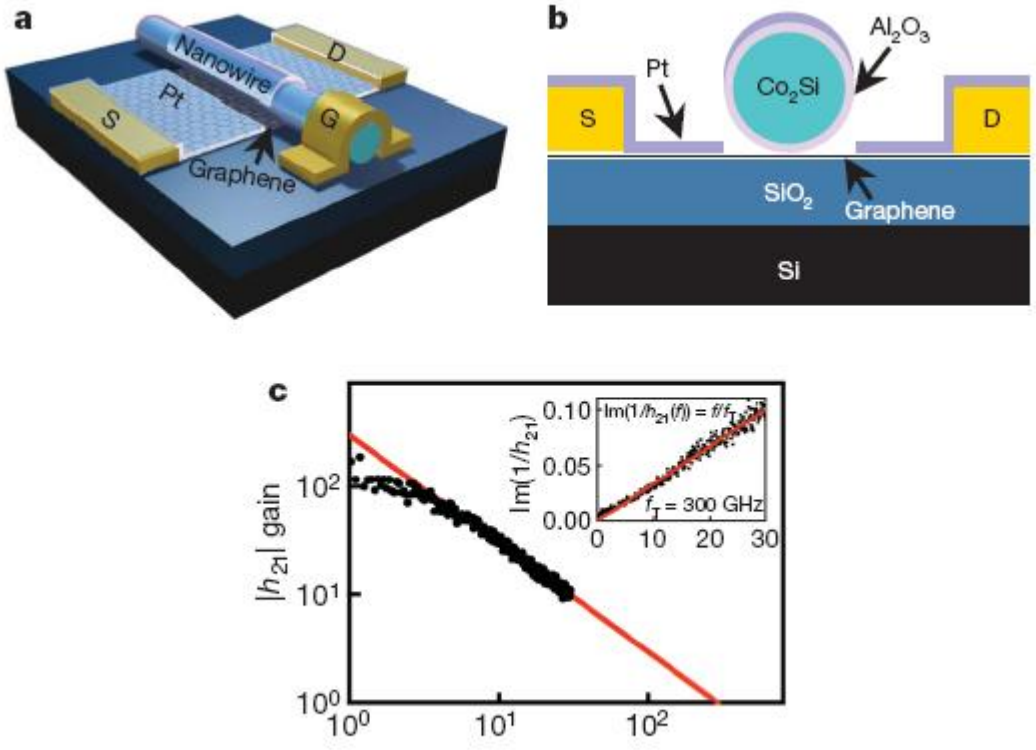

Figure 1.2.2.3 (a) Schematic of the three-dimensional view of the device layout. D, drain; G, gate; S, source. (b) Schematic of the cross-sectional view of the device. (c) Measured small-signal current gain |h21| as a function of frequency *f* at V_{ds}= -1V. Gate length, 144 nm; V_{TG} = 1V. [30]

There is one big barrier for graphene to be utilized as logic devices, because graphene's valence and conduction bands meet at the K points of the Brillouin zone.[4] Transistors fabricated with the graphene channel cannot be turned off, since the band gap is zero. Nevertheless, the band gap of graphene can be opened up with some methods. For example, bilayer graphene's valence and conduction bands are parabolic shape, which is different from the cone-shape of single layer graphene at the K point.[39] A band gap can be opened in bilayer graphene, when the electrical field is applied to perpendicular to bilayer graphene. It is experimentally verified that the conduction and valence bands of bilayer graphene can be transformed from parabolic shape to so called Mexican-hat shape.

Theoretically, the maximum size of bilayer graphene is expected as 250 meV.[44] Engineering bilayer for logic devices is not practical, because we always need to apply dc power in order to turn off the graphene.[14] The most realistic approach to open a band gap of graphene is to constrain graphene to nanoribbons.[40] There are many theoretical calculations for band gaps of zigzag and armchair graphene ribbons, however making precise zigzag and armchair nanoribbons is unavailable with current technology to control the edge of graphene uniformly.[41-43] The graphene nanoribbons with rough edges are fabricated with a width below 10 nm experimentally. The band gap of graphene becomes higher than 200 meV, when the width of graphene ribbons is narrower than 20 nm.[40] However, the cone-shaped conduction and valence band tend to become more parabolic, when the band gap of graphene increases as seen from 1.2.2.3. This means the effective mass of electron and hole increases and the mobility of charge carrier decreases as a result. The experimental results reveal that the mobility of 10 nm wide graphene nanoribbons is less than 200 $cm^2V^{-1}s^{-1}$, which is slower than that of silicon.[40] The measured highest mobility is 1500 $cm^2V^{-1}s^{-1}$ corresponding to 14 nm wide nanoribbons.[44] Although the intrinsic mobility of graphene is very fast, it is very challenging to switch off graphene transistors without losing its high mobility. Nevertheless, it is worthy to develop very narrow graphene ribbons with well-defined edges aiming all-graphene integrated circuits, in which both active and passive devices can be realized with graphene nanoribbons.

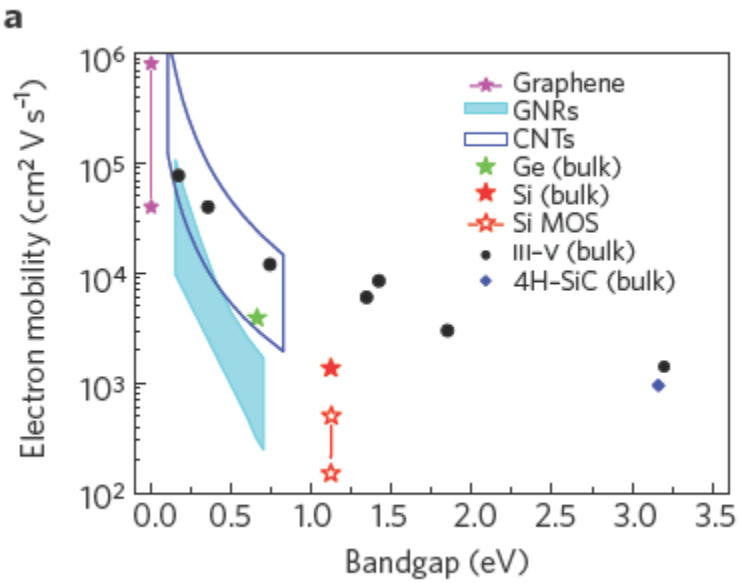

Figure 1.2.2.3 Electron mobility versus bandgap in low electric fields for different materials. [44]

To overcome an insufficient ON/OFF ratio of graphene devices, triode, the first concept of three terminal devices, has been brought back from the history. A graphene variable-barrier "barristor" is realized by engineering atomically sharp interface between graphene and hydrogenated silicon as shown in Fig. 1.2.2.4.[45] By changing the work function of graphene, the barrier's height is adjusted to 0.2 eV thanks to the absence of Fermi-level pinning at the interface. Huge current modulation with an ON/OFF ratio of 10^5 is successfully achieved by controlling the gate voltage to adjust the graphene-silicon Schottky barrier. Logic circuits such as an inverter and a half-adder are demonstrated with graphene barristor.

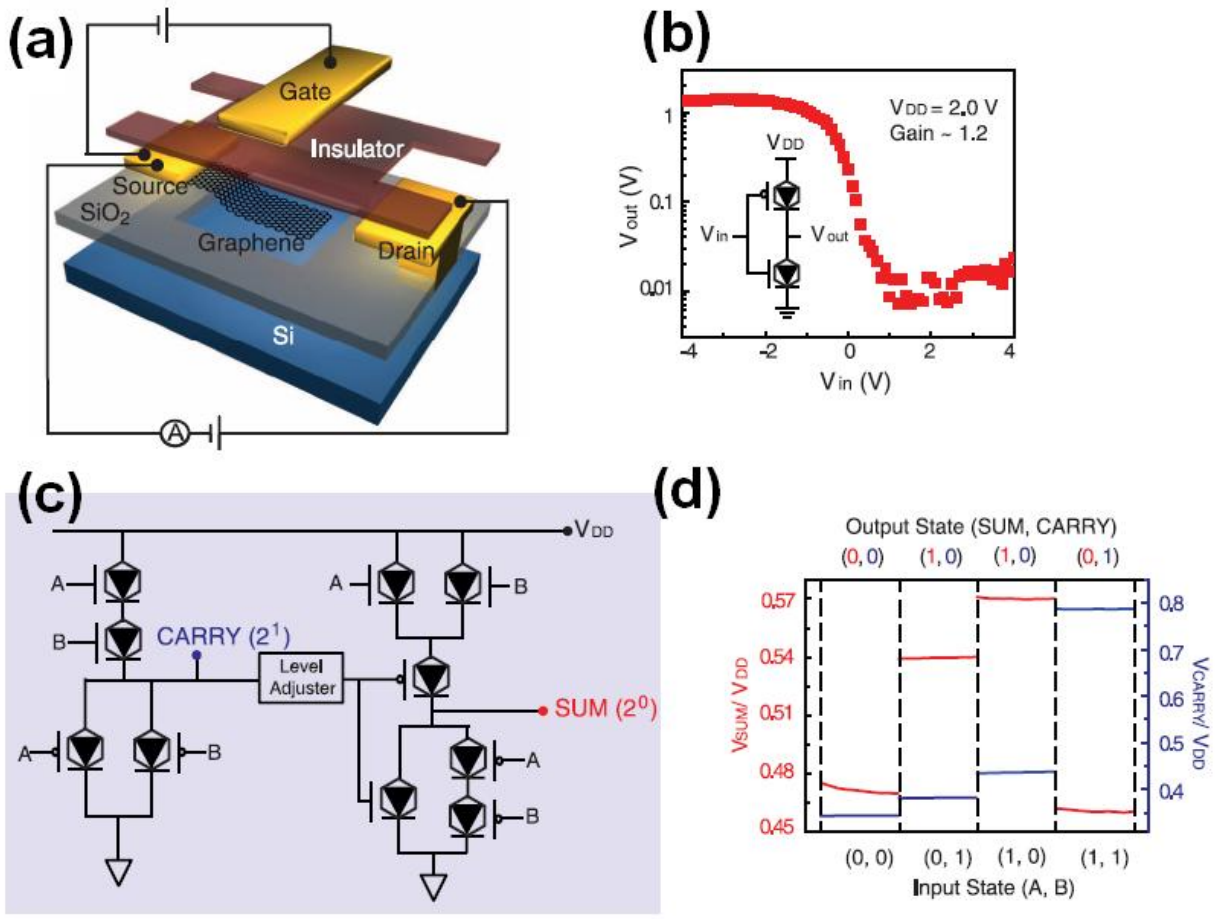

Figure 1.2.2.4 (a) A schematic diagram to show the concept of a graphene barristor. (b) Inverter characteristics obtained from integrated n- and p-type graphene barristors and schematic circuit diagram for the inverter. Positive supply voltage (V_{DD}) is connected to p-type graphene barristor, and the gain of the inverter is ~1.2. (c) Schematic of circuit design of a half-adder implemented with n- and p-type graphene barristors. (d) Output voltage levels for SUM and CARRY for four typical input states. [45]

1.2.3 Optical Properties

An unexpectedly high opacity of an atomic monolayer is originated from peculiar optical properties of graphene. This atomically thin carbon monolayer absorbs $\pi\alpha \approx 2.3\%$ of incident light over a broad wavelength range, where α is the fine-structure constant.[46, 47]

By employing graphene's impressive optical and electrical properties, an ultrafast photodetector is demonstrated experimentally up to 40 GHz without degrading for optical intensity modulations.[48] Exceptionally efficient broadband modulation of terahertz waves at room temperature is also engineered employing graphene with a low intrinsic signal attenuation.[49]

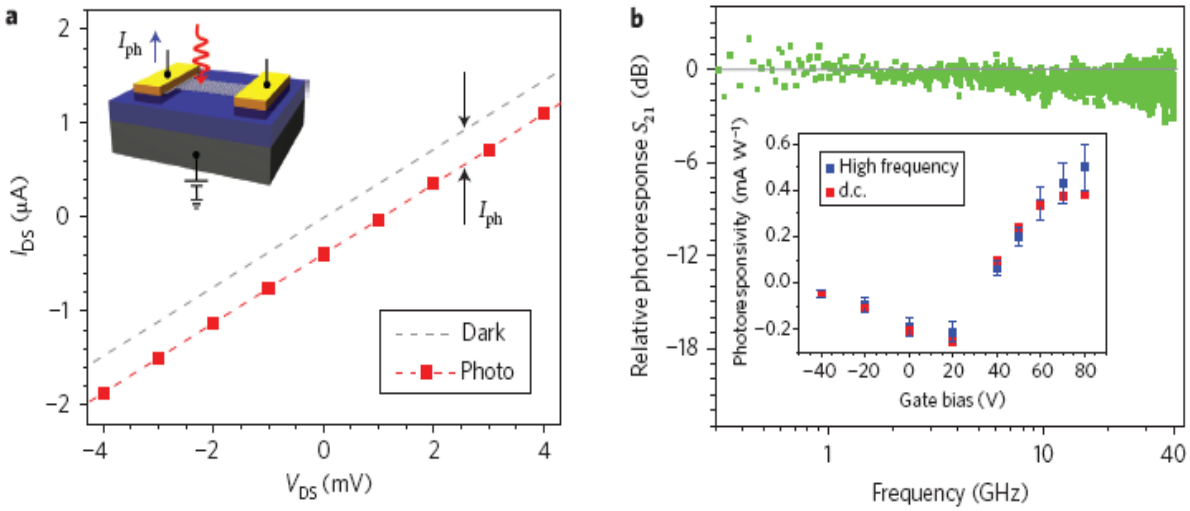

Figure 1.2.3.1 (a) Typical *I*–*V* curves of the graphene photodetector without and with light excitation. Inset: schematic of the photocurrent measurement. The curved arrow in the inset represents the incident photon. (b) Relative a.c. photoresponse $S_{21}(f)$ as a function of light intensity modulation frequency up to 40 GHz at a gate bias of 80 V. Inset: peak d.c. and high-frequency (a.c.) photoresponsivity as a function of gate bias. [48]

Even though graphene holds big potential for many optoelectronics, the most promising application is to replace ITO. In order to engineer graphene as transparent conductors for the conventional electronics, two conditions, uniform large scale synthesis and low enough sheet resistance, should be satisfied. Fortunately, CVD based roll to roll synthesis with chemical doping of graphene meets all the requirements. A doped four graphene layer film with layer-by-layer stacking shows a sheet resistance as low as ~ 30 Ω/□ at ~ 90 %

transmittance.[31] Additionally, one of the best parts of the optical properties of graphene is that the transmittance of graphene is independent of the frequency at the visible range as can be seen in Fig 1.2.3.2.[28] Since ITO is not perfectly transparent but slightly yellowish, graphene, which is transparent in the visible spectrum, can be utilized to manufacture more premium display panels.

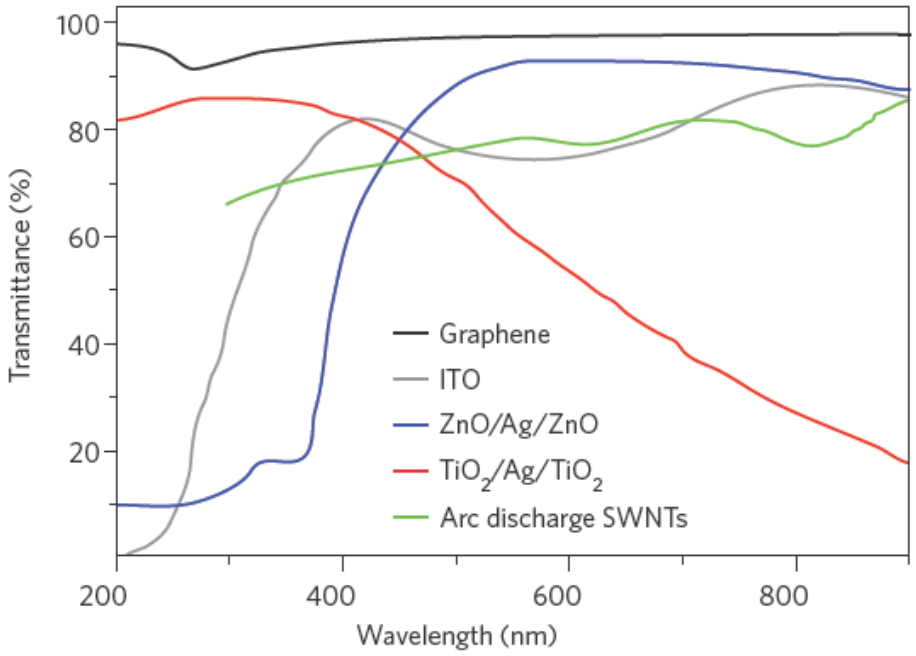

Figure 1.2.3.2 Transmittance for different transparent conductors. [28]

1.2.4 Mechanical Properties

Elastic properties and intrinsic breaking strength of free standing graphene are measured by nanoidentation and it appears to be one of the strongest materials ever tested. Breaking strength of graphene is 200 times stronger than steel, with a tensile modulus of 1 TPa.[23] Graphene is not only strong but also light, weighing only about 0.77 milligrams per square meter. These two mechanical properties of graphene make very attractive metal contacts for flexible display. By taking advantages of graphene mechanical properties, the thinnest

electromechanical resonator with a charge sensitivity down to 8×10^{-4} electrons per root hertz is realized as seen in Fig 1.2.4.1.[50]

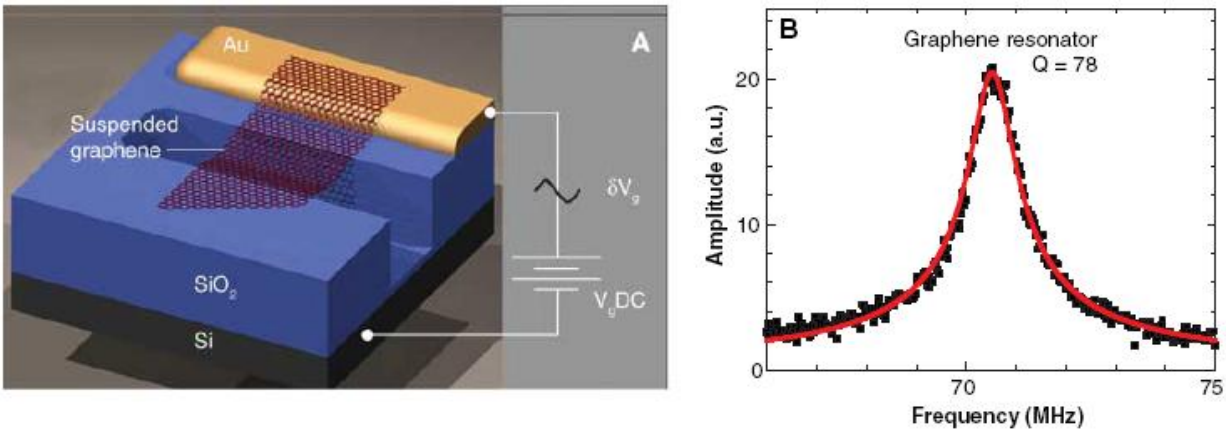

Figure 1.2.4.1 (a) Schematic of a suspended graphene resonator. (b) Amplitude versus frequency taken with optical drive for the fundamental mode of the single-layer graphene resonator. [50]

Graphene is also known as super thermal conductor. The measured thermal conductivity of graphene is 5.3×10^{3} $Wm^{-1}K^{-1}$ which is a many times higher than aluminum.[22] The outstanding thermal property of graphene can be a good solution for many high power electrical and optical devices suffering from self-heating problems. It has been reported that self-heating of high power gallium nitride devices is substantially improved by quilting graphene for heat-escaping channel.[51] It has been demonstrated that temperature of the hotspots is lowered by ~20 ºC, which corresponds to an order of magnitude improvement for the device life time as shown in Fig. 1.2.4.2.

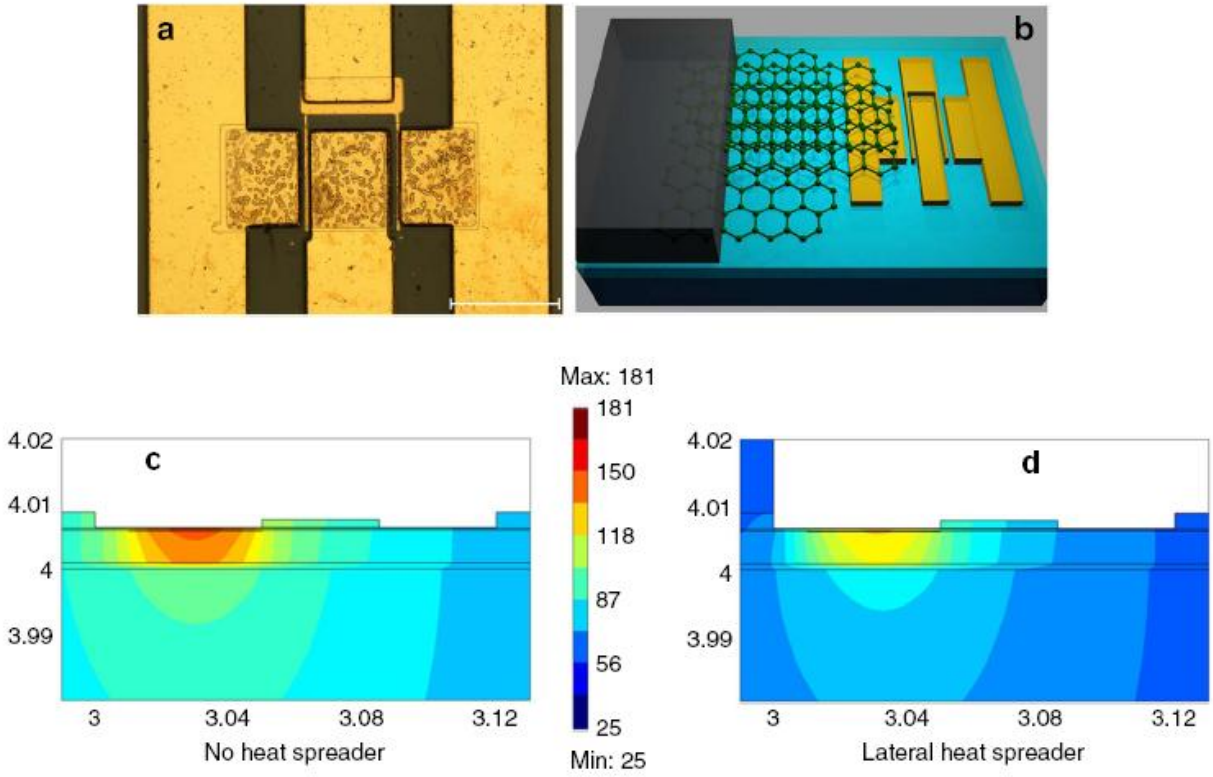

Figure 1.2.4.2 (a) Optical microscopy of AlGaN/GaN high electron mobility field effect transistors (HFETs) before fabrication of the heat spreaders. (b) Schematic of the few layer graphene–graphite heat spreaders attached to the drain contact of the AlGaN/GaN HFET. (c) Temperature distribution in AlGaN/GaN HFET without the heat spreader showing maximum T = 144 °C at the dissipated power P = 12.8 W mm^{-1}. (d) Temperature distribution in the AlGaN/GaN HFET with the graphite heat spreader, which has sizes matching one of the experimental structures. The maximum temperature is T = 127 °C at the same power P = 12.8 W mm^{-1}. [51]

Another interesting mechanical characteristic of graphene is its friction coefficient. The micro-scale scratch tests results show that the monolayer, bilayer, and trilayer graphene all yield friction coefficients of approximately 0.03 as shown in Fig. 1.2.4.3.[24] It is also studied from the scratch tests that graphene itself is not delaminated or peeled off from the substrate prior to the failure point from a critical load (The critical road is referred to normal

load required for the probe to penetrate through the graphene inducing failure of the film.). Rather graphene is bent and displaced more than 50 nm together with the supporting substrate, when it reaches the failure point seen from Fig. 1.2.4.4. One atom-thick-layer material holds the normal displacement for more than 100 times of its thickness. Graphene can be employed for antiwear coatings with its very low friction coefficient and elastic characteristic. In particular, graphene can be an ideal material as lubricant layer for the next generation magnetic media of hard disks, since future tribology technology of hard disks requires sub-2 nm of the disk overcoat.

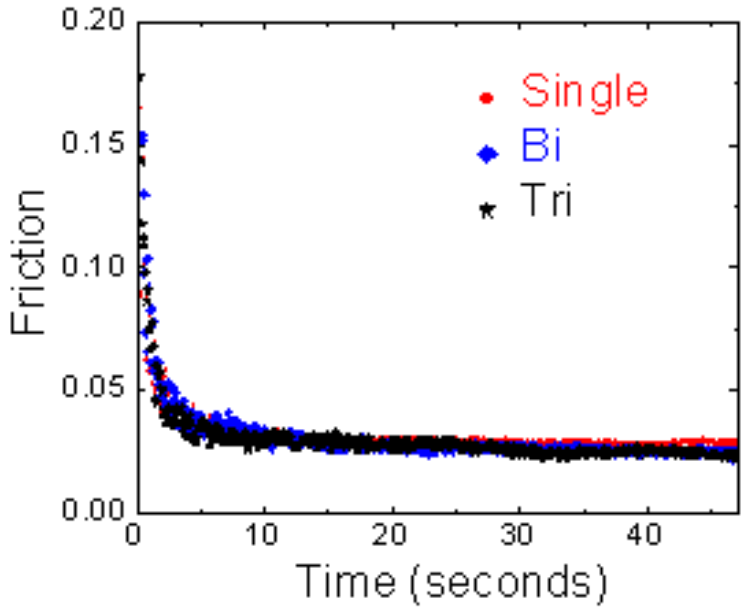

Figure 1.2.4.3 Friction coefficient (lateral force/normal force) versus time of single, bi-, and tri-layer graphene. [24]

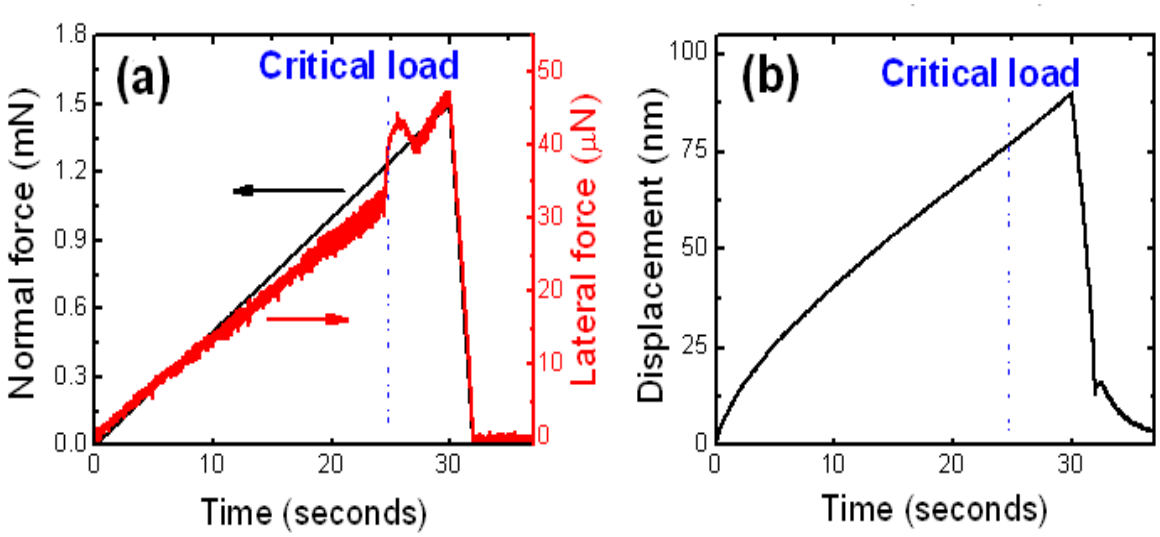

Figure 1.2.4.4 (a) Normal force and lateral force versus time on graphene. (b) Normal displacement of probe versus time of the sample in (a). [24]

1.2.5 Large Scale Graphene

In order to obtain chemically exfoliated graphene, graphene oxide should be achieved as precursors by annealing graphite rapidly.[54] By annealing graphene oxide flakes in argon or hydrogen environments, chemically exfoliated graphene (or reduced graphene oxide) power can be achieved. However, the electrical qualities of chemically exfoliated graphene are not good enough to be utilized in electronics due to the incomplete removal of various functional groups such as oxides and hydroxyls. These powers can be mixed with metals in order to improve a breaking strength and to make metals light.

Figure 1.2.5.1 Photographs of GO thin films on filtration membrane (a), glass (b) and plastic (c) substrates. [54]

Growing graphitic layers on top of nickel by CVD of hydrocarbons has been known for a long times. Large-scale graphene has been synthesized in the same way. After understanding that rapid cool-down after the reaction between methane and nickel at 1000 ºC is a key technique to suppress forming thick graphitic layers, a few layer graphene have been successfully produced. The synthesized graphene layer on top of nickel can be transferred to any type of substrates by using polydimethysiloxane (PDMS) stamps. Using nickel was initially used, but it is not good enough to synthesize uniform and single layer graphene.[55] By using copper as a catalyst, centimeter-scale single layer graphene is formed predominantly with less than 5% of multilayer graphene.[56] A 30 inch single layer graphene sheet using copper catalyst is produced by employing a roll to roll method. The synthesized single layer graphene by the roll to roll method shows a sheet resistance as low as 125 Ω/□ and 97.4% optical transmittance. [31] When p-doped graphene is stacked one by one as four layers with the roll to roll method, the sheet resistance of graphene can be as low as ~30 Ω/□ with ~90% optical transmittance, which is superior to conventional transparent electrodes such as ITO as seen from Fig. 1.2.5.3.

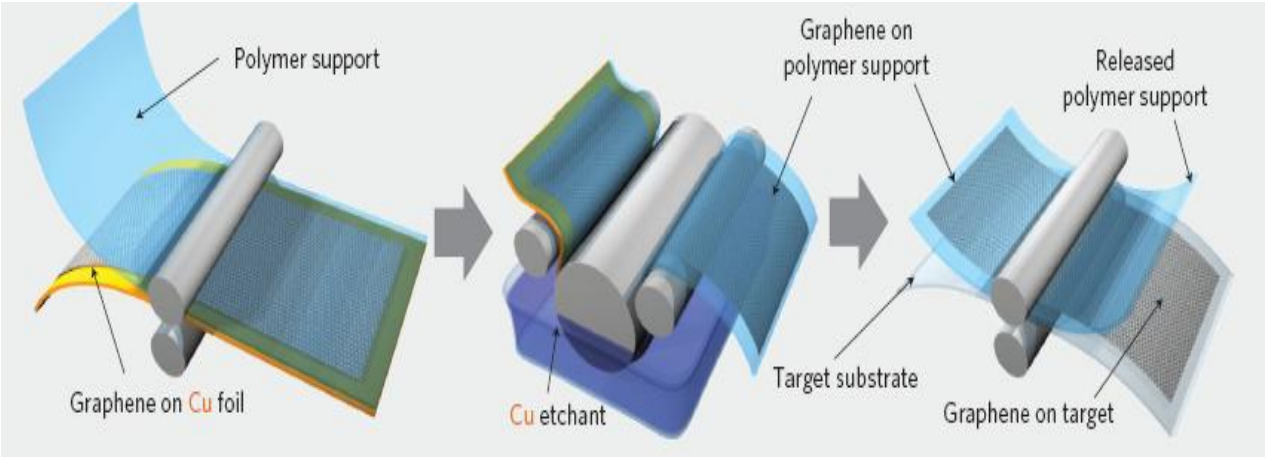

Figure 1.2.5.2 Schematic of the roll-based production of graphene films grown on a copper foil. [31]

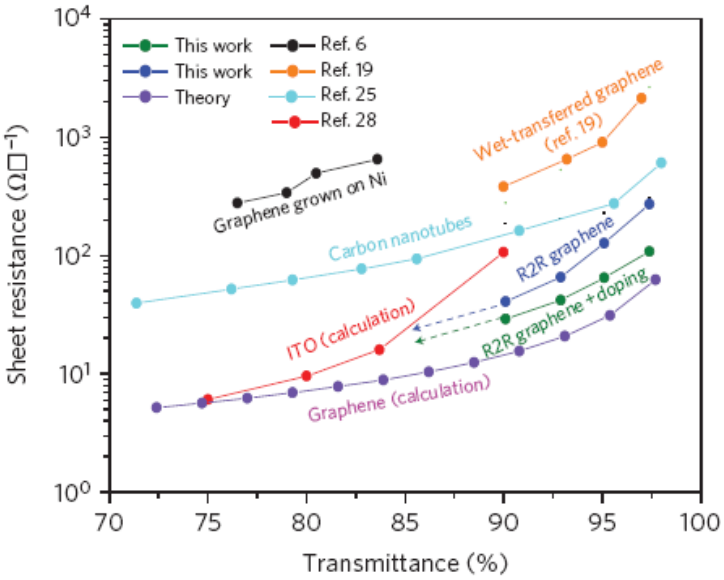

Figure 1.2.5.3 Comparison of sheet resistance. The dashed arrows indicate the expected sheet resistances at lower transmittance. [31]

Near room-temperature and transfer-free method is also introduced.[57] Carbons from graphite poweder source diffuse through the Ni film and crystallize as graphene at the interface as can be seen from Fig. 1.2.5.4. There is no limitations on the choice of substrates, since it does not require high termperature process. By employing this process, graphene can

be even grown on top of plastic directly. However, the mobility of graphene is ~ 667$cm^2V^{-1}s^{-1}$, which is very low compared to that of the one from conventional CVD growths.

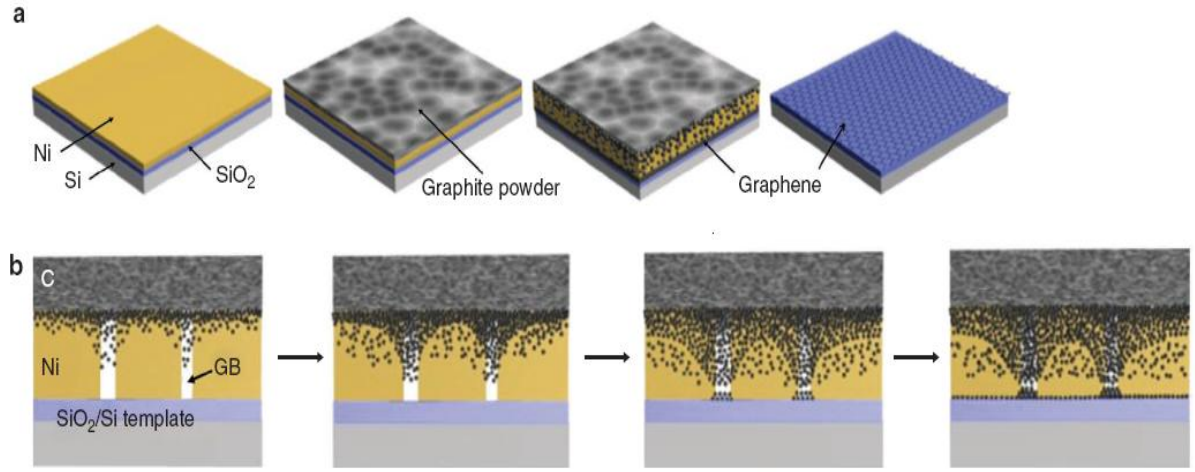

Figure 1.2.5.4 (a)Schematic drawing of the diffusion-assisted synthesis process for directly depositing graphene films on nonconducting substrates.(b) T ≤ 260 °C; preferential diffusion of Carbon atoms via graphene boundarys in Ni, followed by heterogeneous nucleation at the defect sites and growth via lateral diffusion of C atoms along Ni/substrate interface. [57]

1.1 Motivations and Objectives

Graphene-based transistors have been developed rapidly for the last few years, since graphene was born from the "Scotch tape" method. Graphene has attracted enormous attention from engineers, as it has been considered as a good candidate for next generation materials. However, many questions still remain about the potential performance of graphene-based transistors in real electronic applications. Generally, the mobility of graphene can be considered at least ten times higher than that of silicon at room temperature. In spite of graphene's high mobility, graphene has a bottleneck due to it's a very low on-off ratio.[19] The on-off ratio, I_{on}/I_{off}, of graphene is not high enough for graphene to be engineered as logic or memory devices because of its zero band gap characteristic. To overcome the

limitation, band gap engineering is proposed to improve the on-off ratio of graphene. However, the mobility of graphene is not advantageous anymore compared to that of silicon, when the band gap of the graphene nanoribbon is close to the band gap of silicon, because the mobility is inversely proportional to the band gap.[44] The carbon nanotubes, the cousin of graphene and a rising star 20 years ago, were believed to create a new paradigm in the electronics world, but ended in failure of engineering due to the difficulty of mass fabrication with precise alignments.[52] Will graphene follow the history of the carbon nanotubes? In my humble opinion, graphene is taking a different path from its cousin, carbon nanotube as can be seen from Fig. 1.3.1.[44]

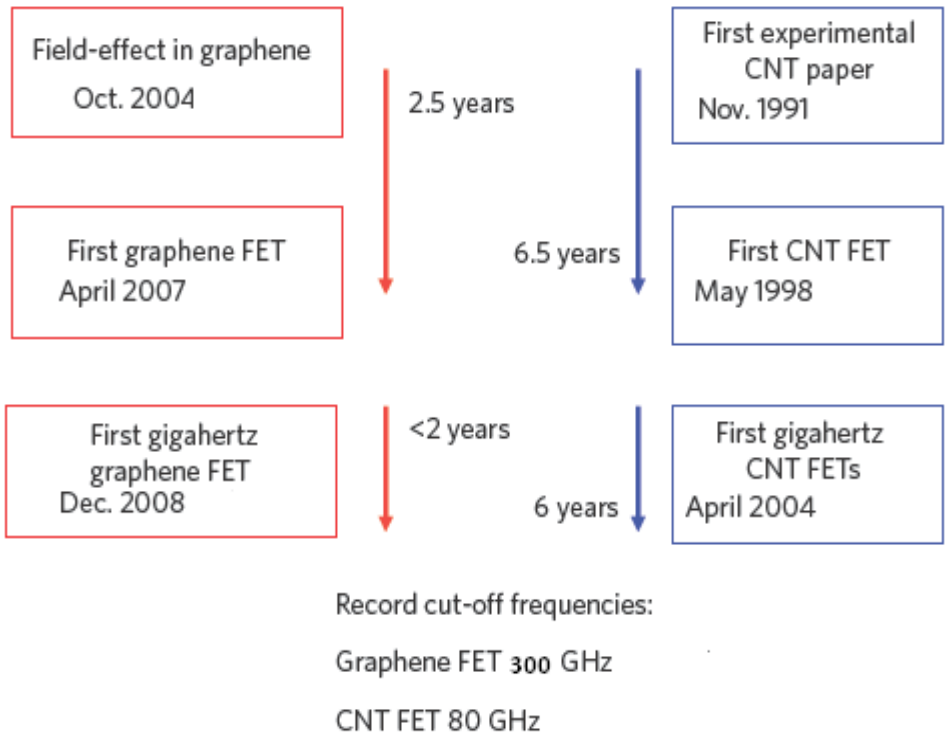

Figure 1.3.1 Progress in graphene MOSFET development compared with the evolution of nanotube FETs. [44]

Moreover, the CVD based growth method enables graphene to become large scale and to be transferred to any type of substrates as mentioned previously. Graphene synthesized by CVD methods is well suited with conventional semiconductor processing. There are many materials which have very outstanding electrical properties compared to silicon, however none of these materials seems to be possible to compete with silicon in terms of mass production and cost.[31] Practically, it might be also very difficult for graphene to be utilized as logic and memory devices. However, the beauty of graphene is not only its mobility but also its transparency. Graphene's high electrical conductivity and high optical transparency make it a candidate for transparent conducting electrodes, which are required for such applications as touch screen, liquid crystal displays, organic photovoltaic cells, and organic light-emitting diodes (OLEDs), as seen from Fig. 1.3.2. [9] In particular, graphene's mechanical strength and flexibility are advantageous compared to ITO, which is too brittle to be applied for the next generation flexible displays. As the promising potential is reflected, major electronic companies such as IBM and Samsung have been investing graphene for applications. Especially, Samsung Techwin has started building up pilot lines for CVD-based large-scale graphene. A few experimental results have been already reported that graphene grown by the CVD method can be incorporated well with conventional organic photovoltaic devices and light-emitting diodes as shown in Fig 1.3.2. Since graphene has been dominantly studied in the physics point of view, many experimental transports have focused on low bias and low temperature measurements. In order to test its potential for real applications, the electrical transport of graphene with high enough operational voltage biases should be understood and examined thoroughly. The stability of electrical transport is another important issue to be understood for applications in addition to the interface issues such as charge traps.

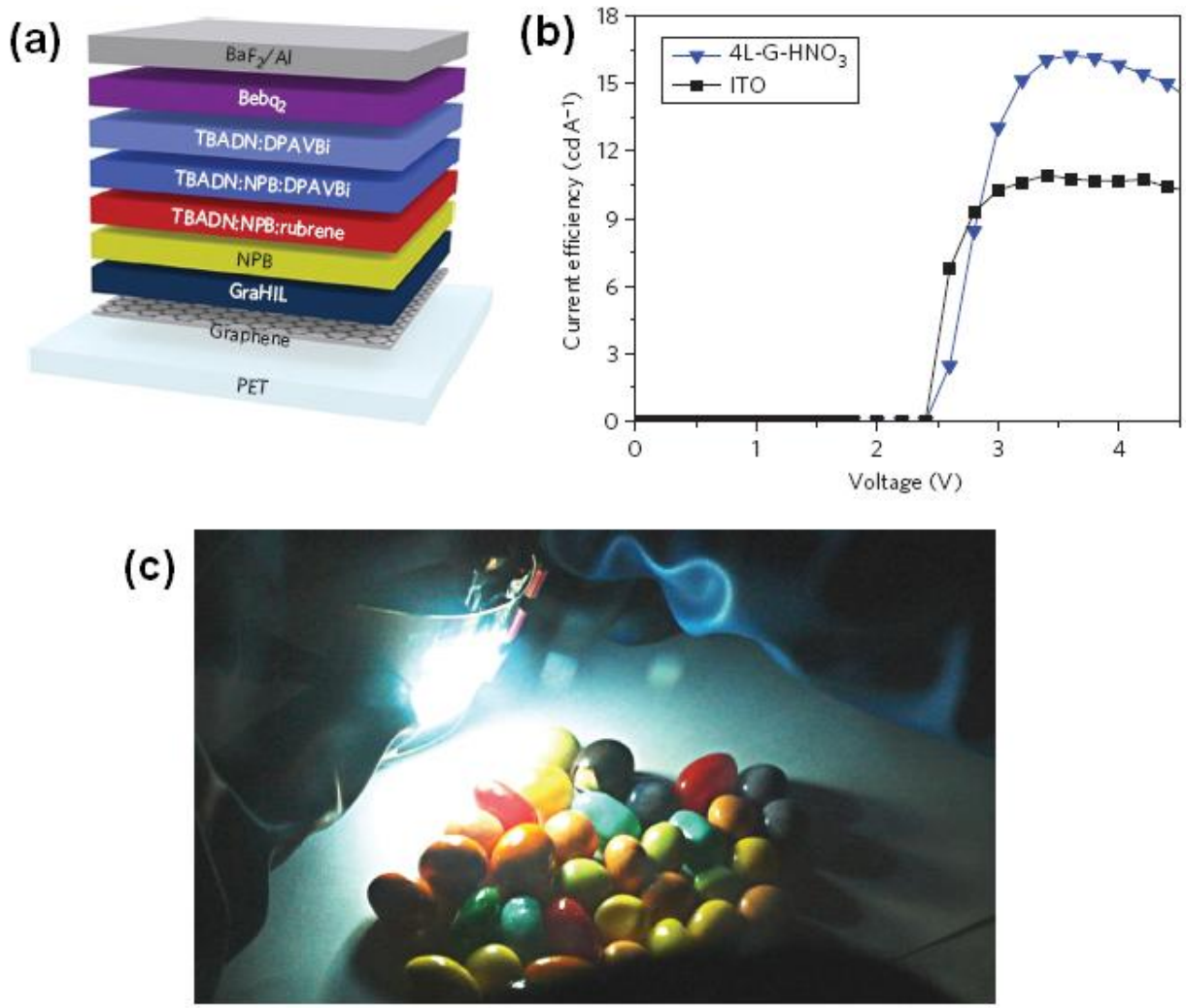

Figure 1.3.2 (a) Device structure. (b) as a function of voltage for flexible white OLED devices with graphene (doped with HNO_3) and ITO anodes.(c) Flexible OLED lighting device with a graphene anode on a 5 cm× 5 cm PET substrate. [9]

The focus of this dissertation is an understanding of the fabrication and electrical transport of graphene devices. In chapter 2, various methods of graphene preparations are introduced as well as an overview on experimental techniques used for this work. In chapter 3, the surface property of graphene is studied in order to have better electrical contacts. The optimization of fabrication procedures is very important for mass production, in which billions of contact for each device should be fabricated without any failure. In chapter 4, current hysteresis in graphene devices is investigated with a two-terminal configuration. By

changing the back gate bias, ambipolar bistable switching is observed. We propose charging and discharging effect for the origin of the ambipolar hysteresis. In order to support our theory, quantum transport simulations are performed and the results indicate charging and discharging effect plays an important role in hysteretic switching. In chapter 5, the origin of hysteresis in the channel resistance from top gated graphene transistors is studied. Capacitance - voltage measurements across the gate oxide on top gated bilayer graphene show hysteresis. However, the measured capacitance across the graphene channel does not show any hysteresis, but shows an abrupt jump at a high channel voltage due to the emergence of an order, indicating that the origin of hysteresis between gate and source is due to charge traps present in the gate oxide and graphene interface. In chapter 6, the tunneling behavior in graphene at a high voltage bias is reported. When high voltage is applied across the graphene channel, a negative differential conductance is found just before the breakdown as a symptom of the tunneling behavior. After the breakdown, non-linear *I-V* curves are measured. Raman spectroscopy is employed to investigate the origin of tunneling characteristic and crystalline graphene is transformed to non-uniform disordered graphene under the application of high voltage bias. In chapter 7, a stochastic nonlinear electrical characteristic of graphene is investigated. Abrupt current changes are observed from voltage sweeps between the source and drain with an ON/OFF ratio up to 10^3. It is found that graphene channel experience the topological change. Active radicals in an uneven graphene channel cause local changes of electrostatic potential. Simulation results based on the self-trapped electron and hole mechanism account well for the experimental data. Our findings illustrate an important issue of reliable electron transports and help for the understanding of transport properties in graphene devices. In chapter 8, the thesis is concluded by summarizing the accomplishments of this project and proposing future works.

2. General Experimental Techniques

2.1 Preparation of Graphene

2.1.1 Mechanical Exfoliation

Graphene with a single layer and multiple layers can be obtained by exfoliating highly oriented pyrolitic graphite (HOPG). Scotch tape is employed to peel off the graphite chunk from the HOPG repeatedly.[3] The flakes on the tape can be transferred to SiO_2 substrates and atomically thin graphene can be found by optical microscope using the contrast difference between graphene and 300 nm SiO_2.[53] The size of mechanically exfoliated graphene is limited to micrometer scale. Therefore, this method is not applicable for industrial production, but still very useful for the study of fundamental physics and for the fabrication of prototype devices. The mechanically cleaved graphene sample is used most widely in laboratories.

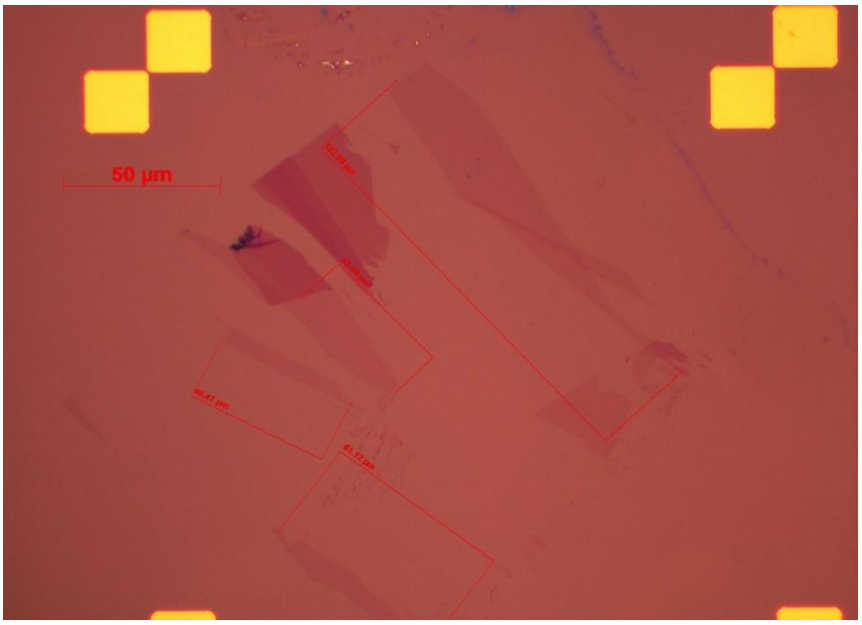

Figure 2.1.1.1 Mechanically exfoliated graphene flakes on top of 300 nm SiO_2

2.1.2 Thermal Decomposition of SiC

By heating silicon carbide to high temperature above 1100 ºC in an ultra high vacuum, wafer-scale epitaxial graphene can be obtained. Si is sublimated from SiC leaving behind a carbon rich surface.[8] The thickness and electrical properties such as the mobility and carrier density are highly dependent on the face of SiC, silicon-terminated or carbon-terminated. Many important physical properties have been measured from epitaxial graphene made of silicon carbide in the beginning. For an example, the electronic band structure was visualized by angle-resolved photoemission spectroscopy. In 2009, IBM successfully engineered very fast graphene transistors with a cutoff frequency of 100 GHz.

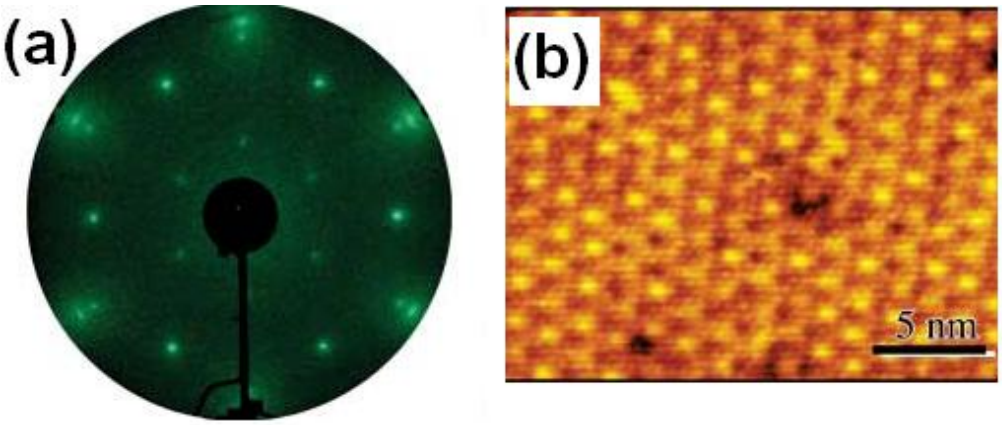

Figure 2.1.2.1 (a) Low Electron Energy Diffraction (LEED) pattern (71 eV) of three monolayer of epitaxial graphene on 4H-SiC(C-terminated face). (b) STM image of one monolayer of epitaxial graphene on SiC(0001). [8]

2.2 Raman Spectroscopy

Raman spectroscopy is a spectroscopic technique which is used to investigate vibrational, rotational, and low frequency modes from various materials. The inelastic scattering of

electromagnetic radiation due to energy transfer between the incident photons and the molecules during their interaction is the mechanism of Raman spectroscopy. When the electromagnetic radiation interacts with the molecule, an electron is excited from the ground state to a virtual energy state; it subsequently relaxes to an energy state different from the initial energy state. Energy exchange does not occur, if the energy of the resulting photon released during the relaxation from the virtual energy level is the same as the energy of the incident photon. This scattering is known as Rayleigh scattering. Inelastic Stokes and anti-Stokes scattering can be observed, if the energy of the resulting photon released from relaxation is less or more than the energy of the incident photon due to relaxation to a different vibrational or rotational state as can be seen from Fig. 2.2.1.[58] It has been intensively used, being a routine, non-destructive way to characterize the structural quality of diamond, diamond-like carbon (DLC) and CNTs. [59]

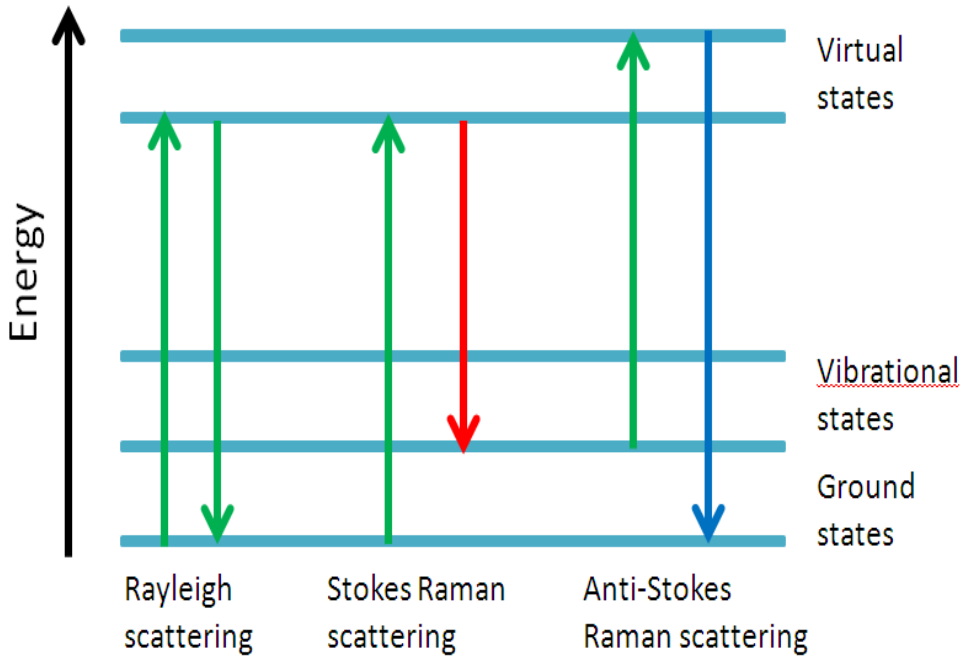

Figure 2.2.1 Rayleigh, Stokes and anti-Stokes scattering.

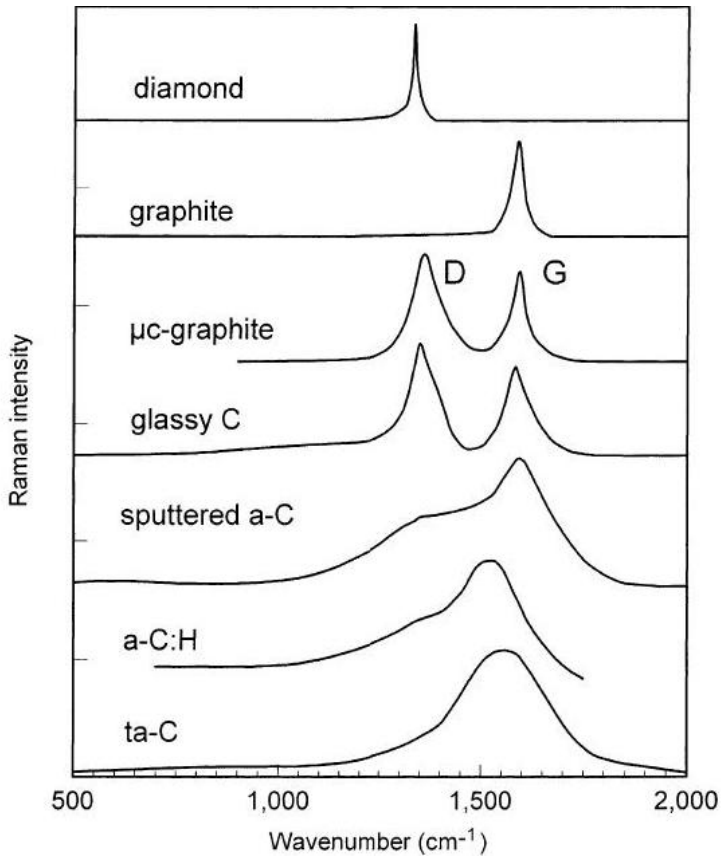

Figure 2.2.2 Comparison of typical Raman spectra of carbons. [59]

Raman spectroscopy is one of the most efficient methods to confirm the number of layer and nature of defects in graphene. There are three distinctive peaks, when graphene is characterized by Raman spectroscopy. The first peak is the G-band at ~1584 cm^{-1} which is originated from in-plane vibration of the sp^2 bonded carbon atoms. The second peak is the 2D-band at ~2700 cm^{-1} which is related to a second-order two-phonon mode. The last peak is the D-band at ~1350 cm^{-1} which is due to the defect level of graphene.[60] The D-band cannot be observed from pristine graphene. The structural and electronic properties of graphene can be reflected from the variation in shape, position and relative intensity of G-, 2D- and D-bands. The number of graphene layer can be distinguished by comparing the full width half maximum (FWHM) value of 2D-band.[61]

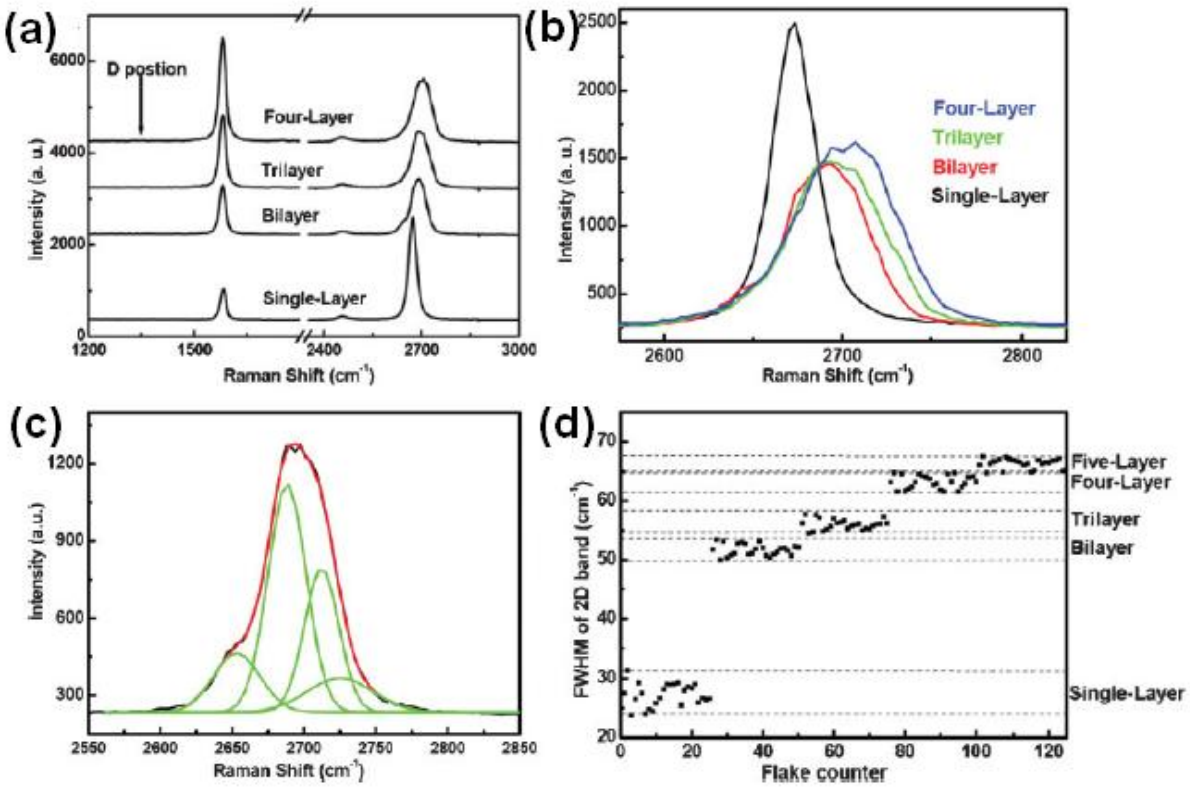

Figure 2.2.3 (a) Raman spectra of graphene with different number of layers. (b) Magnified 2D band. (c) The fitted four components of 2D band in bilayer graphene. (d) The statistical data of FWHM with respect to different number layer. [61]

2.3 Defect free Deposition onto Graphene

It is important to keep graphene as pristine as possible during depositions onto graphene in order to maintain its high mobility and to observe peculiar physical phenomenon as well. Low energy deposition process is preferred to protect graphene from defects as can be seen from Fig 2.3.1.[62] Various methods to deposit thin films onto graphene are tried and the level of damage of graphene is investigated by Raman spectroscopy. 3 nm SiO_2, 2 nm TiO_2, 2 nm Cr, 2 nm Cr and 2 nm Cu has been deposited onto graphene by plasma enhanced chemical vapor deposition (PECVD), pulsed laser deposition (PLD), thermal evaporation, e-beam evaporation, and sputtering with their typical deposition parameters, respectively. As plotted in Fig. 2.3.2, only thermal evaporation gives rise to a negligible D peak after the

deposition. A significant D peak appears with the other methods, such as PLD, e-beam evaporation, PECVD, and sputtering. Among these methods, PLD and sputtering induce most significant disorder. From the shape and position of these three peaks (D, G and 2D) and the ratio I_D/I_G, Ferrari and Robertson introduced a three stage model of disorder in carbon materials, which allows to simply assess the Raman spectra of graphene: the early stage leads to nanocrystalline graphite (nc-G phase) from crystalline graphite, the second stage is low tetragonal amorphous carbon (a-C phase), and the third stage is high sp^3 tetrahedral amorphous carbon (ta-C phase).[63] In the following, these three stages are referred in order to quantify the impact of deposition on the structural quality of graphene sheets. According to this model, for e-beam evaporation and PECVD, the disorder level is moderate and the amorphization is at the first stage. A second stage amorphization has been occurred to graphene with the PLD and sputtering processes. According to Raman Spectroscopy, thermal evaporation is the most recommended method to deposit metal contacts onto graphene. E-beam evaporator can be also employed, when it has long enough distance between graphene and crucible.

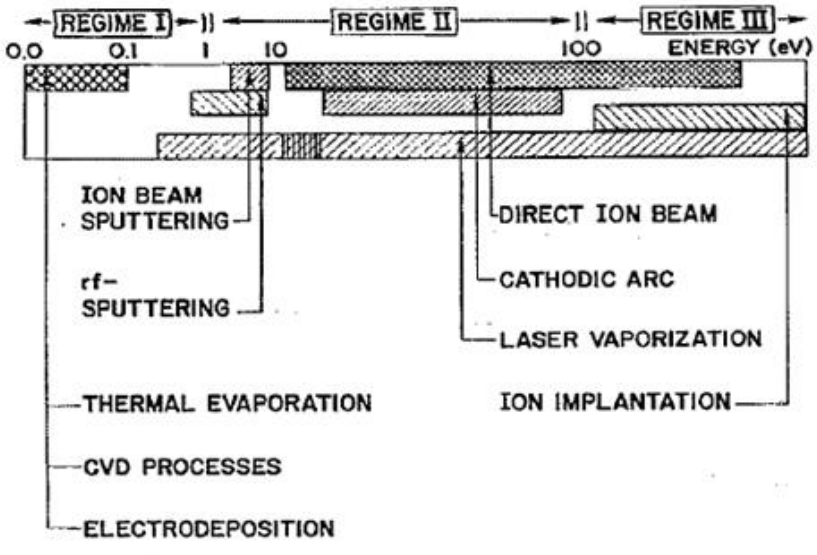

Figure 2.3.1 Energy of depositing species produced by a variety of deposition process. [62]

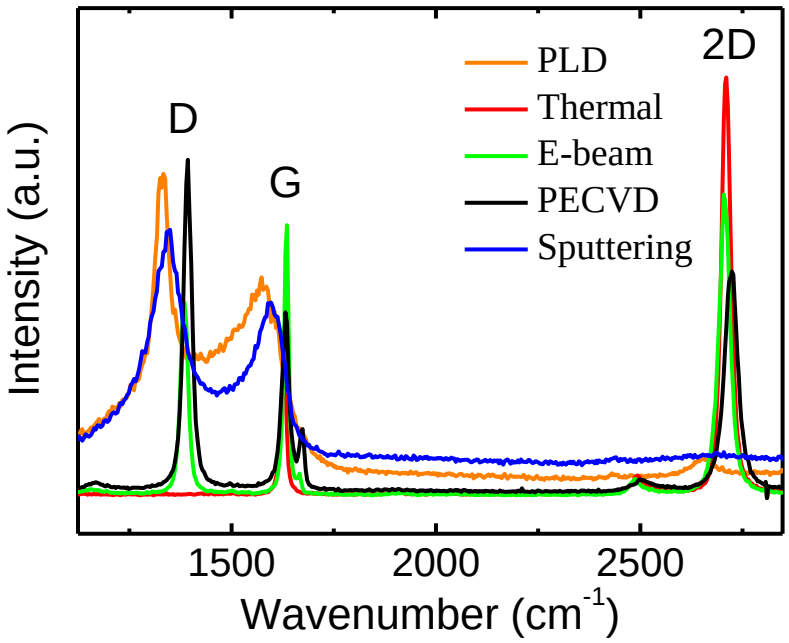

Figure 2.3.2 Raman spectra of graphene with the various deposition methods.

Sputtering is a versatile technique to deposit various metals and insulators for example, indium tin oxide to make transparent devices. However, the sputtering process causes damage to graphene because of high energy sputtered atoms. We develop a new sputtering technique preventing damage onto graphene during the deposition. Various materials are sputtered onto graphene using sputtering in two configurations; one is the normal the other is the flipping configuration. The schematic of two configurations is shown in Fig. 2.3.3. In the normal configuration, the graphene faces the sputter targets. In the flipping case, since the samples are flipped as the backside of the graphene samples faces the targets, the energy of atom bombardment can be greatly reduced especially at a high Ar pressure, as shown in Fig. 2.3.3(b), when the materials are deposited onto the flipped sample surface. 4 nm $Co_{70}Fe_{30}$ and 2 nm Al is deposited onto graphene by dc sputtering at a power of 60 W. 3 nm MgO is deposited by rf sputtering at 120 W, and 1 nm MgO is deposited by dc reactive sputtering at 60 W in a mixture of 30 sccm Ar and 1 sccm O_2 gas. All the deposition pressures are set to 20

mTorr which is much higher than a typical value of 3 mTorr in the sputtering process. The distance from the target to substrate is fixed to 30 cm. The purpose of using a high Ar pressure of 20 mTorr is to increase the atoms collision probability. Therefore, more atoms can be condensate onto the flipped sample surface, and the energy of atoms reduces when they reach the graphene surface. The deposition rate reduces in the flipping configuration. For example, the deposition rate of CoFe, Al, and MgO (rf) is 6.3 nm, 5.6 nm, and 6.3 nm per hour, respectively, in the normal configuration, while it is 3.5 nm, 2.5 nm, and 0.5 nm per hour in the flipping configuration, respectively. The deposition rate of reactive sputtered MgO using the flipping method is 1 nm per hour.

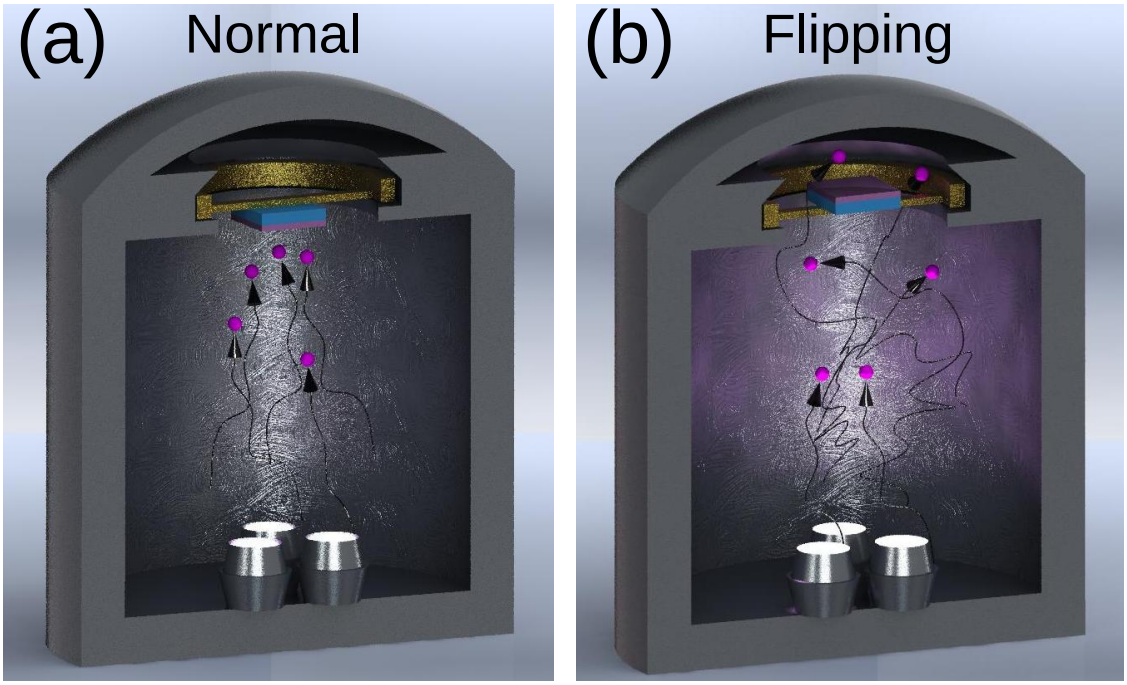

Figure 2.3.3 Schematic of sputtering deposition in the normal configuration with low Ar pressure (a) and the flipping configuration with high Ar pressure (b). The arrows show the trajectory of the sputtered atoms.

Figure 2.3.4(a) shows the Raman spectra after the deposition of 4 nm CoFe on graphene by two methods. With the normal deposition method, the appearance of the D peak indicates that the deposition of CoFe breaks the symmetry of graphene and induces disorder. However, the in-plane correlation length (L_a) is calculated to be 6.07 and the disorder level is still good for certain graphene applications due to the deposition in a high Ar pressure.[64] This shows that high Ar pressure (20 mTorr) for sputtering can greatly reduce the disorder level as compared to the result of low Ar pressure (3 mTorr) sputtering as shown in Fig. 2.3.2. The level of damage of graphene can be further reduced, once the flipping method is utilized together with high Ar pressure. The Raman spectrum using the flipping method shows a negligible D peak, while the G and 2D peaks preserve their shapes, indicating the suitability of proposed dc sputtering method onto graphene.

The Raman spectra after the deposition of 2 nm Al on graphene are shown in Fig. 2.3.4(b). The result is similar to the case of CoFe. No disorder is seen from the spectra by using the flipping method, however, slight disorder appears in the normal method. A common adopted method to form AlO_x is to deposit Al and then subsequently oxidized it in atmosphere, pure O_2, or oxygen plasma.[65] Since AlO_x is often used as a tunnel barrier for spintronic devices or a dielectric layer to apply gate bias, our work thus sheds light on future graphene applications via sputtering.

Simply reducing the sputtering power is not helpful to reduce the damage level of graphene. For example, we reduce the CoFe deposition power from 60 to 23 W for the normal sputtering configuration, so that the deposition rate is the same to the flipping configuration. The D peak appears in the Raman spectra which is comparable with the one seen at 60 W in the same configuration (not shown). The improvement in disorder using the flipping method should be mainly attributed to the reduced energy of atoms, when they reach the sample surface rather than a slow deposition rate.

We have also deposited 3 nm of MgO on graphene by rf sputtering. As seen from Fig. 2.3.4(c), in the normal configuration, the shapes of the G and 2D peaks vanish which show a clear amorphization of graphene. With the flipping method, the D and G peaks can be still observed after the deposition, while the 2D peak disappears from the spectrum. Compared to the normal deposition configuration, the flipping method thus shows an improvement, but is not suitable for a high quality graphene device. This is due to the limitation of rf sputtering. In rf sputtering a high frequency ac voltage is applied between the ground of the sample holder and the target to discharge the target surface. The plasma of rf sputtering is more extended and Ar^+ ions are also present around the sample, therefore, rf sputtering has an enhanced ion bombardment which will induce large disorder onto graphene in both configurations. This can explain larger disorder of graphene due to rf deposited MgO as compared to AlO_x obtained by dc sputtering from an Al target as reported previously.[66]

Reactive sputtering is an alternative method to deposit high quality tunnel barriers in a reactive gas mixture with Ar.[67] We have deposited 1 nm MgO onto graphene by dc reactive sputtering with the flipping method and the Raman spectra is shown in Fig. 2.3.4(d). A small D peak is observed, which comes from the oxygen plasma due to the oxygen gas mixture. By utilizing the proposed flipping method in high Ar pressure, a better quality of graphene is obtained after the oxide deposition as compared to the previous reports[66, 68, 69], which will enable to use various oxide materials in graphene devices by sputtering. Especially, highly spin filtering MgO tunnel barriers are of great importance for spintronic applications. By replacing the O_2 gas with the N_2 or other reactive gases, various nitrides and other materials can be explored with graphene using reactive sputtering.

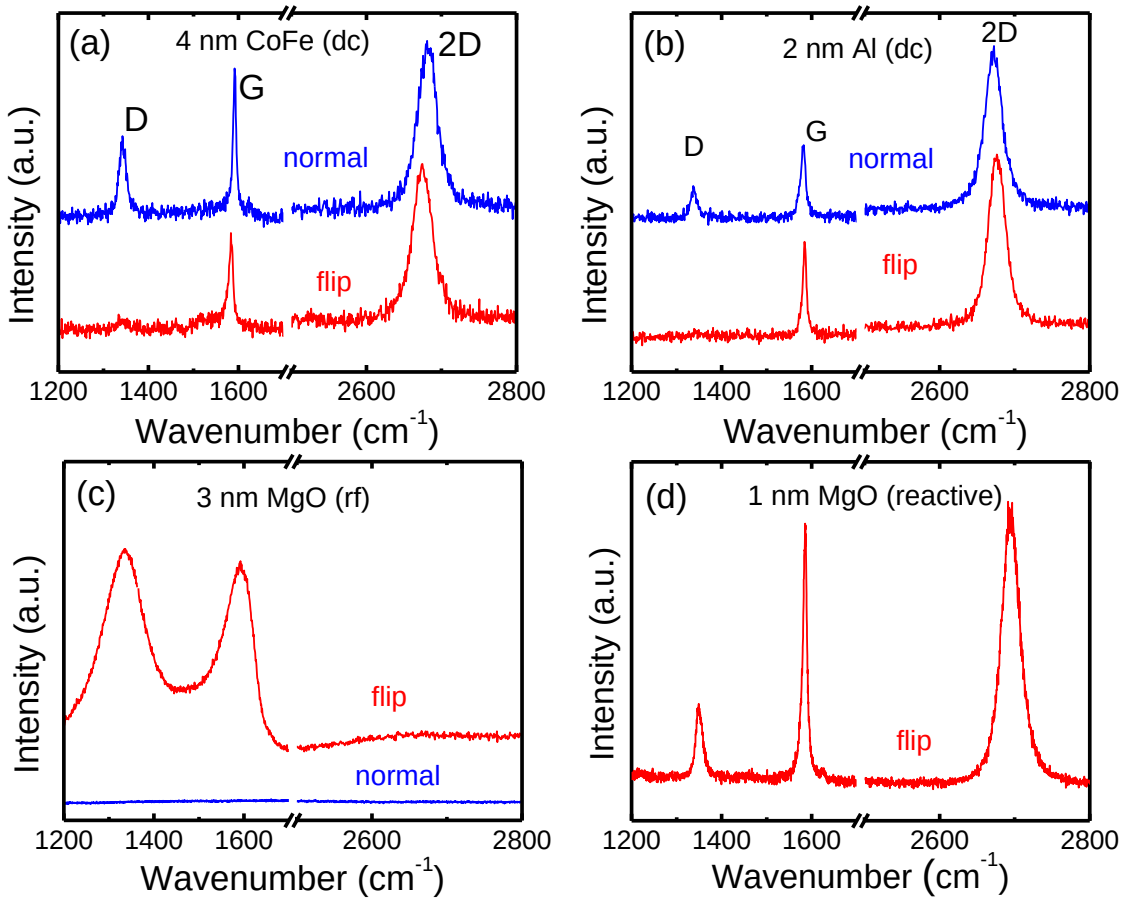

Figure 2.3.4 Raman spectra of graphene after dc sputtering of 4 nm CoFe (a) and 2 nm Al (b), rf sputtering of 3 nm MgO (c), and reactive sputtering of 1 nm MgO (d) with the normal (blue) and flipping (red) methods.

We check the uniformity of deposited materials onto graphene by the proposed sputtering method. Figure 2.3.5 shows the atomic force microscopy (AFM) images of 3 nm CoFe and 2 nm Al on graphene which were deposited by the flipping method with 20 mTorr Ar pressure. The mean roughness of CoFe on graphene is 0.432 nm, while that of Al is 0.284 nm. The films show a good uniformity promising for practical applications.

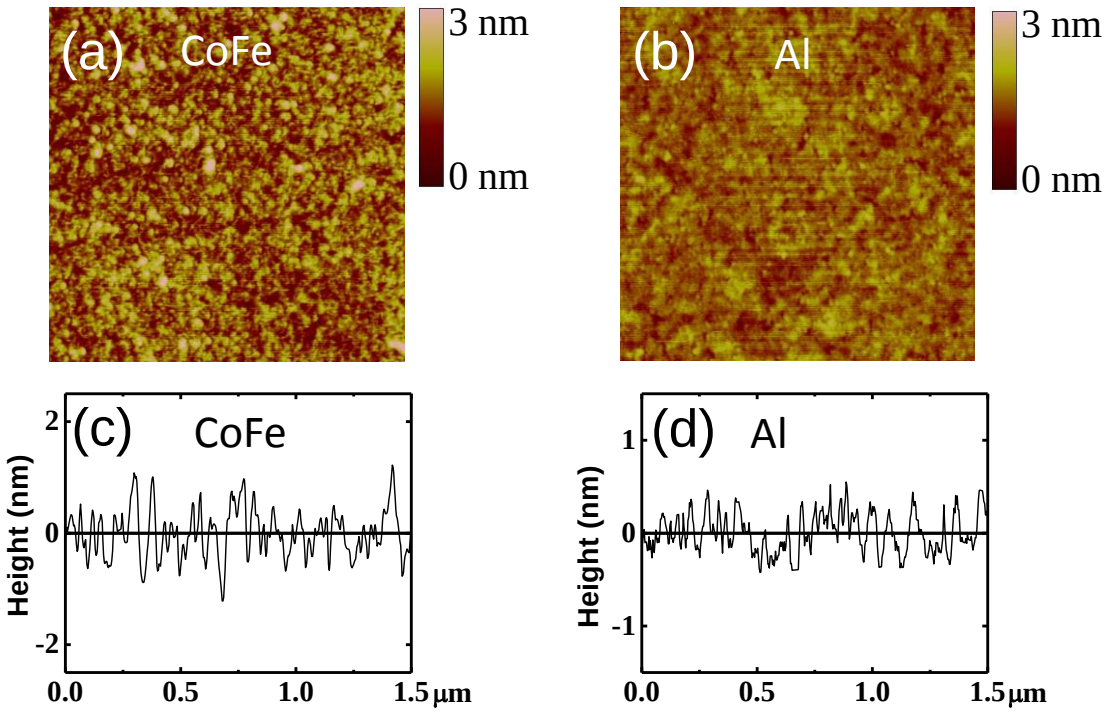

Figure 2.3.5 AFM images of CoFe (a,c) and Al (b,d) on graphene. (a) and (b) show the surface morphology over 1.5 × 1.5 μm^2. (c) and (d) show a line profile.

2.4 Device Fabrications

The mechanically cleaved graphene (MCG) was prepared by micromechanical exfoliation and transferred to Si substrates which were covered by a layer of 300nm SiO_2 with alignment markers. Both e-beam lithography and photo lithography were adapted to pattern electrodes and top gates on top of graphene. E-beam lithography was utilized for the delicate designs such as hall bar geometries. AZ5214 was chosen as photo resist for optical lithography and polymethylmethacrylate was used for e-beam lithography. After developing the electrode patterns, Cr and Au were deposited by thermal evaporator. 5nm adhesive Cr layer was deposited first for the better contacts and 100nm Au was deposited for the electrodes. Lift off process is a very crucial step after metal depositions. If sonification is used with too high power, graphene can be easily peeled off from the substrates. Overnight

immersion time in acetone is recommended to protect graphene devices from peeling off. To remove the residual from the fabrication process, the graphene devices are annealed under high vacuum conditions at 500 K for 2-24 hours .

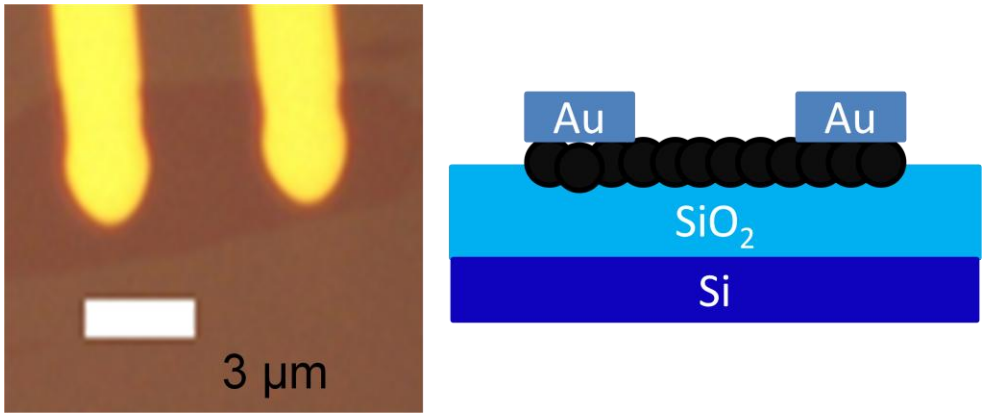

Figure 2.4.1 Optical image of two terminal graphene device and schemtatic of its side view.

3. Surface Energy Engineering of Graphene

Understanding the surface characteristics and controlling the wettability of graphene are very important for many applications. In contact deposition on top of graphene, without sufficient understanding of the surface characteristics of graphene, the process is not always guaranteed to be successful. However, there have been few studies investigating the surface property of graphene as opposed to many reports on the electrical properties, due to limited size of the single layer of epitaxial graphene (EG). In this chapter, we investigate the wettability of graphene on SiC by contact angle measurements. The dependence of the wettability on the number of graphene layers was also investigated. By treating graphene with oxygen plasma, disorder or defect was introduced on graphene and the level of disorder was determined by Raman spectroscopy. The correlation between the level of disorder and contact angle of graphene provides more insight on the physical meaning of D band in Raman spectroscopy. We also propose a method to improve the adhesion between metal contacts and the graphene surface by controlling the surface property which will introduce little or no damage to graphene.

3.1 Experimental Details

Epitaxial graphene (EG) on SiC was prepared by annealing chemically etched (10% HF solution) n-type Si-terminated 6*H*-SiC (0001) samples at 850 ^{o}C under a silicon flux for 2 minutes in an ultra-high vacuum (UHV), resulting in a Si-rich 3×3-reconstructed surface, and subsequently annealing at a higher temperature (> 1200 ^{o}C) in the absence of the silicon flux. The thickness of EG films can be controlled by the annealing temperature and time followed by slow cooling to the room temperature, allowing the preparation of samples with EG

thicknesses ranging from one to three and more layers.[70,71] The temperature of the samples was measured by an optical pyrometer. The mechanically cleaved graphene (MCG) was prepared by micromechanical exfoliation and transferred to Si substrates which was covered by a layer of 300nm SiO_2.[3] The quality of graphene was examined by scanning tunneling microscopy (STM), atomic force microscopy (AFM), and Raman spectroscopy. AFM imaging of graphene has been carried out in the contact mode and with environmental chamber which can remove moisture by controlling the environment with silica gel. The Raman spectra were obtained using 532 nm (2.33 eV) laser lines as the excitation source and laser power on the sample was below 0.5 mW to avoid laser induced heating. An objective lens with a magnification of 100X and a numerical aperture of 0.95 has been used and the focused laser spot size is ~ 500 nm in diameter. [72] The measurement of the contact angle of graphene has been carried out in ambient conditions. 0.5 μL of de-ionized water droplet has been released onto graphene surface from a syringe needle. The image of the liquid droplet was obtained in real time by using a CCD camera. A tangent line has been drawn onto the droplet from the droplet-graphene interface in the image, and the angle between the tangent line and the base line indicates the contact angle of the solid and liquid interface. The accuracy of the contact angle measurements is less than 1°. The contact angle data of twenty measurements per sample were averaged.

3.2 Graphene Characterizations by STM and Raman Spectroscopy

Figure 3.2(a-b) shows *in-situ* STM images of single and bi-layer EG on 6*H*-SiC. Honeycomb structure is clearly observed in the STM images. Detail information on the preparation and confirmation of graphene on SiC is described elsewhere.[70, 71] The AFM image in Fig. 3.2(c) clearly shows that the atomic arrangements are repeated in a regular fashion with possible distortions due to the mechanical and thermal drift. Fig. 3.2(d) shows

the Raman spectra of graphene on SiC and pristine SiC substrate. The appearance of the in-plane vibrational G band (1597 cm^{-1}) and two phonon 2D band (2715 cm^{-1}) after decomposing Si from SiC indicates that graphene has been formed on SiC.[72]

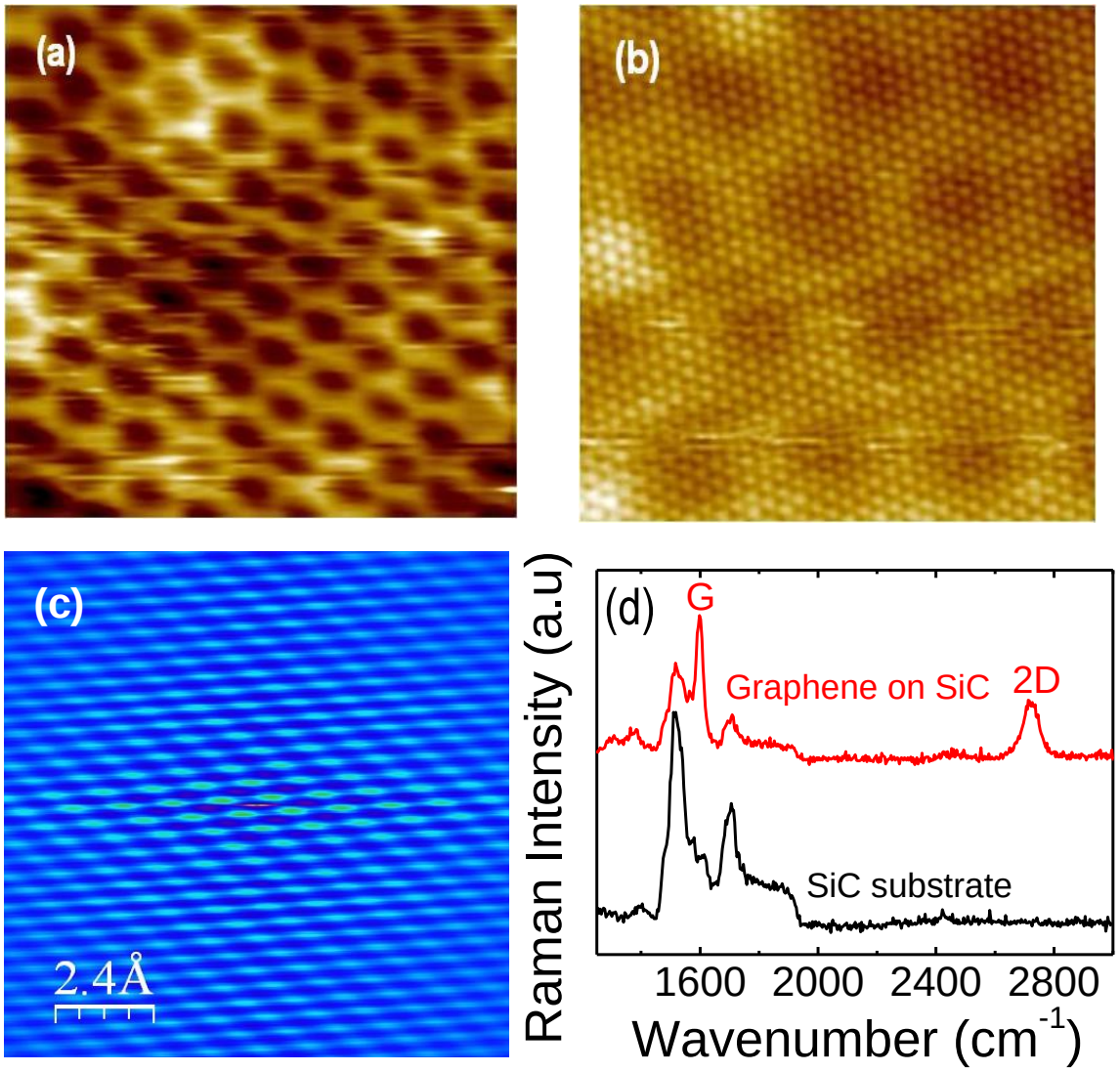

Figure 3.2 (a) 2nm × 2nm STM image of single layer graphene on 6*H*-SiC (0001). (b) 8nm × 8nm STM image of bi layer graphene on 6*H*-SiC (0001). (c) AFM image of single layer graphene on 6*H*-SiC (0001). (d) Raman spectra of single layer graphene and SiC substrate.

3.3 Contact Angle Measurement on Graphene

Figure 3.3 shows the images of water droplets on SiC substrate, highly ordered pyrolytic graphite **(**HOPG), single layer EG, and plasma etched graphene on SiC. Although only one monolayer of graphene exists on top of SiC substrate, there is a drastic change in the contact angle of the water droplet with graphene (92.5°) on SiC compared to that of pristine SiC (69.3°). The contact angle of freshly cleaved HOPG (91°) shows that it is hydrophobic similar to graphene on SiC. After completely etching monolayer of graphene by oxygen plasma at 10 W for 2 min, the contact angle (70.0°) is similar to that of a SiC substrate.

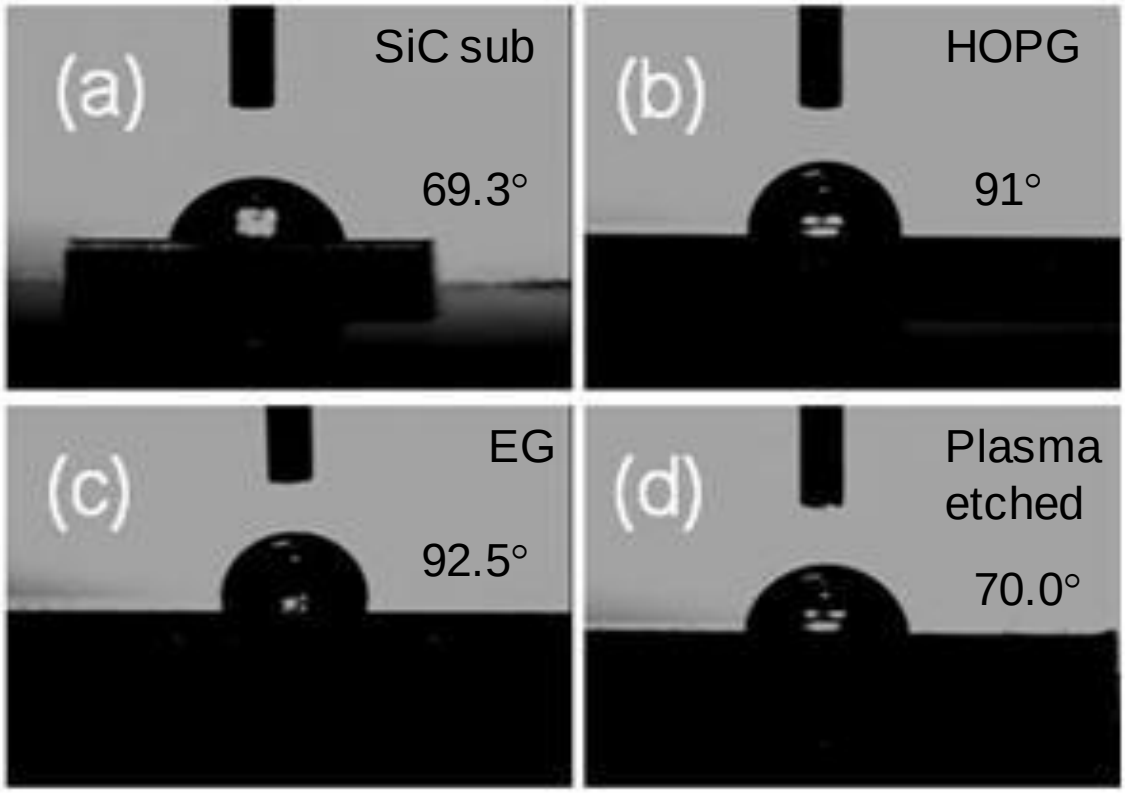

Figure 3.3 Water droplet on SiC (a), HOPG (b), single layer graphene on SiC (c), and oxygen plasma etched graphene on SiC at 10 W for 2 min (d).

Properties of graphene are sensitive to the number of layers. Different characteristics such as the electrical and mechanical properties of mono-layer, bi-layer, and tri-layer have been investigated by different groups.[7, 73, 74] In order to determine the dependence of wettability of graphene on the layer thickness, we measured the contact angle as a function of number of layers and the result is summarized in Table 3.3. By investigating the measurement result we concluded that the wettability of graphene is independent of the thickness. Wang *et al.* reported a contact angle of 120° on graphene films [75] which is quite different from our result. This difference can be attributed to their rough surface, a result of integrating many micro scale and different layer of graphene flakes. This is consistent with the fact that a hydrophobic surface becomes more hydrophobic when microstructured.[76] The change of the contact angle due to surface roughness can be described by $\cos(\theta_W) = R_w \cos(\theta_0)$, where θ_W is the apparent contact angle, R_w is the surface roughness factor, and θ_0 is the contact angle in the Young's mode. [77]

Type of graphene	Contact angle (standard deviation)
Single	92.5° (2.9)
Bi	91.9° (3.4)
Multi	92.7° (2.3)
HOPG	91° (1.0)

Table 3.3 Averaged contact angle of graphene with different number of layers.

3.4 Contact Angle Measurement on Disordered Graphene

In order to investigate the difference of wettability between epitaxial graphene and disordered graphene, we introduced damage and defects intentionally by oxygen plasma treatment. Figure 3.4 summarizes the contact angle measurements on graphene for different

conditions. After oxygen plasma treatment at 5 W for 15 sec, the surface becomes more hydrophilic with the contact angle changing from 92.5° of pristine graphene to 55.1° in Figure 3.4.1(a,b). Oxygen plasma could create vacancies, C-H, sp^3 sites, or OH^- bonding.[59] However, when the plasma power is relatively small (< 2 W) and the exposure time is less than 1 minute, no detectable defect is present in graphene from the Raman and AFM measurements. Moreover, the contact angle is completely recovered from 42.4° with plasma treatment of 2 W for 45 sec whereby no defect is present to 91.6° by dehydroxylation process after annealing at 300 °C in UHV for 30 minutes.[78] We monitored that the contact angle of graphene was changed to 72.4° after one day of oxygen plasma treatment in Figure 3.4.1(c). It is well known that most of the hydrophilic characteristic could be originated from hydroxide introduced by oxygen plasma process.[79] After annealing the plasma treated samples at 300 °C in UHV for 30 minutes, contact angle of graphene has been recovered from 72.4° to 87.3° as shown in Figure 3.4.1(c,d).

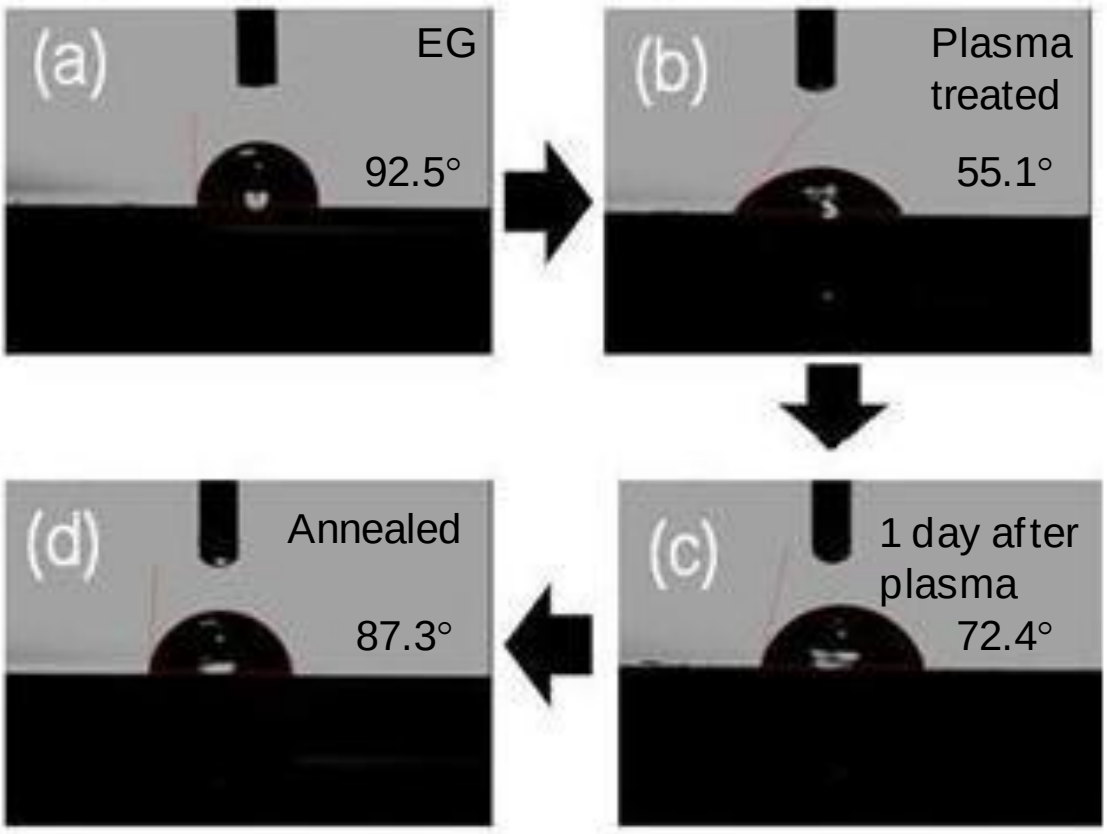

Figure 3.4.1 Water droplet on graphene before plasma treatment (a), after plasma treatment (5 W, 15 sec) (b), 1 day after O_2 plasma treatment (c), and annealed at 300 ^{o}C in UHV for 30 min (d).

It was shown that the contact angle of 92.5° for graphene layer on SiC changes to 70.0° in Fig. 3.3, when the graphene layer was removed by oxygen plasma. With an oxygen plasma condition of 10 W for 2 minutes it is confirmed that graphene on SiC has been completely removed, since the G peak (1597 cm^{-1}) and the 2D peak (2715cm^{-1}) are not present in the Raman spectra as shown in Fig. 3.4.2(a). It was found that there is a significant difference between the etching rate of MCG and EG.[80] When RF power was 5 W and exposure time was 5 seconds, a more pronounced D band from MCG indicates that MCG is more reactive with oxygen plasma in comparison to EG as shown in Fig. 3.4.2(a,b). Since

relatively stronger covalent bond exists between EG and SiC substrate compared to MCG and SiO_2 layer, SiC or buffer layer may hold EG more tightly during oxygen plasma treatment.[81],[82] This is in line with the previous study in which the authors reported very different etching rate for single and multi layer graphene.[80] Since single layer graphene is bonded to SiO_2 more loosely by van der Waals forces as compared to the bonding between graphene layers in mechanically cleaved multi layer graphene, the etching rate of single layer graphene is faster.[80] In the present study, it took about 25 seconds to completely etch MCG with an RF power of 5 W, whereas it took 3 minutes to remove EG at the same RF power.

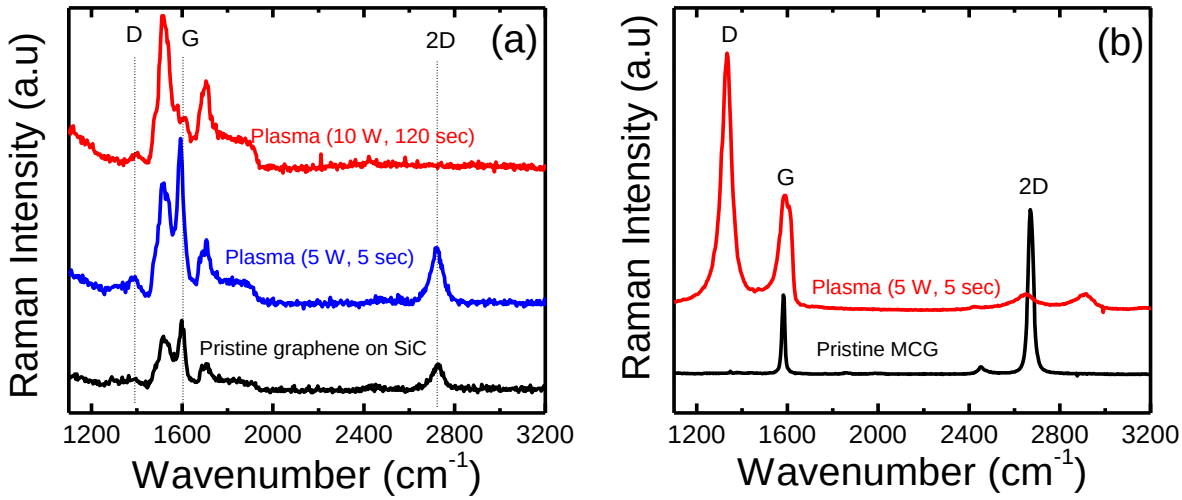

Figure 3.4.2 (a) Raman spectra of EG without and with plasma treatment. (b) Raman spectra of MCG without and with plasma treatment.

3.5 Correlation between Contact Angle and Damage of Graphene

By controlling the exposure time of oxygen plasma, different levels of damage can be introduced on graphene samples. By calculating the integral intensity ratio of the D band to G band, I(D)/I(G), from the Raman spectra, the level of defect on graphene is extracted.[59] It is clear from Fig. 3.5 that the relative intensity of D band to G band increases with increase in exposure time. Fig. 3.5(b) shows that the contact angle generally decreases with an increase in the I(D)/I(G) ratio. The result indicates that the defects, which could be a surface

dislocation, corrugation, interaction of graphene with the substrate or vacancies, have increased the polarity of the surface, therefore the surface energy has increased.[72] Further studies are required to better understand the interaction of oxygen plasma with graphene, since the role of various defects in controlling the contact angle is not clear.

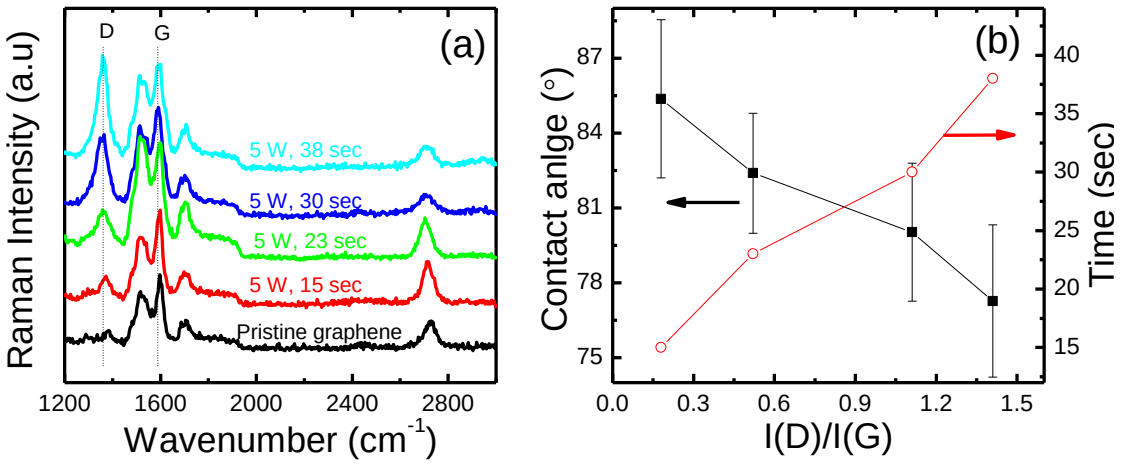

Figure 3.5 (a) Raman spectra of EG treated with 5 W plasma as a function of exposure time. (b) Contact angle versus I(D)/I(G) ratio and I(D)/I(G) ratio versus plasma exposure time.

3.6 Contact Angle Engineering of Graphene

Understanding the surface characteristics and controlling the wettability of graphene are very important for many applications. In contact deposition on top of graphene, without sufficient understanding of the surface characteristics of graphene, the process is not always guaranteed to be successful. For example, Figure 3.6(a) shows the unsuccessful attempt of contact deposition. Most of 5 nm Cr/100 nm Au contact electrodes have been deposited successfully on top of SiO_2, whereas part of the electrodes which is located on the graphene side have been peeled off during the lift-off process. As shown in the contact angle experiments, graphene surface is not adhesive (hydrophobic). By oxygen plasma treatment, we can improve the adhesion property of graphene. It should be noted that oxygen plasma

exposure time and power should be carefully selected in order to minimize the damage on graphene and achieve good adhesion of the contacts at the same time. In the case of 30 sec etching time, a big difference of the I(D)/I(G) ratio, proportional to the level of damage, between 2W and 5W of RF power is shown in Fig. 3.6(b). As we already mentioned, MCG is etched and damaged by oxygen plasma at a faster rate compared to EG at the same power of 2 W. Graphene transforms from hydrophobic to hydrophilic after the oxygen plasma treatment as inferred from the contact angle change from 92° to 10°. For EG, no significant rise of D band has been observed during the entire plasma process indicating no significant damage on graphene when 2 W RF power is used. In contrast, for MCG when exposure time has reached 30 seconds, the D band started rising significantly. This method to control wettability can be combined with the annealing process, which can cure any damage induced by oxygen plasma, thus providing good contact adhesion without compromising the physical properties. Liang *et al*. fabricated graphene transistors without and with oxygen plasma treatment.[83] They reported that oxygen plasma treatment possibly increases the bonding strength, even though the dangling bond generated by plasma treatment could degrade mobility. It is consistent with the results of the present study and can be explained to be a result of the improved adhesion due to the presence of hydroxyl group, which increases the polarity of surface. By choosing appropriate power, less than 2 W in the present study, and time of oxygen plasma, high performance graphene devices can be fabricated with good adhesion between graphene and metal contacts as well as minimal damage to graphene. Choi *et al.* has reported that fabrication yield ratio of metal contacts on graphene is much improved without degrading electrical property of graphene after applying plasma engineering.[93]

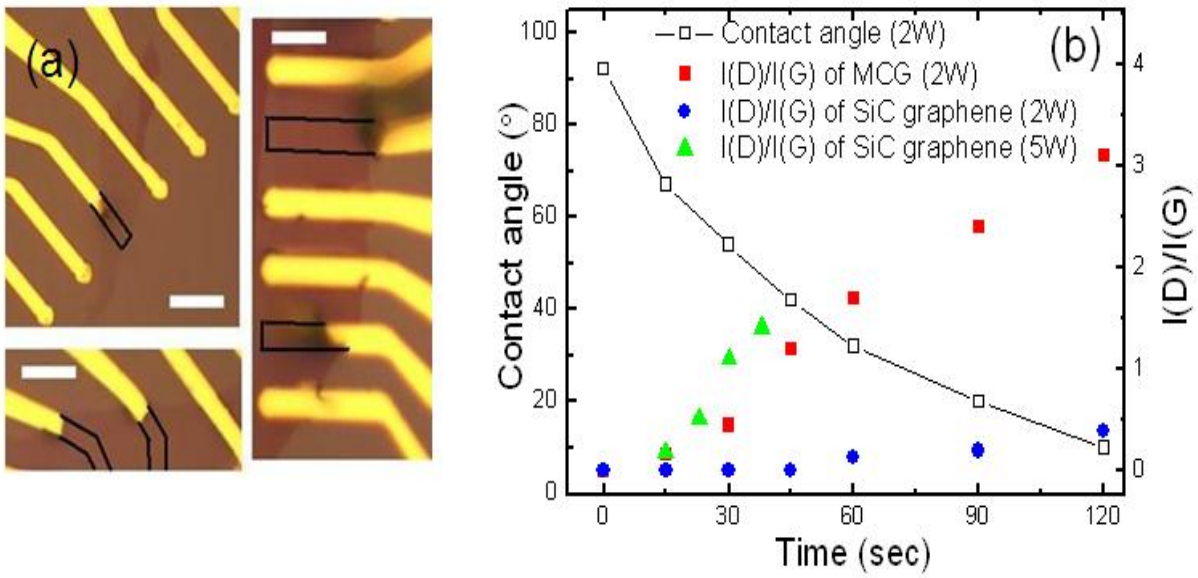

Figure 3.6 (a) Image of graphene devices when part of the electrodes are peeled off after lift-off process (scale bar: 10 μm, electrodes were supposed to be deposited in the area guided by black line). (b) The O_2 plasma exposure time dependence of contact angle and I(D)/I(G) ratio. The plasma power is indicated in brackets.

3.7 Summary

In chapter 3, Contact angle goniometry is conducted for epitaxial graphene on SiC. Single layer epitaxial graphene showed a hydrophobic characteristic similar to HOPG. It is found that there is no thickness dependence of the contact angle from the measurements of single, bi, and multi layer graphene and HOPG. Upon oxygen plasma treatment, defects are introduced into graphene and the level of damage was investigated by Raman spectroscopy. There exists a correlation between the level of defects and the contact angle. As more defects are induced, surface energy of graphene is increased leading to hydrophilic nature. By using low power oxygen plasma treatment, the wettability of graphene is improved without additional damage, which can solve the adhesion issues involved in the fabrication of graphene devices.

4. Ambipolar Bistable Switching Effect of Graphene

In this chapter, current hysteresis in graphene devices is investigated in a two-terminal configuration showing bistable states with a back gate bias to tune the Fermi level of graphene. To explain the observed ambipolar bistable switching effect, we propose charging and discharging effect (CDE). Quantum transport simulations, self-consistently coupled with charging energy calculation, are performed and the results indicate that CDE plays an important role in hysteretic switching. In addition, resistive switching of graphene devices is found to be stable for more than 100 cycles of operation. To improve the ON/OFF ratio of the resistive switching device, various methods, such as band gap engineering and chemical doping, are suggested. By employing this unique ambipolar switching effect, multi-state devices based on graphene are proposed.

4.1 Experimental Details

Single and multi-layer graphene are prepared by micromechanical exfoliation and transferred to a highly p-doped Si substrate, which is covered by a layer of 300 nm thick SiO_2. Mechanically cleaved graphene is identified by optical microscopy and Raman spectroscopy. The electrodes are patterned using standard lithography and Cr/Au (5 nm/80 nm) is deposited by a thermal evaporator, followed by standard lift-off procedures. The *I-V* characteristics of graphene with a two-probe configuration are measured under ambient conditions. To apply a back gate bias, the cathode is connected to the back gate and the leakage current through the SiO_2 layer is monitored.

4.2 *I-V* Characteristic of Two-terminal Graphene and Glassy Carbon

Figure 4.2.1(a) shows the Raman spectra of single and multi-layer graphene samples. From the appearance of in-plane vibrational *G* band (1581 cm^{-1}) and two-phonon 2*D* band (2680 cm^{-1}), single layer graphene can be clearly identified. The number of layers of the graphene sample is determined by measuring the width of the 2*D* band.[60] The inset of Fig. 4.2.1(a) shows the optical image of graphene on top of a Si wafer covered with 300 nm thick SiO_2 after the deposition of Cr/Au contacts. Figure 4.2.1(b) shows the resistance as a function of the back gate voltage. Graphene is found to be p-type without an external electric field, which is seen as a shift of the Dirac point to a positive back gate voltage. The Dirac peak shift can be attributed to unintentional doping such as water molecules.[3] In typical transport experiments of graphene, applying a high voltage between the source and drain is not preferred, as this causes a device breakdown. Some experiments, which applied a high voltage (> 2 V) to graphene devices, reported nonlinear *I*-*V* characteristics similar to our *I*-*V* curves in the insets of Fig. 4.2.1(b).[85-87] The difference in the maximum current density between the forward and backward sweeps is ~ 0.5×10^7 A/cm^2 with a sample width of 4 μm and a thickness of 0.35 nm at ± 4 V. In addition to the nonlinear *I*-*V* curves, current hysteresis is also observed as shown in Fig. 4.2.1(c-f) at different back gate bias. The *I*-*V* characteristics exhibit a typical unipolar (or symmetric) switching behavior, in which the switching procedure does not depend on the polarity of the voltage and current signal. Moreover, we find an interesting phenomenon in which the sequence of switching is reversed, when the charge carrier type is changed by an external bias. As shown in Fig. 4.2.1(c-d), switching starts from a low resistance state and ends up with a high resistance state for both the positive and negative sweeps in the hole transport regime. On the other hand, when the charge carrier becomes electrons as shown in Fig. 4.2.1(e-f), switching starts from a high resistance state and ends up with a low resistance state for both the polarity sweeps. Ambipolar

characteristics at different back gate biases imply that intrinsic physical properties of graphene are responsible for the observed current hysteresis.

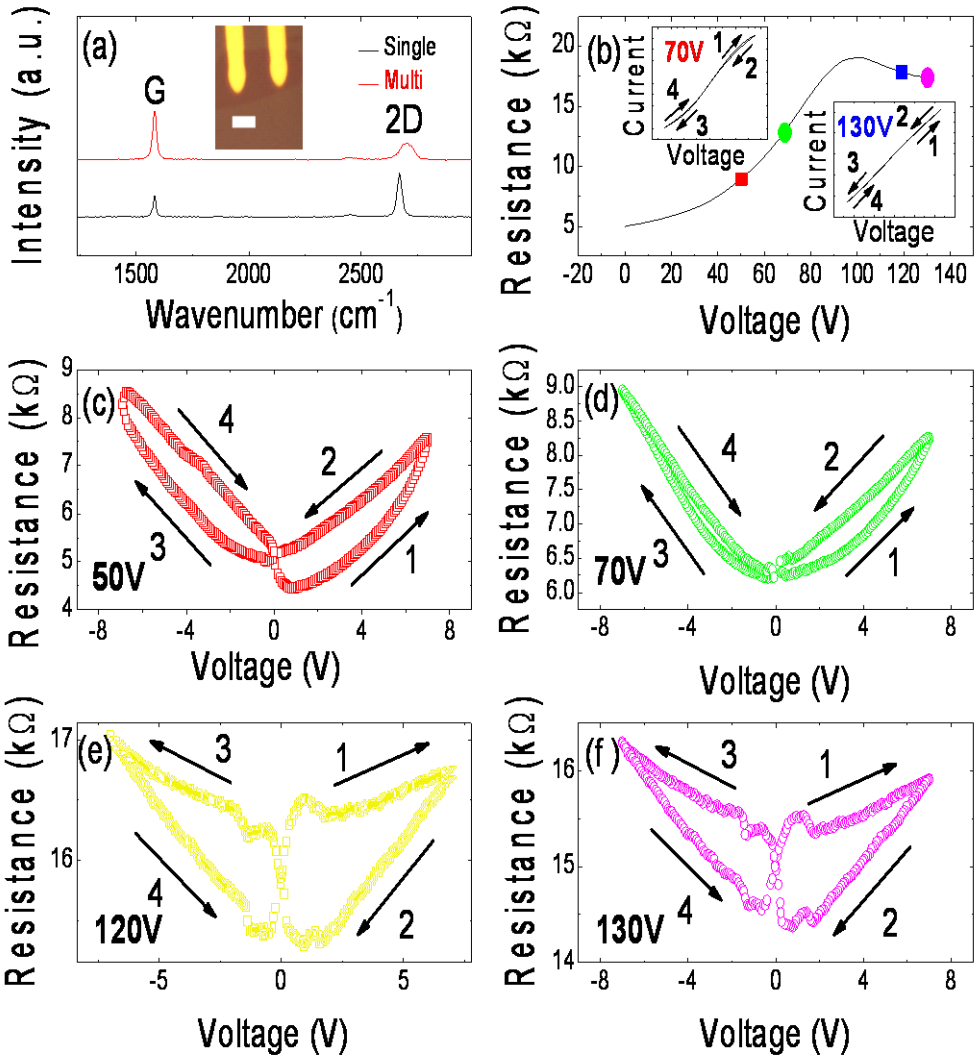

Figure 4.2.1 (a) Raman spectra of single layer and multi-layer graphene. The inset in (a) shows an optical image of a device (scale bar is 3 μm). (b) Resistance vs. back gate voltage (V_g) of a device. The upper and lower insets in (b) show typical *I-V* data in p-type (V_g = 70 V) and n-type (V_g = 130 V) devices. (c-f) Resistance vs. bias voltage at different V_g.

In addition, amorphous glassy carbon films of 2 nm thick deposited by pulse laser deposition are measured to examine any hysteresis switching behavior, shown in Fig. 4.2.2. Thin Au strips without graphene in the lower inset of Fig. 4.2.2 are also tested to check the possible switching effect due to electrical annealing and residual TiO_x.[88] No hysteretic switching is found and linear *I-V* characteristic is observed for both cases, demonstrating that our observation from graphene devices is unique.

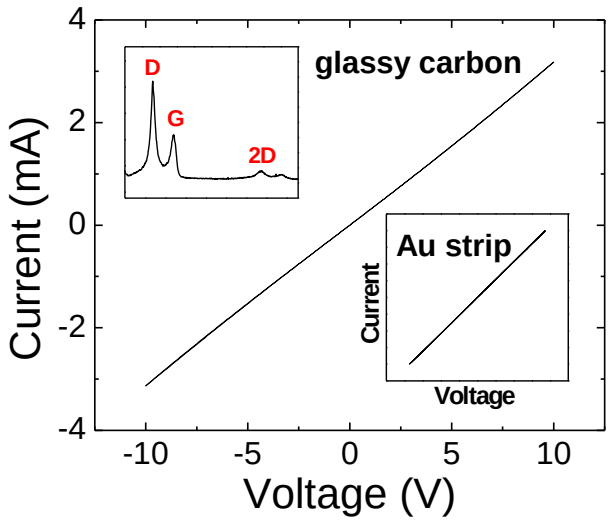

Figure 4.2.2 *I-V* data of a glassy carbon film. The upper inset shows the Raman spectra of glassy carbon and the lower inset shows *I-V* curve of an Au strip.

4.3 Controlled Experiments and Simulation results

In order to verify that CDE is the cause of hysteretic resistive switching, we perform *I-V* measurements in both vacuum (10^{-8} Torr) and ambient conditions. The hysteresis is much weaker under vacuum conditions due to the lack of the charging sources as shown in Fig. 4.3.1 (a). The possible sources of CDE are: 1) unintentional particles between contacts and graphene, which can be introduced during or before the deposition of contacts; 2) particles between graphene and the substrate; and 3) dangling bonds from the edge of graphene. Two

opposite types of CDE sources can be assumed. First, when a bias voltage is applied, the positively charged hydrogens (H^+) or similar polarity groups are removed in the case of p-type graphene, but attached to the n-type graphene surface. Conversely, when a bias voltage is applied, the negatively charged hydroxyl ions (OH^-) or similar polarity groups are detached from n-type graphene, but attached to p-type graphene. The charging energy in p-type graphene increases with bias voltage, which requires a larger change in bias for the same electron conduction, therefore, the current decreases when the bias voltage changes from positive to zero. On the other hand, for the n-type devices, the increase of bias voltage leads to a decrease of the charging energy and an increase of the current in the backward sweep. The difference in current is getting bigger as the range of sweep voltage increases shown in Fig. 4.3.1 (b). This implies that more charging sources become activated with a higher bias, which leads to a larger hysteresis curve.

In order to understand charging discharging effect (CDE), a two-terminal one-level transport model where the carriers flow across the channel via an isolated energy state, is employed, with the device potential obtained self-consistently with charging energy calculation.[89, 90] In this model, the lowest unoccupied molecular orbital (LUMO) conduction or the highest occupied molecular orbital (HOMO) conduction can be considered as n-type or p-type conduction channels, and they are set at 0.2 and -0.2 eV, respectively. Furthermore, the carrier escape rate between the contact and the channel is set to 5×10^{-3} s^{-1} at 300 K. A schematic of the model for HOMO channel conduction is shown in the lower inset of Fig. 4.3.1(c). As the drain bias increases, the chemical potential of the drain moves downwards, and when it is lower than the energy of the channel state, a net current occurs. The charge occupation of the channel state changes from filled to partially-filled and the charging energy is thus changed. The simulated *I-V* characteristics, as shown in Fig. 4.3.1(c), present the hysteresis behavior due to a change in the charging energy as the bias voltage

increases. Moreover, the different patterns of n-type and p-type devices exactly match with the experimental data shown in the insets of Fig. 4.2.1(b). Figure 4.3.1(c) also shows that the simulated hysteresis loop of the p-type device becomes larger, as the sweeping bias increases thus the difference in charging energy increases. The model clearly reveals the physical origin of the hysteresis switching for p- and n-type graphene devices.

The reproducibility of switching effect is tested. Input voltage is repeated in the following sequence: 0V, 4V, 8V, 4V, and 0V, and the output current is measured at 4 V for the forward and backward sweeps. The resistance change ratio, $\Delta R/R = (R_{OFF}-R_{ON})/R_{ON}$ is around 13% in Fig. 4.3.1(d). Even though the ratio of resistance change is small, 100 cycles of operation can be repeated without serious degradation. Yao *et al.* engineered two-terminal nonvolatile memory with single-walled carbon nanotube, and reported that current hysteresis was not observed for metallic carbon nanotube due to the absence of a band gap as can be seen from Fig. 4.3.2.[91] As the electrical characteristic of graphene is similar to that of a metallic system, it is difficult to make a large ON/OFF ratio from graphene, which is a major hurdle for graphene devices.[19] However, by patterning graphene into nanoribbons, a band gap can be induced, resulting in a higher ON/OFF ratio.[2, 40] Furthermore, the band gap of bilayer graphene can be opened up with a gate bias [74], and metallic graphene can be turned into an insulator by chemical doping.[15] As a result, graphene device is expected to take advantage of its high mobility for fast resistive switching memory applications.[29] In addition, by utilizing the observed ambipolar switching effect, graphene devices can be set at multiple states depending on the gate bias voltage, leading to the possibility of multi-bit memory devices.

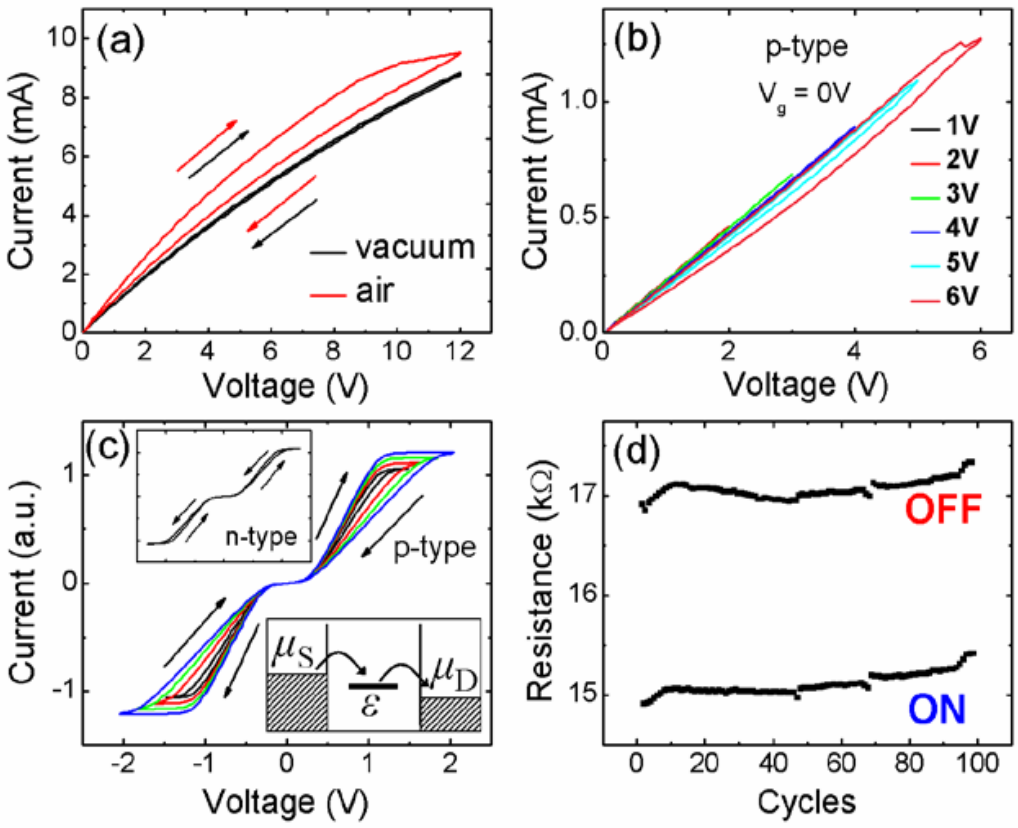

Figure 4.3.1 (a) *I-V* data of p-type graphene in both vacuum and air without a gate bias. (b) *I-V* with different voltage sweep ranges. (c) The simulated *I-V* of p-type graphene devices. The upper inset shows the simulated *I-V* of n-type graphene devices. The lower inset represents the one-level model for simulations with μ_S and μ_D being the chemical potentials of the source and drain. ε is the energy of the conduction state in the channel and the shaded regions are filled with electrons. (d) 100 cycles of ON/OFF switching.

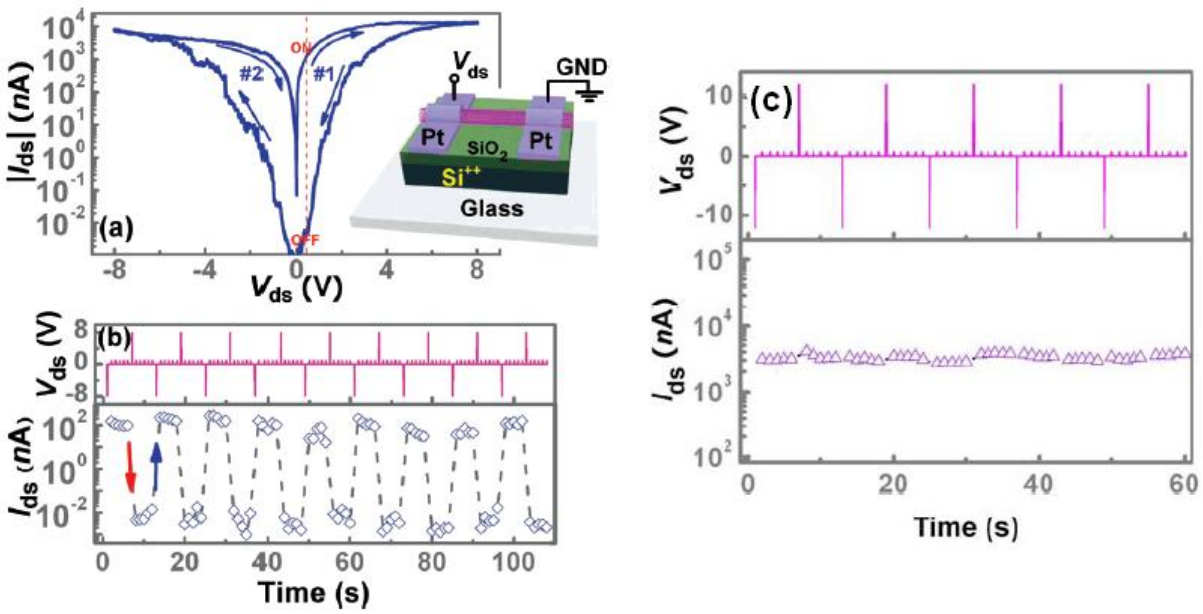

Figure 4.3.2 Both panels represent the same p-type single-walled carbon nanotube (SWCNT) device tested under vacuum. (a) Two-terminal current-voltage (I_{ds}-V_{ds}) evolution in the SWCNT device. (b) (Top panel) A series of programming voltage pulses of -8 and +8 V applied across the device. Between each two neighboring programming voltages, there are five voltage pulses of +0.5 V as reading operations. (Bottom panel) Corresponding memory states (I_{ds}) read out by the +0.5 V pulses shown in the top panel. (c) Top panel: a series of programming voltage pulses of -12 V and +12 V applied across a metallic SWCNT device. Bottom panel: corresponding memory states (I_{ds}) read out by the +0.5 V pulses shown in the top panel. [91]

4.4 Summary

The study of reproducible current hysteresis in graphene is presented in the chapter 4. It has been observed that the sequence of hysteresis switching with different type of the carriers, electron and hole, is inverted and it has been proposed that CDE is the origin for the observed ambipolar switching effect, supported by quantum simulations. In addition, band gap engineering is proposed to improve the ON/OFF ratio of resistive switching. Graphene memory devices can be realised based on the observed hysteretic switching as

semiconducting CNT devices are engineered. Our observation demonstrates an opportunity to realize two-terminal memory devices with well studied three-terminal FET graphene devices on a same graphene based platform if the ON/OFF ratio is improve

5. The Role of Charge Traps in Inducing Hysteresis

It is technologically important to understand the origin of hysteresis in top gated graphene transistors as this will serve a platform for the characterization of high frequency GFET. In all the previous studies, either resistance or conductance as a function of gate voltage is used to understand the origin of hysteresis and there is no report on the hysteresis in capacitance-voltage (C-V) measurements, especially in bilayer graphene. Quantum capacitance, a property of low dimensional systems, is proportional to the density of states and the capacitance measurements are very useful in detecting localized states of disordered systems, whose contribution to conductivity is suppressed.

5.1 Experimental Details

The graphene is obtained by micromechanical exfoliation of Kish graphite subsequently transferring it to a highly p-doped Si substrate, which has a layer of 300 nm thick SiO_2. The resultant graphene is identified by an optical microscope and confirmed by Raman spectrophotometer.[92, 93] Electrodes are prepared by optical lithography followed by the deposition of Cr (5 nm)/Au (150 nm) using a thermal evaporator. Standard lift-off procedures are followed after the deposition [see Fig. 5.2(a)]. For the top gate fabrication, similar procedures are followed and a 10 nm of Al is deposited in two steps followed by natural oxidation. The complete oxidation of Al is verified via X-ray photoelectron spectroscopy (XPS). Figure 5.2(b) shows the Raman spectrum of pristine graphene. The spectrum shows prominently the G peak along with a 2D peak. A Lorentian fit of a 2D peak in the inset of Fig. 5.2(b) estimates the full width at half maximum as 50 cm^{-1}, indicating bilayer graphene. The

sample has no detectable D peak suggesting the absence of microscopic disorder in the graphene channel.

5.2 Hysteresis of Capacitance of Top Gated Bilayer Graphene

In order to understand the electron transport properties, measurements are carried out in two point geometry and under high vacuum (< 1×10^{-7} Torr) conditions. Figure 5.2(c) shows the channel resistance R_{xx} between source (S) and drain (D) as a function of top gate (G) voltage, V_{TG} at 300 K. The top gate voltage is continuously varied from 0 to 1 V, then to -1 V and finally back to 0 V. The bias voltage range is extended to ±2 and ±3 V with the same sweeping sequence. Each hysteresis loop is repeated twice to confirm the reproducibility of the results. Two important points are noticeable in the figure; (i) charge neutrality point (CNP) corresponding to maximum resistance in the R_{xx} vs. V_{TG} graph is not at zero, but depends on the extent of the applied V_{TG}, (ii) the area under the hysteresis is a function of the extent of the V_{TG}. When a positive V_{TG} is applied, the accumulation of electrons in charge traps causes the maximum of R_{xx} to be on a positive bias voltage. With negative V_{TG} due to the injection of holes into charge traps, CNP is shifted towards more negative voltage. The larger the applied positive (negative) voltage, the more the accumulation of electrons (holes), which lead the CNP to depend on the magnitude of the applied voltage. The occupancy of the traps depends on the maximum applied voltage which in turn determines the shift in CNP, whereas the area under the hysteresis is determined by the number of traps charged on applying a definite voltage. The trap density is calculated from the shift of the CNP (ΔV_{NP}) from zero gate voltage using the relationship, $n_{it}=C_{ox}\Delta V_{NP}/2e$, where C_{ox} is the geometric capacitance per unit area (for Al_2O_3, the dielectric constant is 8 and the thickness is 10 nm) and e is the charge of an electron. For a maximum gate voltage of 3 V, n_{it} is estimated to be ~ 5×10^{11} cm^{-2} which is in agreement with the

reported results on the magnitude of the charge density inhomogeneity (2-15×10^{11} cm^{-2}) in single and bilayer graphene.[94-96]

To further understand the origin of hysteresis, capacitance measurements are performed. Figure 5.2(d) shows the measured capacitance (C) with top gate as one electrode and source as the ground electrode as a function of V_{TG} at 300 K. The capacitance behavior is similar to the reciprocal of R_{xx} and is also a function of the extent of the applied V_{TG}. The identical nature of C and $1/R_{xx}$ indicates that the appearance of hysteresis and existence of different CNPs is due to a capacitive source and we find that, as we discuss later, charge traps present at the graphene/gate oxide interface are causing these effects.

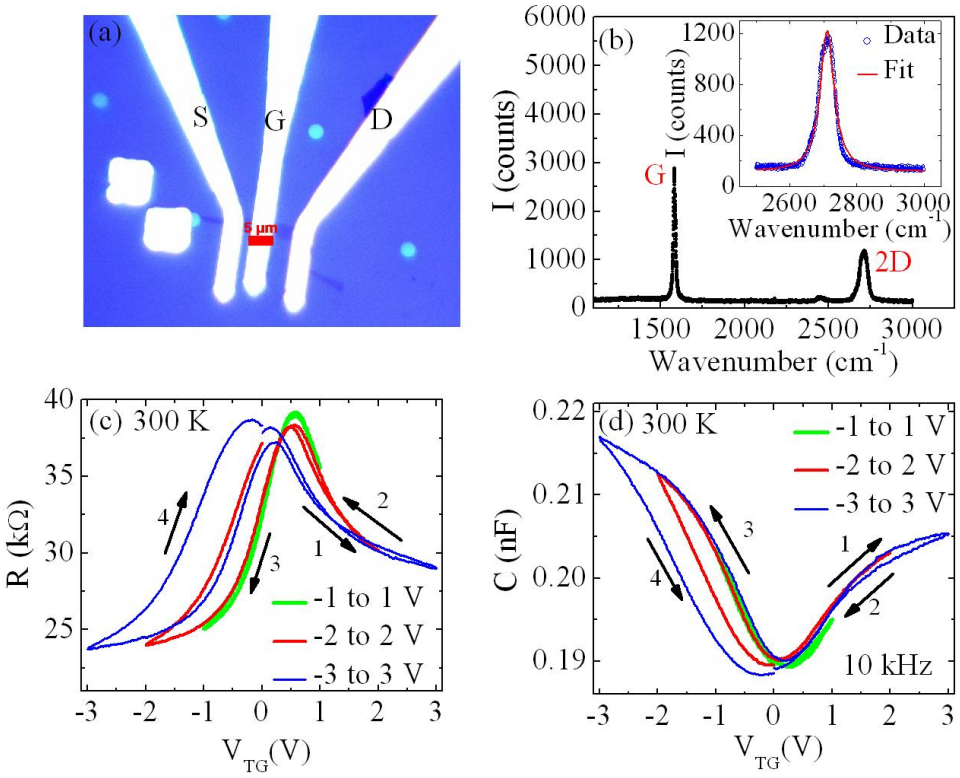

Figure 5.2 (a) Optical micrograph of the patterned graphene device (scale bar: 5μm). In the figure "S" stands for source, "G" for top gate, and "D" for drain. (b) Raman spectrum of bilayer graphene. The inset in (b) shows the 2D peak along with a theoretical fit. (c) Channel resistance (R_{xx}) vs. top gate voltage (V_{TG}) of the bilayer graphene at 300 K. The measurements are done at different range voltages. (d) Capacitance (C) vs. V_{TG} at 300 K performed at 10 kHz with an AC amplitude of 500 mV.

5.3 Low Temperature Measurements and Frequency Dependence

The different contributions to the total capacitance C is decomposed into the top gate oxide capacitance (C_{ox}), in series with the quantum capacitance of graphene (C_Q) and the trap capacitance (C_{tr}). It is known that C_{ox} is constant and independent of the applied gate voltages, whereas the graphene quantum capacitance C_Q is a measure of the response of the charges inside the channel to the change in the density of states of conduction and valence bands. Figure 5.3(a) shows the two probe resistance R_{xx} as a function of V_{TG} at 3.8 K, indicating that the hysteresis is still present at 3.8 K. A hysteresis was observed in graphene by other groups at ambient conditions, but it was suppressed either by introducing vacuum or cryogenic temperatures suggesting the removal of attached molecules in graphene.[97-100] In our samples, the hysteresis still exists even after exposing to the above conditions implying that chemical attachment is not a dominant source of the hysteresis. Figure 5.3(b) shows the measured C as a function of V_{TG} at 3.8 K, showing a similar behavior with $1/R_{xx}$ as observed at 300 K.

Figure 5.3(c) shows the total C between gate and source as a function of frequency f and V_{TG} at 300 K. The capacitance shows a sharp reduction, when f increases from 1 kHz to 20 kHz, but the values remain almost constant for f > 20 kHz. A sharp fall at f ~ 10 kHz suggests that the charging and discharging time for the interface trap on graphene/Al_2O_3 is ≥ 100 μs. A recent study of graphene on SiO_2 estimates trapping time constants of 87 μs - 1.6 ms which is in good agreement with our result.[101] It is interesting to note that the trap time constant in graphene/oxide is much larger than that of Si/gate oxide (< 1μs).[102] Figure 5.3(d) shows the total capacitance between gate and source as a function of V_{TG} at 100 kHz and 1 MHz. The capacitance does not follow V_{TG} in contrast to that of low frequencies, which implies that electron trapping cannot follow the speed of band movements at high frequencies.

This result suggests that the trapping speed can be very different depending on the type of the carriers (electrons or holes).

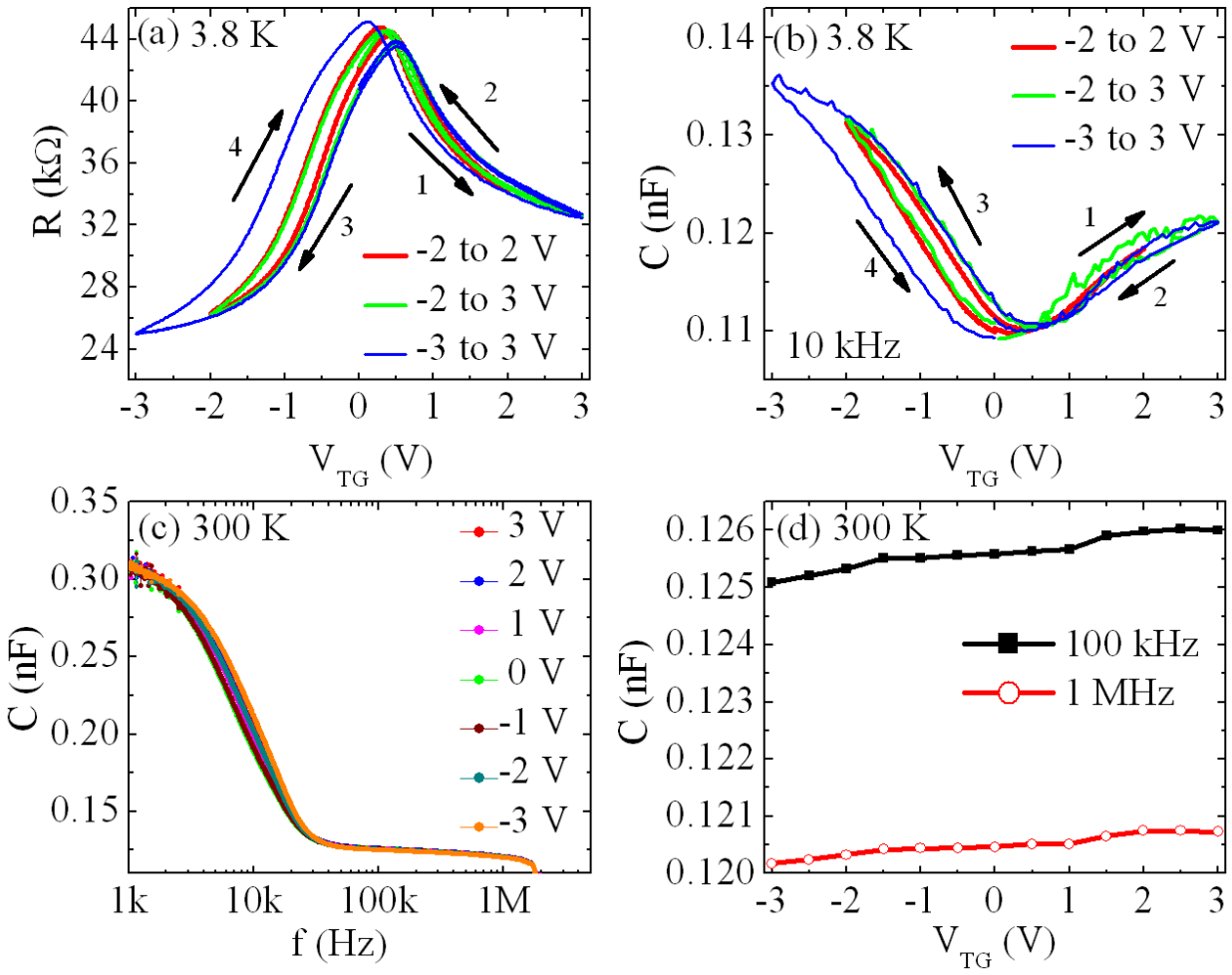

Figure 5.3 (a) Channel resistance (R_{xx}) vs. top gate voltage (V_{TG}) at 3.8 K. (b) Capacitance (C) vs. V_{TG} at 3.8 K. The measurements in (b) are performed at 10 kHz and an AC amplitude of 500 mV. (c) C vs. frequency f as a function of V_{TG} at 300 K. (d) C vs. V_{TG} at f = 100 kHz and 1 MHz at 300 K.

5.4 Hysteresis of Quantum Capacitance and Controlled Experiments

Figure 5.4(a) shows C measured at 10 kHz between source and drain terminals as a function of the channel bias voltage, V_{CH} at 300 K. The C does not show any hysteresis with a very small change of the C value with V_{CH}. This suggests that the hysteresis observed in the

top gated configuration across the gate oxide is not related to graphene but to the graphene/Al_2O_3 interface. Figure 5.4(b) shows an abrupt increase in C when V_{CH} increases beyond 2.5 V. A sudden increase in C suggests that it may be related to the topological changes in the Fermi surface due to an increase in order.[103] The asymmetry of the band structure when next-near neighbor hoping is considered can also explain this result.[104] To understand this behavior, we theoretically calculated the density of states of bilayer graphene which is shown in the inset of Fig. 5.4(b). The shape of C versus V_{CH} qualitatively agrees with the density of states. However, the detail dependence including the anomaly above 2.5 V needs to be understood. Figure 5.4(c) shows R_{xx} vs. V_{TG} at different sweep rates at 300 K. The rate of V_{TG} sweep is varied by changing the hold time between successive V_{TG} increments. The hysteresis is not dependent on the sweep rate, as all the curves are falling on the same curve. This indicates that interface traps are charged in time scales much smaller than the sweep speeds. Figure 5.4(d) shows R_{xx} vs. V_{TG} at different sweep rates at 300 K with an opposite sweep direction to that in Fig. 5.4(c). It shows that the hysteresis is not dependent on the sweep direction, neither the sweep rate. The inset of Fig. 5.4(d) shows R_{xx} as a function of temperature (T) with V_{TG} = 0. The sample shows a metal to insulator transition at a temperature ~ 248 K which indicates that the sample may consist of electron-hole puddles, which is often reported from low mobility samples.[105] If Joule heating is the origin of the hysteresis, the direction of the hysteresis loop should be opposite below and above 248 K. The direction of the hysteresis loop in the top gated sample is the same at different temperatures as shown from Fig. 5.2 (c) and Fig. 5.3(a), indicating that Joule heating is not playing any role in inducing the hysteresis as this could have caused a change in the sequence of the hysteresis loop at 300 and 3.8 K.

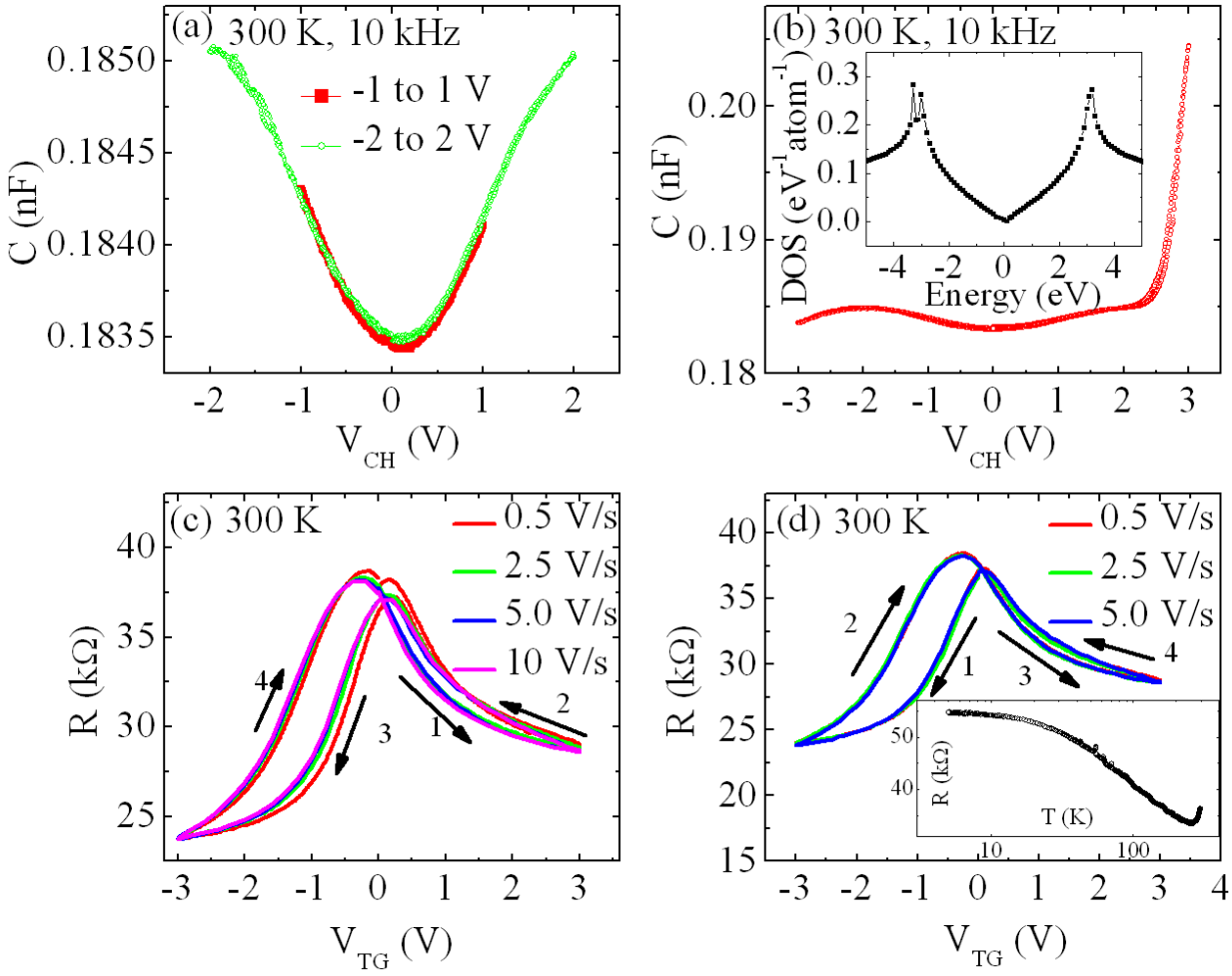

Figure 5.4 (a) Capacitance (C) vs. source-drain voltage (V_{CH}) at 300 K. (b) C vs. V_{CH} in the range of -3 to 3 V at 300 K. The measurements of C are performed at 10 kHz and an AC amplitude of 200 mV. The inset in (b) shows the density of states (DOS) of the bilayer graphene as a function of energy. Plot of channel resistance (R_{xx}) vs. top gate voltage (V_{TG}) at 300 K at different sweep rates (dV/dt) in one sweep direction (c) and the opposite sweep direction (d) of the loop indicated by arrows. The inset in (d) shows R_{xx} vs. temperature (T).

5.5 Summary

In chapter 5, hysteresis of the top gated bilayer graphene field effect transistors is investigated. Capacitance - voltage measurements on top gated bilayer graphene indicates that the origin of hysteresis in the channel resistance is due to charge traps present in the graphene/Al_2O_3 interface with a charging and discharging time constant of ~100 μs. On the

other hand, the measured capacitance of graphene between source and drain with source-drain voltage does not show any hysteresis. It is also observed that the hysteresis is present even at high vacuum conditions and cryogenic temperatures indicating that chemical attachment is not the main source of the hysteresis.

6. Tunneling Characteristics of Graphene

Although graphene has superior physical properties such as very high mobility (Fermi velocity $v_F \sim 10^6$ m/s), a low ON/OFF ratio due to its semi-metallic property prevents graphene from being engineered as logic and memory devices. Two-terminal devices coupled with a nonlinear current-voltage (*I*-*V*) characteristic can be a solution to overcome this shortcoming.

6.1 Experimental Details

Mechanical exfoliation is used to prepare single and multi-layer graphene.[3] Mechanically cleaved graphene is transferred to a highly p-doped Si substrate covered by a 300nm thick SiO_2 layer. Number of layers and quality of graphene is determined by Raman spectroscopy. Electrodes are patterned by standard lithography and Cr/Au (5 nm/80 nm) is deposited by a thermal evaporator. The contact deposition is followed by standard lift-off procedures. The *I*-*V* measurements with a two-probe configuration are carried out with a closed cycle helium cryostat under a base pressure of less than 1×10^{-8} Torr at 3.8 K.

6.2 Negative Differential Conductance of Graphene

Single and multi-layer graphene samples are identified by Raman spectra as shown in Fig. 6.2(a) and the transport data from single layer graphene are reported in this chapter. In-plane vibrational *G* band (1580 cm^{-1}) and two-phonon 2*D* band (2670 cm^{-1}) are clearly visible without any indication of disorder *D* band peak and the number of layers of the graphene sample is determined by estimating the width of 2*D* peak. [60] Figure 6.2(b) shows the two-terminal resistance as a function of back gate voltage. From the shift of the Dirac point to the positive side of the applied back gate voltage, graphene is identified to be hole dominant. The

Dirac point is shifted due to unintentional doping such as the adsorption of water molecules making graphene p-type. [3] The inset of Fig. 6.2(b) shows the optical image of a graphene device on top of a Si wafer with 300 nm thick SiO_2 after the Cr/Au electrode deposition. The inset of Fig. 6.2(c) shows the typical linear *I*-*V* curve with the low bias voltage less than 2 V in graphene devices. As shown in Fig. 6.2(c), the *I*-*V* curve is linear at a low bias voltage, but becomes non-linear and slightly hysteretic at a higher bias.[106] Also the current starts to decrease, as the applied voltage is continuously increased above 6 V. When the current reaches a maximum ($dI/dV = 0$), the current density is $\sim 1.9\times10^8$ A/cm^2 with a sample width of 16 μm and a thickness of 0.35 nm. When the *I*-*V* curve is numerically differentiated, we can clearly identify a negative differential conductance behavior as shown in Fig. 6.2(d). This negative differential conductance might be attributed to the self-heating effects caused by strong electron scattering due to hot non-equilibrium optical phonons similar to what is observed in carbon nanotubes. [107]

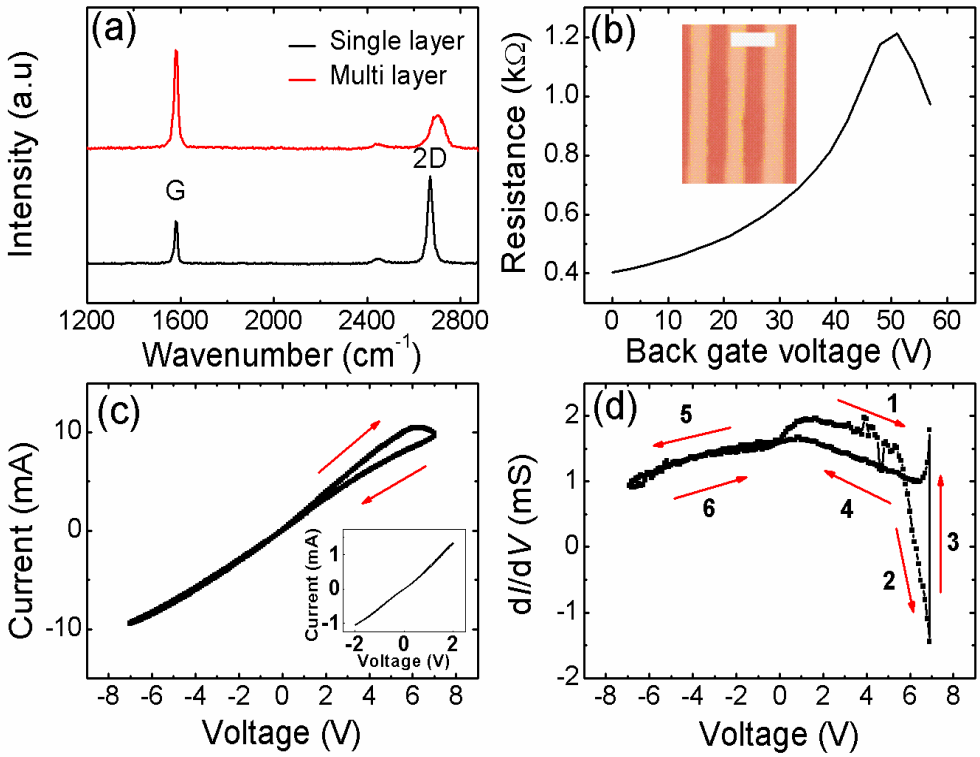

Figure 6.2 (a) Raman spectra of single layer and multi-layer graphene. (b) Resistance vs. back gate voltage of a graphene sample. The inset in (b) shows the optical image of graphene with gold contacts (the scale bar is 8 μm). (c) *I-V* curve in the high bias range. The inset in (c) shows *I-V* curve in the low bias range. (d) Differential conductance versus bias voltage.

6.3 Tunneling effect of graphene

After the observation of negative differential conductance, the sweep voltage is increased further to induce a breakdown in graphene channel as was reported recently that graphene nanoribbons exhibit a breakdown current density, on the order of 10^8 A/cm^2.[108] As can be seen in Fig. 6.3(a), the voltage sweep is halted as soon as the breakdown occurs. Fig. 6.3(b) shows non-linear *I-V* behavior of graphene devices instead of linear increase in current with increasing the bias voltage, when graphene undergoes the breakdown. It can be clearly seen in the logarithmic scale that current starts increasing drastically, when the bias

exceed the threshold voltage of 7 V as shown in Fig. 6.3(c). After the measurement, graphene is examined by Raman spectroscopy and we find out that crystalline graphene is converted to disordered graphene. Interestingly, this disordered system is very different from typical disordered graphene created by an oxygen plasma treatment. Compared to the typical disordered system, the transformed graphene by an electrical breakdown has mixed phases such as amorphous-like (the upper inset of Fig. 6.3(a)) and graphene-like (the lower inset of Fig. 6.3(a)) phases. From the investigation by Raman spectroscopy, the breakdown can be considered as a "deforming process", which is the opposite concept of the forming process, the change in the spatial distribution of oxygen ions by applying the bias voltage, in the oxide resistance switching devices.[109] The deforming process introduces randomly distributed energy barriers caused by amorphous-like phase in the graphene channel. A Raman imaging system is employed to investigate the details of the mixed phase graphene channel. The Raman images are plotted as the intensity of *D* and 2*D* band clearly show amorphous-like phase across the channel which is introduced by the breakdown. Since the deformed channel does not have a continuous current path after the breakdown, the charge carriers of graphene should go over the energy barrier due to the amorphous phase regime. As shown in Fig. 6.3(b) resistance is very high (5.15×10^{10} Ω at 3 V), below 7 V because the charge carriers have to tunnel through the barrier. On the other hand, resistance dramatically decreases to a lower value (7.45×10^{7} Ω at 15 V) under a high bias, due to the decrease of the effective tunneling width of the barrier caused by the electric field as sketched in the inset of Fig. 6.4(a). As a result, more carriers will tunnel through the barrier resulting higher currents. To strengthen this hypothesis, the *I-V* characteristics of a one-dimensional single-square barrier between two metal contacts are simulated based on non-equilibrium Green's function approach. The barrier height and width are set to 6 eV as the Fermi level (E_F) of graphene with respective to the vacuum level, and 1 nm, respectively. We find that its *I-V* characteristics in Fig. 6.4(a) are

similar to the experimental results, and it indicates that the tunneling effect contributes the diode-like *I-V* characteristics.

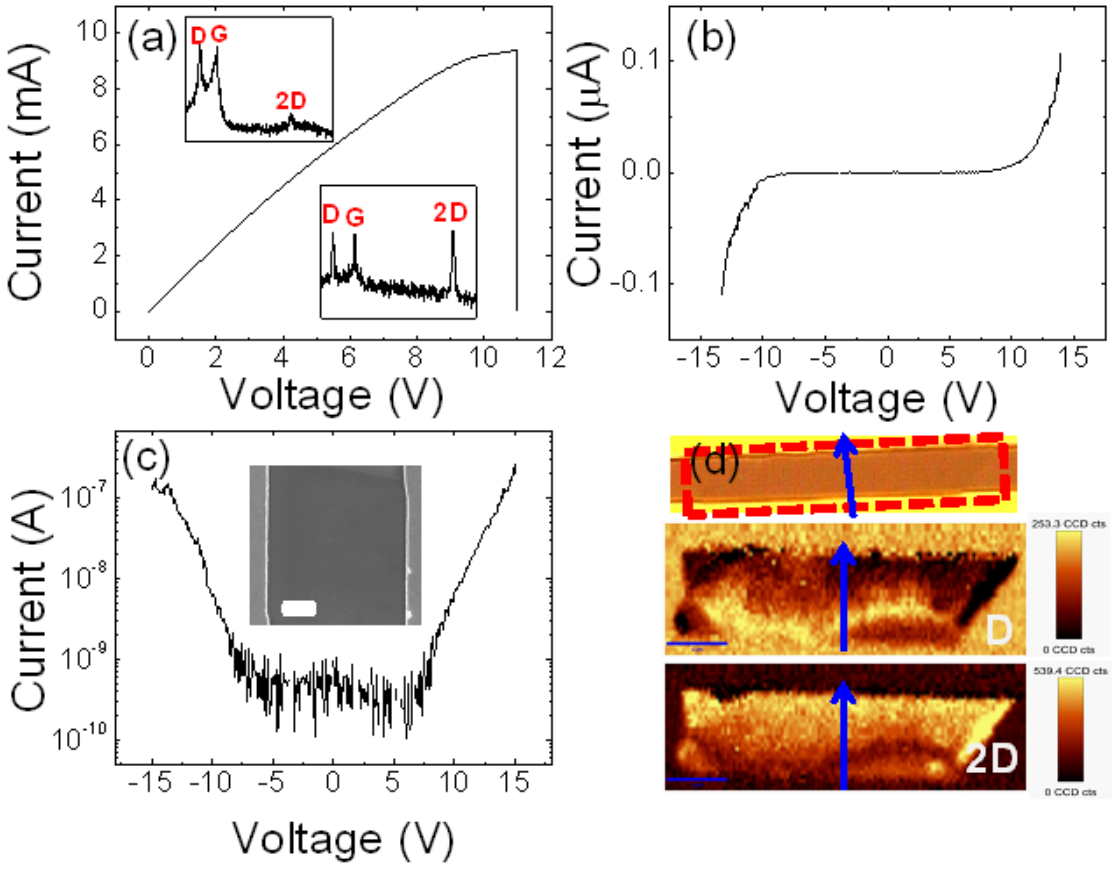

Figure 6.3 (a) *I-V* curve through an electrical breakdown. The insets in (a) show different Raman spectra measured at two different locations in the graphene channel after the breakdown. (b) *I-V* curve after breakdown. (c) Absolute value of current as a function of bias voltage in a logarithmic scale. The inset in (c) shows a scanning electron microscopy image of the graphene channel after the breakdown (the scale bar is 1 μm). (d) Optical image of the sample (top panel) and Raman images plotted by the intensity of D and 2D band (the scale bar is 4 μm). The dotted red line indicates the area of Raman imaging. The blue arrows show the direction of current flow through the graphene channel.

6.4 Material Characterization by Raman Spectroscopy and Switching Effect

The reproducibility of the tunneling diode effect is tested in the other sample by sweeping voltage several times from -6 to 6 V. It is reproducible with slight degradation as shown in Fig. 6.4(b). Degradation in the tunneling behavior is due to the enlargement of the barrier width caused by Joule heating. More than 20 devices are tested and it turns out that each device has a different threshold voltage, since the breakdown is a random process. When the bias voltage is swept for even higher bias in the tunneling regime, current hysteresis is observed as plotted in Fig. 6.4(c). The range of the ON/OFF ratio is from 1000% to 100000%. Current hysteresis is repeatable but degraded gradually. To understand better and engineer the current hysteresis from the mixed phase channel, further studies are required. In order to verify the unique nature of disordered graphene by the breakdown, we further study the *I-V* characteristics from other carbon thin films. For this a 2 nm thick glassy carbon film is deposited by pulsed laser deposition and tested in the same measurement conditions. From the inset of Fig. 6.4(d), the structure of deposited glassy carbon, strong *D* peak and weak 2*D* peak in Raman spectra, is similar to the structure of graphene after the breakdown. However, a complete mapping by Raman spectroscopy reveals that the glassy structure is very uniform unlike to the disordered graphene by the breakdown. When a high bias is applied across the glassy carbon channel, linear *I-V* characteristics are observed in Fig. 6.4(d), which demonstrates that the tunneling characteristic is a unique property of non-uniform disordered graphene. If the tunneling behavior in resistance of Fig. 6.3(b) is caused by electrical annealing, it should not be reversible and reproducible. [110] Non-linear *I-V* characteristics of graphene and carbon nanotubes due to a mechanical discontinuity have been reported.[111-113] We carefully check all our devices by scanning electron microscopy after the breakdown, but any mechanical discontinuity is not found as can be seen in the inset of Fig. 6.3(c).

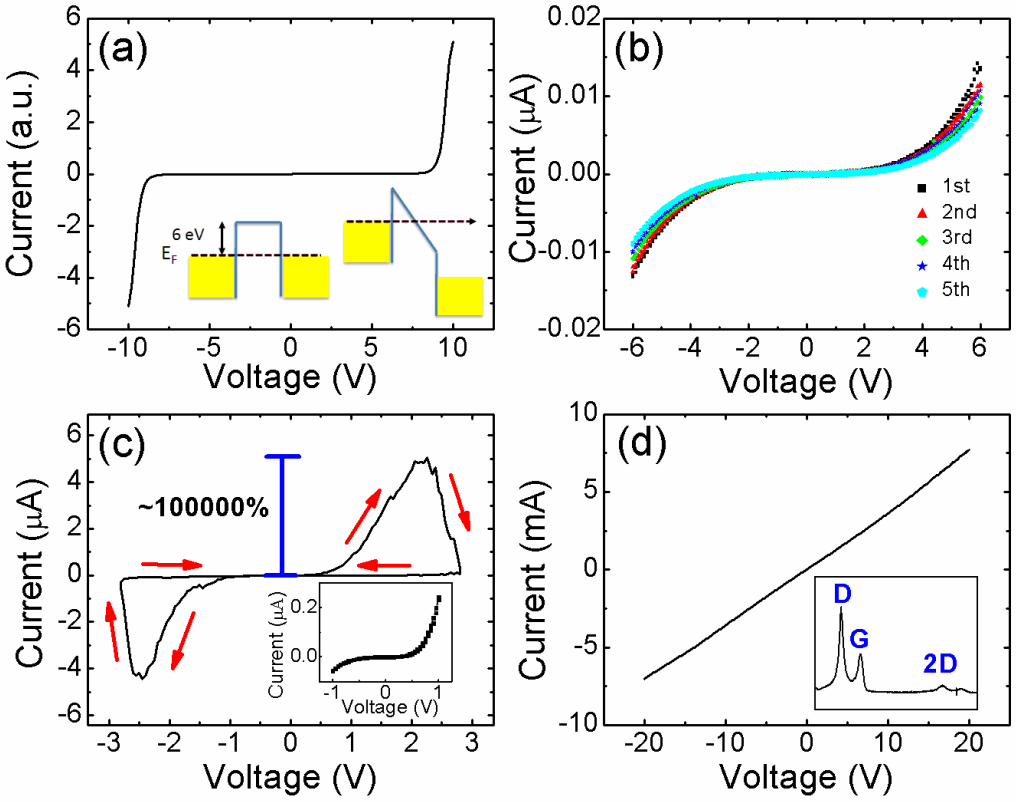

Figure 6.4 (a) Simulated *I-V* data. The insets show the energy diagrams of disordered graphene system without and with the bias voltage. (b) Repeated *I-V* curves after the breakdown. (c) *I-V* curve in the high bias range after the breakdown. The inset in (c) shows *I-V* curve in a low bias range after the breakdown. (d) *I-V* curve of a glassy carbon film. The inset in (d) shows the Raman spectra of glassy carbon.

6.5 Summary

In chapter 6, the tunneling characteristic of graphene from the two-terminal devices after the breakdown is studied. Negative differential conductance is also found when a high voltage bias is applied. The tunneling behavior could be attributed to the formation of non-uniform disordered graphene. The non-uniform disordered structure can introduce energy

barrier in graphene channel. A 2 nm thick glassy carbon film, which is uniformly disordered, deposited by pulsed laser deposition is compared and linear *I-V* characteristics of grassy carbon prove that the tunneling characteristic is a unique property of non-uniform disordered graphene.

7. Stochastic Nonlinear Electrical Characteristic of Graphene

Graphene has been obviously spotlighted for its outstanding properties. Consequently, major electronics companies have already started commercialization activities including a pilot line for large scale graphene growth. However, is graphene really qualified for the real application? Graphene is known as good candidate for chemical or gas sensor due to its large surface to volume ratio. It has been demonstrated that graphene are capable of detecting individual gas molecules. Is graphene suitable for electrical contacs in terms of stability if graphene is very sensitive material? It has been studied that the insulating state of bi-layer graphene can be converted to the metallic state by exposing pristine bi-layer graphene into atmosphere. Maintaining stable electrical properties under various circumstance, especially for long term use with an operational enough bias, is very crucial for graphene to be integrated into display electronics as transparent contacts. Therefore, the stability and reliability of graphene should be investigated more carefully and understood more deeply since the commercialized electronics do not allow a single malfunction.

7.1 Experimental Details

Two-terminal graphene devices with a back gate are fabricated on top of highly p-doped Si substrates covered by a 300 nm thick SiO_2 layer as shown in the inset of Fig 7.2.1(a). Mechanically exfoliated single and multi layer graphene is utilized in this study and we are able to observe the nonlinear switching effect regardless of the number of graphene layer. The quality of graphene is checked with optical microscopy, AFM, and Raman spectroscopy.

For the device fabrication, optical and e-beam lithography are used for electrode patterns and Cr/Au (5 nm/120 nm) is deposited by a thermal evaporator, followed by lift-off.[84]

7.2 *I-V* Characteristic of Two-terminal Graphene

Figure 7.2.1(a) shows many experimental *I-V* switching curves from a single device. The bias voltage is swept from 0 to 3 V and back to 0 V between source and drain with zero back gate bias, repeatedly under ambient conditions. The random transitions between a low-resistive, metallic state and a high-resistive, insulating state are observed. The three most representative switching phases from *I-V* traces in Fig. 7.2.1(a) are plotted separately in Fig. 7.2.1(b-d). For example, an ON-OFF transition in Fig. 7.2.1(c) represents that the device starts from an ON state when the bias voltage increases from zero voltage, and it ends with an OFF state when the voltage sweeps back to zero bias. The resistance of two-terminal graphene devices is ~a few kΩ when it is in metallic (ON) state, whereas the resistance is higher than a few MΩ in the insulating (OFF) state.

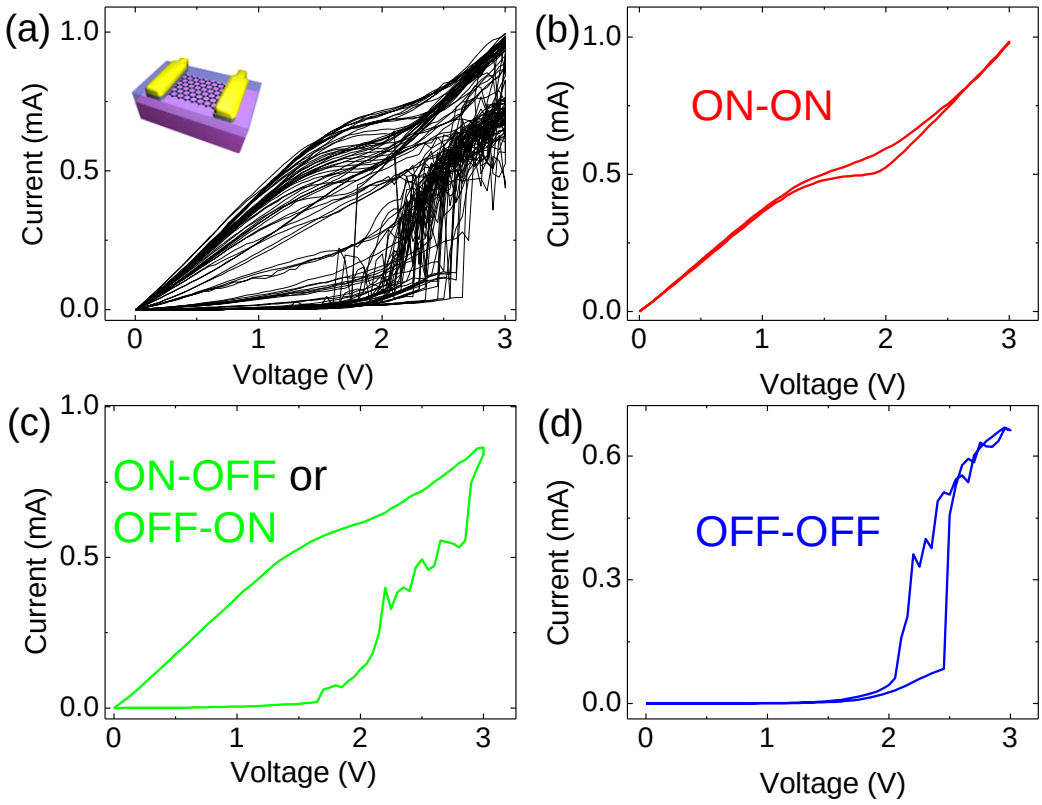

Figure 7.2.1 (a) Experimental *I-V* curves of a two-terminal single layer graphene device. The inset in (a) shows a schematic of graphene device. Three most representative switching phases: (b) ON-ON, (c) ON-OFF (or OFF-ON), and (d) OFF-OFF.

The transition can be more clearly seen, when the *I-V* data are plotted in a logarithmic scale as shown in Fig. 7.2.2(a). The difference of the current between ON and OFF states is more than three orders of magnitude. When the resistance of the device is plotted as a function of measurement time in Fig. 7.2.2(b), there are random transitions among three switching phases and a switching histogram of phases is shown in Fig. 7.2.2(c). From the statistical study, the ON-OFF (or OFF-ON) phase is found to be less frequent than either the ON-ON or OFF-OFF phase. Fig. 7.2.2(d) shows the resistance as a function of back gate bias at two different states; ON and OFF. The charge carrier density of graphene is 4×10^{12} cm^{-2} at

zero back gate bias in a metallic state. The junction resistance at a metallic state follows a well-defined typical p-type Dirac curve (black line). On the other hand, a negligible change due to the back gate voltage is found in an insulating state (red line). A Dirac curve is observed again, when the phase is changed back from insulating to metallic by voltage sweep (black dots), demonstrating reliable transitions between two ON and OFF states.

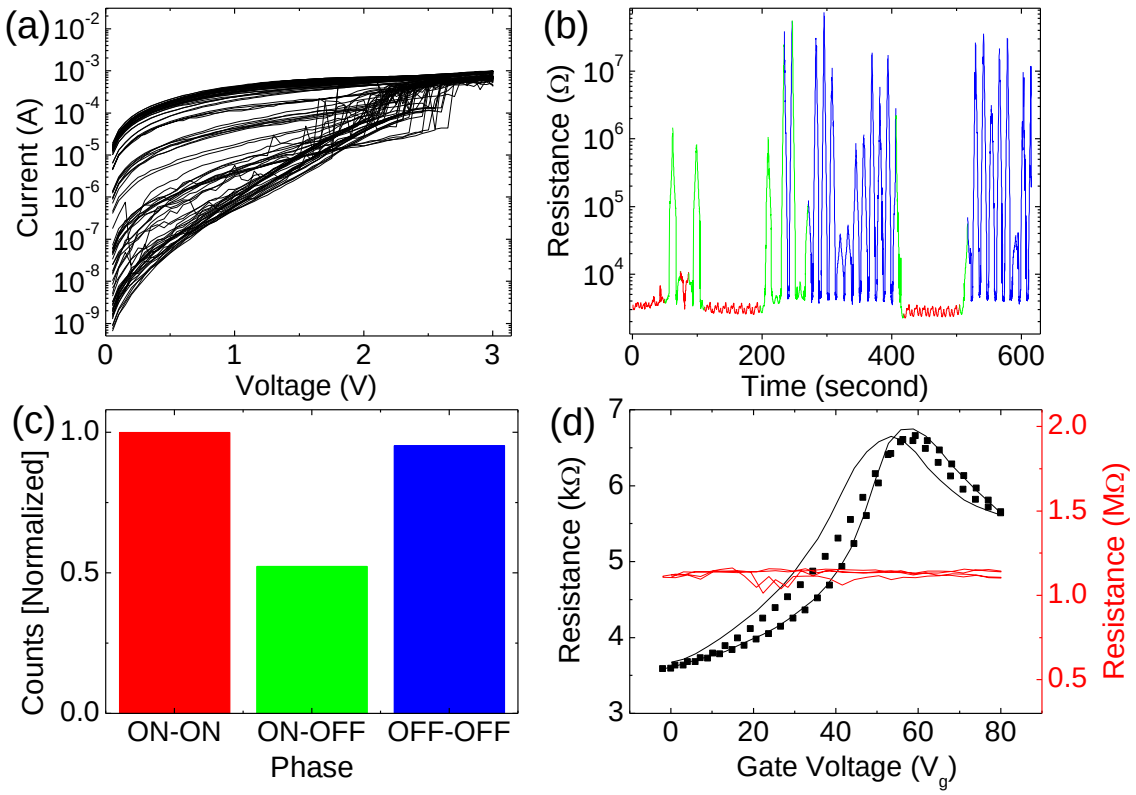

Figure 7.2.2 (a) Current as a function of the channel bias voltage in a logarithmic scale. (b) Resistance as a function of measurement time. (c) A histogram of three representative phases. (d) Resistance versus back gate voltage (V_g) of a device in metallic and insulating phases.

7.3 Characterization of Graphene Channel and Theoretical Supports

It is well known that graphene can be easily influenced by external doping sources such as absorbed molecules.[3] An opposite sequence of current hysteresis originated from attaching and detaching active radicals from the air has been reported.[97] Tunable metal-insulator transitions (MIT) in bilayer graphene caused by water vapors has been also found.[105] Electrochemical reactions caused by active radicals can be a key to elucidate the origin of the observed stochastic nonlinear effect. In order to understand the underlying mechanism, many repeated *I*-*V* sweeps are conducted in a vacuum chamber ($< 1\times10^{-7}$ Torr) for the samples which show random transitions at ambient conditions. All the active radicals are first detached from the channel by applying high currents through the graphene channel under a vacuum because of the thermal energy generated by current annealing. After removing all doping sources, the nonlinear random transitions have never been observed with more than 20 devices measured in a vacuum as shown in Fig. 7.3(a). When the device is exposed to air again, the random transitions are reinstated. From this result, it is clear that the observed phenomenon is strongly correlated to electrochemical reactions caused by active radicals which is attached and detached to the graphene channel from air. Similar phenomenon with a top gate structure has been reported observing reversible bipolar switching by applying electrochemical modification.[116] In this case, hydrogen and hydroxyl, catalytically produced in the silicon oxide top gate, work as chemical doping sources and devices did not exhibit the switching anymore under high vacuum conditions similar to our case.

In order to investigate any mechanical deformation or topological changes associated with the random transitions, material characterization techniques such as atomic force microscopy (AFM) and scanning electron microscopy (SEM) are employed to image the graphene channels. All imaging have been done after the transport measurements, since the

characterization may damage or change the graphene property. As can be seen from Fig. 7.3(b), the SEM image of the graphene channel is not flat and a topological change of graphene is observed. The mechanically deformed part which may induce a local strain due to an upheaval structure is clearly visible by the AFM measurement in Fig. 7.3(c). The current density between two terminals is usually higher than a few times 10^8 A/cm^2 at 3 V, when the device is in a metallic state. In this regime, it is reasonable to have electromigration and large Joule heating effects.[85] Heat dissipation more than a few mW may cause the topological change of graphene. We have investigated more than 300 exfoliated graphene and cannot observe any upheaval or local strain from the pristine exfoliated graphene. We can observe the deformed graphene channel only after measuring stochastic transitions, indicating that the deformed graphene is responsible for the random transitions. In order to support our assumption, we sweep the voltage in a small range (< 0.1 V) for more than 50 devices. Only typical ohmic *I-V* characteristics are measured rather than the nonlinear behavior, and no deformed graphene channel is found after the transport measurements. This is in line with previous studies, in which metal-semiconductor transition (MST) and metal-insulator transition has been observed from the two-terminal carbon nanotube (CNT) devices exposed to electron beam irradiation.[117, 118] Inhomogeneous electric fields generated from the trapped charges in SiO_2 are proposed to be the origin in this case.

We conclude that the observed random transition of graphene is attributed to unevenly attached active radicals, similarly working as the trapped charges to create inhomogenuous fields, in a non uniform graphene channel. Since our graphene channel is inhomogeneous, unevenly attached active radicals in graphene locally change the electrostatic potential. We have done transport simulations considering self-trapped electrons and holes in the upheaval graphene channel caused by electrochemical reactions. We consider the tight binding Hamiltonian of graphene cluster taking into account electron-electron interactions

$$H_G = -t\sum_{i,j,\sigma}(a_{i\sigma}^{+}b_{j\sigma} + b_{i\sigma}^{+}a_{j\sigma}) + U\sum_{i} n_i^{\uparrow} n_i^{\downarrow}\ , \qquad (1)$$

where t is the spin-independent effective hopping integral between the nearest-neighbour carbon atoms, U is the electron-electron interaction parameter, n^{σ}_i is the operator of number of electrons with spin σ, $a^{+}_{i\sigma}$ ($b^{+}_{i\sigma}$) and $a_{i\sigma}$ ($b_{i\sigma}$) are the creation and annihilation operators of the conduction electron with spin σ on site i on graphene sublattice A (B). We apply the Hartree-Fock approximation for the second term of eq.(1) and rewrite the Hamiltonian of the graphene cluster

$$H_G = -t\sum_{i,j,\sigma}(a_{i\sigma}^{+}b_{j\sigma} + b_{i\sigma}^{+}a_{j\sigma}) + \frac{U}{2}\sum_{i,\sigma}\left(\langle n_i\rangle - 1\right)(a_{i\sigma}^{+}b_{i\sigma} + b_{i\sigma}^{+}a_{i\sigma})\,, \qquad (2)$$

where $<n_i>$ is the average number of electrons on site i. For uncharged graphene $<n_i>=1$, while $<n_i>=2(0)$ if an extra electron (or hole) is on site i. The graphene cluster is coupled with two non-magnetic leads. The Hamiltonian of the device has the form

$$H = H_G + H_L + H_R + H_{GL} + H_{GR} + H.c.\,, \qquad (3)$$

where $H_{L/R}$ is the Hamiltonian of the left/right lead, and the term $H_{GL/GR}$ describes the coupling of the graphene cluster to the left/right lead. We calculate the electric current through the system, when voltage is applied across the devices. Our calculations are based on the non-equilibrium Green functions formalism. The details of the approach can be found elsewhere.[119] First we diagonalize H_G and find the retarded Green function of the uncoupled graphene cluster g^r. Next we find the retarded Green function of the coupled system by solving the Dyson equation

$$G^r = g^r + g^r\Sigma_L^r G^r + g^r\Sigma_R^r G^r\,, \qquad (4)$$

where $\Sigma^r_{L/R}$ is the retarded self-energy due to connection of the graphene cluster to the left/right lead. We assume that $\Sigma^r_{L/R}$ is independent of energy. The final expression for the charge current becomes

$$I = \frac{e}{h}\int d\varepsilon[\, f_L(\varepsilon) - f_R(\varepsilon)]Tr[G^a\Gamma_R G^r\Gamma_L], \tag{5}$$

where G^a is the advanced Green functions of the coupled system, $\Gamma_{L/R} = i(\Sigma^r_{L/R} - \Sigma^a_{L/R})$ and $f_{L/R}$ is the Fermi-Dirac distribution functions in the left/right lead. We calculate the *I-V* characteristics assuming that the charge distribution on the graphene surface randomly changes, when the applied voltage reaches the threshold value of 3 V. Based on this, we obtain the result of *I-V* traces, which is very similar to the experimental results, as plotted in Fig. 7.3(d). The inset in Fig. 7.3(d) shows the resistance as a function of simulation time. There are also random transitions among three switching phases as similar to the experimental data, which can be seen from Fig. 7.2.2(b). However, further studies are required for better understanding of the physical mechanism of the random transitions.

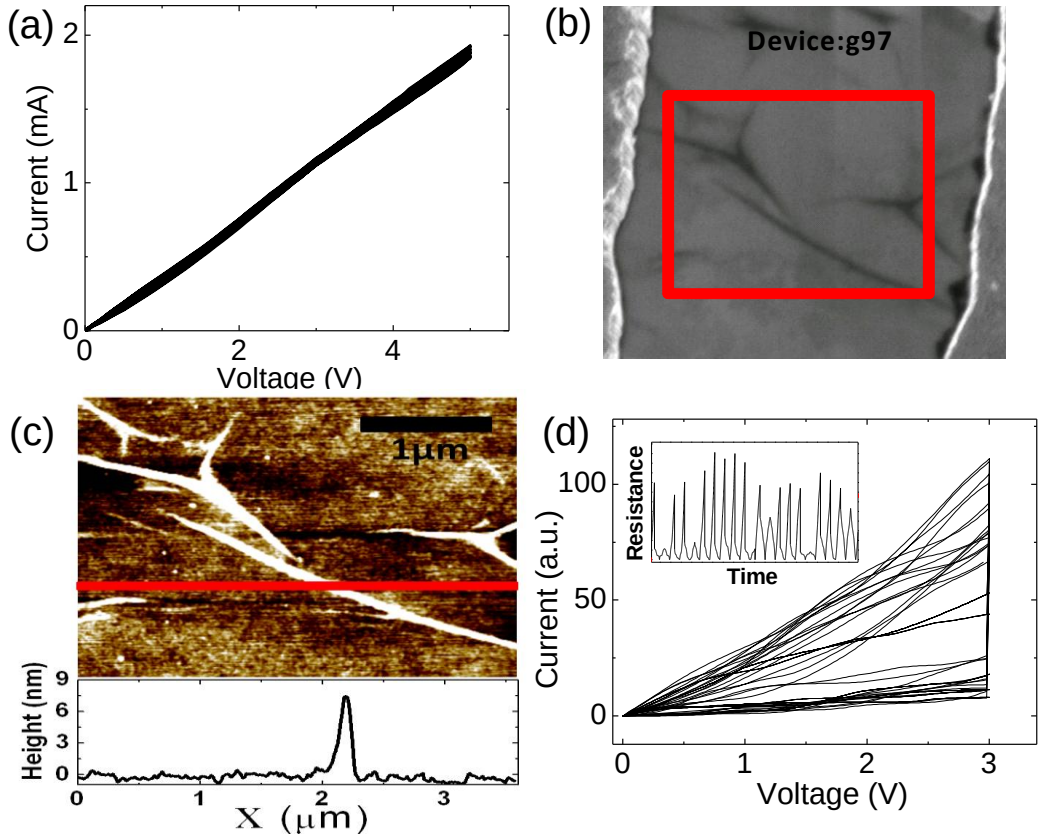

Figure 7.3 (a) *I-V* curves in vacuum. (b) A scanning electron microscopy image of graphene channel after observing stochastic transitions. (c) An atomic force microscopy image of graphene channel indicated as a red box in (b). The bottom figure is the line scan of the red line. (d) Simulated switching *I-V* curves. The inset in (d) shows Resistance as a function of simulation time.

7.4 Electrical Phase Change

Frequent breakdowns occur during the *I-V* sweeps because of a high electrical field used in the experiments. When the graphene channel becomes a mixed phase structure with *sp*2 and *sp*3 fractions, the tunneling characteristic becomes the main transport mechanism as can be seen in Fig. 7.4.[120] In our case the samples undergo the following breakdown

sequence such that the transport property changes from the ohmic to random transition, and then to tunneling, finally resulting in a complete breakdown (open circuit).

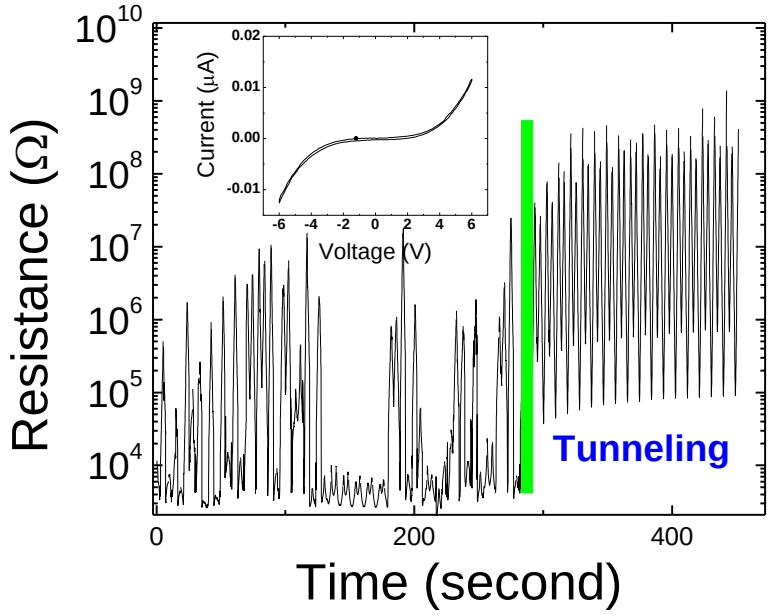

Figure 7.4 Resistance as a function of measurement time. The inset shows a typical *I-V* curve in the tunneling regime. The stochastic nonlinear switching behavior has been observed before the tunneling regime.

7.5 Controlled experiments

It was reported previously that mechanical discontinuity of graphene and graphitic nanoribbon can be the origin of the switching effect. We scrutinize all the samples which show random transitions with AFM and SEM very carefully and cannot find any mechanical discontinuity across the graphene channels. However, there are mechanical deformations. When the sweep voltage is higher than its saturation value, graphene devices are burnt rather than being discontinuous.[92]

In order to rule out other possibilities as the origin of the observed effect such as the current annealing effect and interface issues between graphene and contacts, the graphene devices are annealed under high vacuum conditions at 500 K for 2 hours. After annealing, a random hysteresis is still observed under ambient conditions. Since the electrical property of graphene is highly dependent on the level of defects, we intentionally introduce large defects into graphene by an oxygen plasma treatment and confirm the level of defect by Raman spectroscopy. Graphene is electrically annealed after the oxygen plasma treatment and electrical transport measurements have been conducted. Although the current hysteresis is found, the hysteresis is not repeatable and the value of the tolerable current is very small (order of several μA) as can be seen from Fig. 7.5.

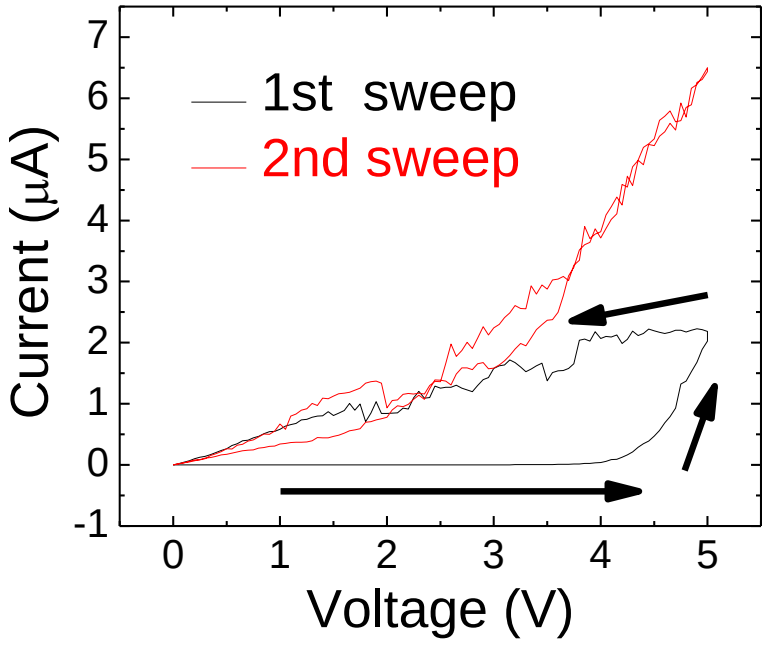

Figure 7.5 Experimental switching *I-V* curve of two-terminal graphene device after exposure to oxygen plasma.

7.6 Summary

In chapter 7, it presents stochastic transitions between an ohmic like state and an insulator like state in graphene devices. The topological change in the graphene channel is involved for the origin of the random transitions. Active radicals with topologically non-uniform graphene channel cause a local change of electrostatic potential, and simulations based on the self-trapped electron and hole mechanism can account for the random transitions. Further, investigations may open up a promising way to engineer graphene memories and logic devices with a high ON/OFF ratio.

8. Conclusion and Future Works

8.1 Summary

Carbon nanotube, the big brother of graphene was first reported in 1991. CNT attracted enormous attentions due to its outstanding physical properties and numerous papers have been reporting its superior properties. At that time, this one dimensional material was the hero in nanotechnology and was believed to provoke a revolution in electronics. Although there have been huge number of trials for developing new electronics with CNT, CNT is difficult to advance further than pro-types in the laboratories. Two factors limit the usage of CNTs in real electronics applications. First, selective growth of purely metallic or semiconducting CNT is difficult. Second, aligning all CNTs to certain directions is extremely challenging. Therefore, it seems that only applicable way to engineer CNTs is to use its network structure. Since the charge carrier in nanotubes should hop from one nanotube to others, the good electrical properties of CNTs cannot be fully utilized. However, graphene is making a new history different from CNTs. Although it might be difficult for graphene to be utilized for logic or memory devices due to its semi-metallic property, graphene can be a good candidate to replace ITO because of the superior optical and electrical properties. Large-scale graphene can be synthesized by adopting the roll to roll method. The uniformity of graphene should still be improved and more economical process should be developed in order for graphene to be more competitive than ITO and other transparent materials. Since lighter, stronger and flexible displays are demanded by the market, graphene can be commercialized as soon as its mass production becomes available.

It is obvious that a better electrical performance can be obtained, when higher quality graphene devices are achieved. We have studied the surface property of graphene in order to make better contacts between graphene and metal. To understand the surface property of graphene, the wettability of epitaxial graphene on SiC has been investigated by contact angle

measurements. A monolayer of epitaxial graphene shows a hydrophobic characteristic and no correlation are found between different layers of graphene and wettability. Upon oxygen plasma treatment, defects are introduced into graphene, and the level of damage is investigated by Raman spectroscopy. There exists a correlation between the level of defects and the contact angle. As more defects are induced, the surface energy of graphene is increased, leading to the hydrophilic nature. Plasma treatment with optimized power and duration has been proposed to control the adhesion properties for contact fabrication. Choi *et al.* has reported that fabrication yield ratio of metal contacts on graphene is much improved without degrading electrical property of graphene after applying plasma engineering [93].

After understanding surface properties, electrical properties of graphene are investigated. Since most of graphene research has focused on only low temperature measurement with low bias to find out its physical properties, we investigate thoroughly graphene devices with high bias, which is very similar to operational voltage of commercialized electronics. Reproducible current hysteresis is observed, when high voltage bias is swept in the graphene channel. We observe that the sequence of hysteresis switching with different types of the carriers, n-type and p-type, is inverted and we propose that charging and discharging effect is responsible for the observed ambipolar switching effect supported by quantum simulations.

After studying ambipolar hysteresis of graphene, we study the hysteresis of the top gated bilayer graphene field effect transistors. Capacitance - voltage measurements on top gated bilayer graphene indicates that the origin of hysteresis in the channel resistance is due to charge traps present in the graphene/Al_2O_3 interface with a charging and discharging time constant of ~100 μs. On the other hand, the measured capacitance of graphene between source and drain with source-drain voltage does not show any hysteresis. It is also found that the hysteresis is present even at high vacuum conditions and cryogenic temperatures

indicating that chemical attachment is not the main source of the hysteresis. The hysteresis is not due to Joule heating effect, but is a function of the level of the applied voltage.

Tunneling characteristic of graphene from the two-terminal devices after the breakdown is studied. A negative differential conductance is also observed, when a high voltage bias is applied across the graphene channel. The tunneling behavior could be attributed to the formation of nonuniform disordered graphene, which is created by the breakdown. We propose that the nonuniform disordered structure can introduce energy barriers in the graphene channel. This hypothesis is supported by the Raman images and the simulated results of the *I-V* characteristics from a one dimensional single-square barrier. A 2 nm thick glassy carbon film, which is uniformly disordered, is compared and linear *I-V* characteristics of grassy carbon prove that the tunneling characteristic is a unique property of nonuniform disordered graphene. The observed memory switching effect up to a 100000% ON/OFF ratio may open up new possibilities for various graphene based applications and the tunneling effect paves a way to study disordered graphene characteristics such as defect magnetism or a weak localization in graphene.

Stochastic transitions between an ohmic like state and an insulator like state in graphene devices are studied. It is found that the topological change in the graphene channel is involved for the observed behavior. Active radicals with an uneven graphene channel cause a local change of electrostatic potential, and simulations based on the self-trapped electron and hole mechanism can account for the observed data. Understanding electrical transport of graphene at room temperature and at high bias voltages is very important for the interconnect and transparent contact applications.

8.2 Suggestions for Future Works

The latest edition of the ITRS has introduced graphene devices in the scope of emerging research devices. This means graphene has some potential for future applications, even though it is currently immature from the point of view of engineering. It should be emphasized that graphene itself is not a device, but is a material. Graphene can be transformed to many different forms. Therefore, there are enormous opportunities which can be pioneered in the graphene world. The followings are some feasible ideas for future researches.

All-graphene integrated circuit is very promising, because graphene can support very high current densities greater than 10^8 Acm^{-2}, and the band gap of graphene can be opened by local nanoribbon patterning.[120] For example, the modern display industries use both silicon and ITO. Using graphene as interconnects and channel for display devices can be very competitive to over the modern flexible and transparent display devices.

Radiofrequency graphene devices have high potential due to graphene's outstanding mobility. So far, the measured highest cutoff frequency is 300 GHz from graphene transistors with a nanowire gate.[30] Even though the best record has been achieved from the nanowire gates, it seems it is unsuitable for future commercialization because of very tricky fabrication processes. Using CVD and epitaxial graphene, cutoff frequencies more than 100 GHz have been accomplished with especially wafer scale devices made by conventional CMOS fabrication methods. However, there is still much room which can be improved.[29] The key value to enhance radiofrequency performance is definitely mobility. For instance, with graphene transistors encapsulated with h-BN, the mobility can increase because the scattering by optical phonon of the SiO_2 can be reduced, leading to the improvement of radiofrequency performance.

The optical properties of graphene are as impressive as its electrical properties. Engineering graphene in optoelectronics is another promising area.[49] For example, ultrafast photodetector with the graphene channel has been achieved. Experimental results suggest that the intrinsic bandwidth of graphene photodetector may exceed 500 GHz. Graphene light emitting devices have not been engineered yet.[48] By patterning graphene nanoribbon, the band gap can be opened, and hole and electron recombination can be generated by electrical doping with dual gates. Since far infrared CNT LEDs have been engineered successfully, nanoribbon graphene LED should be able to be engineered as well. Graphene LEDs have more advantages then CNT, because the band gap can be tunable by patterning with different width and graphene is much friendlier with the conventional semiconductor fabrication method.[121]

References

[1] Geim AK, Novoselov KS. The Rise of Graphene. Nature Materials. 2007;6(3):183.

[2] Kosynkin DV, Higginbotham AL, Sinitskii A, Lomeda JR, Dimiev A, Price BK, et al. Longitudinal Unzipping of Carbon Nanotubes to Form Graphene Nanoribbons. Nature. 2009;458(7240):872.

[3] Novoselov KS, Geim AK, Morozov SV, Jiang D, Zhang Y, Dubonos SV, et al. Electric Field Effect in Atomically Thin Carbon Films. Science. 2004;306(5696):666.

[4] Novoselov KS, Geim AK, Morozov SV, Jiang D, Katsnelson MI, Grigorieva IV, et al. Two-Dimensional Gas of Massless Dirac Fermions in Graphene. Nature. 2005;438(7065):197.

[5] Zhang YB, Tan YW, Stormer HL, Kim P. Experimental Observation of the Quantum Hall Effect and Berry's Phase in Graphene. Nature. 2005 ;438(7065):201.

[6] Katsnelson MI, Novoselov KS, Geim AK. Chiral Tunnelling and the Klein Paradox in Graphene. Nature Physics. 2006;2(9):620.

[7] Novoselov KS, McCann E, Morozov SV, Fal'ko VI, Katsnelson MI, Zeitler U, et al. Unconventional Quantum Hall Effect and Berry's Phase of 2 π in Bilayer Graphene. Nature Physics. 2006;2(3):177.

[8] Berger C, Song Z, Li X, Wu X, Brown N, Naud C, et al. Electronic Confinement and Coherence in Patterned Epitaxial Graphene. Science. 2006;312(5777):1191.

[9] Han TH, Lee YB, Woo SH, Bae SH, Hong BH, Ahn JH, Lee TW. Extremely Efficient Flexible Organic Light-Emitting Diode with Modified Graphene Anode. Nature Photonics. 2012;6(1038):105.

[10] Miao F, Wijeratne S, Zhang Y, Coskun UC, Bao W, Lau CN. Phase-Coherent Transport in Graphene Quantum Billiards. Science. 2007;317(5844):1530.

[11] Tan YW, Zhang Y, Bolotin K, Zhao Y, Adam S, Hwang EH, et al. Measurement of Scattering Rate and Minimum Conductivity in Graphene. Physical Review Letters. 2007;99(24):246803.

[12] Novoselov K, Geim A. Graphene Detects Single Molecule of Toxic Gas. Materials Technology. 2007;22(3):178.

[13] Williams JR, DiCarlo L, Marcus CM. Quantum Hall Effect in a Gate-Controlled p-n Junction of Graphene. Science. 2007;317(5838):638.

[14] Castro EV, Novoselov KS, Morozov SV, Peres NMR, Dos Santos J, Nilsson J, et al. Biased bilayer graphene: Semiconductor with a Gap Tunable By the Electric Field Effect. Physical Review Letters. 2007;99(21): 216802.

[15] Elias DC, Nair RR, Mohiuddin TMG, Morozov SV, Blake P, Halsall MP, et al. Control of Graphene's Properties by Reversible Hydrogenation: Evidence for Graphane. Science. 2009 Jan;323(5914):610.

[16] Wang ZF, Zheng HX, Shi QW, Chen J, Ieee. Emerging Nanocircuit Paradigm: Graphene-Based Electronics for Nanoscale Computing. IEEE International Symposium on Nanoscale Architecture; 2007;93.

[17] Chen JH, Jang C, Xiao SD, Ishigami M, Fuhrer MS. Intrinsic and Extrinsic Performance Limits of Graphene Devices on SiO_2. Nature Nanotechnology. 2008;3(4):206.

[18] Tsen AW, Brown L, Levendorf MP, Ghahari F, Huang PY, Havener RW, et al. Tailoring Electrical Transport Across Grain Boundaries in Polycrystalline Graphene. Science. 2012;336(6085):1143.

[19] Meric I, Han MY, Young AF, Ozyilmaz B, Kim P, Shepard KL. Current Saturation in Zero-Bandgap, Top-Gated Graphene Field-Effect Transistors. Nature Nanotechnology. 2008;3(11):654.

[20] Geim AK. Graphene: Status and Prospects. Science. 2009;324(5934):1530.

[21] Castro Neto AH, Guinea F, Peres NMR, Novoselov KS, Geim AK. The Electronic Properties of Graphene. Reviews of Modern Physics. 2009;81(1):109.

[22] Balandin AA, Ghosh S, Bao WZ, Calizo I, Teweldebrhan D, Miao F, et al. Superior Thermal Conductivity of Single-Layer Graphene. Nano Letters. 2008;8(3):902.

[23] Lee C, Wei XD, Kysar JW, Hone J. Measurement of the Elastic Properties and Intrinsic Strength of Monolayer Graphene. Science. 2008;321(5887):385.

[24] Shin YJ, Stromberg R, Nay R, Huang H, Wee ATS, Yang H, et al. Frictional Characteristics of Exfoliated and Epitaxial Graphene. Carbon. 2011;49(12):4070.

[25] Bolotin KI, Sikes KJ, Hone J, Stormer HL, Kim P. Temperature-Dependent Transport in Suspended Graphene. Physical Review Letters. 2008;101(9):096802.

[26] Bolotin KI, Sikes KJ, Jiang Z, Klima M, Fudenberg G, Hone J, et al. Ultrahigh Electron Mobility in Suspended Graphene. Solid State Communications. 2008;146(9-10):351.

[27] Wu YQ, Lin YM, Bol AA, Jenkins KA, Xia FN, Farmer DB, et al. High-Frequency, Scaled Graphene Transistors on Diamond-like Carbon. Nature. 2011;472(7341):74.

[28] Bonaccorso F, Sun Z, Hasan T, Ferrari AC. Graphene Photonics and Optoelectronics. Nature Photonics. 2010;4(9):611.

[29] Lin YM, Dimitrakopoulos C, Jenkins KA, Farmer DB, Chiu HY, Grill A, et al. 100-GHz Transistors from Wafer-Scale Epitaxial Graphene. Science. 2010;327(5966):662.

[30] Liao L, Lin YC, Bao MQ, Cheng R, Bai JW, Liu YA, et al. High-Speed Graphene Transistors With a Self-aligned Nanowire Gate. Nature. 2010;467(7313):305.

[31] Bae S, Kim H, Lee Y, Xu X, Park J-S, Zheng Y, et al. Roll-to-roll production of 30-inch Graphene Films for Transparent Electrodes. Nature Nanotechnology. 2010;5(8):574.

[32] Geim AK, MacDonald AH. Graphene: Exploring Carbon Flatland. Physics Today. 2007;60(8):35.

[33] Chen JH, Jang C, Adam S, Fuhrer MS, Williams ED, Ishigami M. Charged-Impurity Scattering in Graphene. Nature Physics. 2008;4(5):377.

[34] Meyer JC, Geim AK, Katsnelson MI, Novoselov KS, Booth TJ, Roth S. The Structure of Suspended Graphene Sheets. Nature. 2007;446(7131):60.

[35] Dean CR, Young AF, Meric I, Lee C, Wang L, Sorgenfrei S, et al. Boron Nitride Substrates for High-Quality Graphene Electronics. Nature Nanotechnology. 2010;5(10):722.

[36] Mayorov AS, Gorbachev RV, Morozov SV, Britnell L, Jalil R, Ponomarenko LA, et al. Micrometer-Scale Ballistic Transport in Encapsulated Graphene at Room Temperature. Nano Letters. 2011;11(6):2396.

[37] Giovannetti G, Khomyakov PA, Brocks G, Kelly PJ, van den Brink J. Substrate-induced Band Gap in Graphene on Hexagonal Boron Nitride: Ab initio Density Functional Calculations. Physical Review B. 2007;76(7) 096802.

[38] Huang PY, Ruiz-Vargas CS, van der Zande AM, Whitney WS, Levendorf MP, Kevek JW, et al. Grains and Grain Boundaries in Single-Layer Graphene Atomic Patchwork quilts. Nature. 2011;469(7330):389.

[39] Ohta T, Bostwick A, Seyller T, Horn K, Rotenberg E. Controlling the Electronic Structure of Bilayer Graphene. Science. 2006;313(5789):951.

[40] Han MY, Ozyilmaz B, Zhang YB, Kim P. Energy Band-gap Engineering of Graphene Nanoribbons. Physical Review Letters. 2007;98(20) 187401.

[41] Raza H, Kan EC. Armchair Graphene Nanoribbons: Electronic Structure and Electric-Field Modulation. Physical Review B. 2008;77(24):245434.

[42] Akturk A, Goldsman N. Electron Transport and Full-Band Electron-Phonon Interactions in Graphene. Journal of Applied Physics. 2008;103(5):2890147.

[43] Cervantes-Sodi F, Csanyi G, Piscanec S, Ferrari AC. Edge-Functionalized and Substitutionally Doped Graphene Nanoribbons: Electronic and Spin Properties. Physical Review B. 2008;77(16) 165427.

[44] Schwierz F. Graphene transistors. Nature Nanotechnology. 2010;5(7):487.

[45] Yang H, Heo J, Park S, Song HJ, Seo DH, Byun KE, et al. Graphene Barristor, a Triode Device with a Gate-Controlled Schottky Barrier. Science. 2012;336(6085):1140.

[46] Kuzmenko AB, van Heumen E, Carbone F, van der Marel D. Universal Optical Conductance of Graphite. Physical Review Letters. 2008;100(11):117401.

[47] Nair RR, Blake P, Grigorenko AN, Novoselov KS, Booth TJ, Stauber T, et al. Fine Structure Constant Defines Visual Transparency of Graphene. Science. 2008;320(5881):1308.

[48] Xia FN, Mueller T, Lin YM, Valdes-Garcia A, Avouris P. Ultrafast Graphene Photodetector. Nature Nanotechnology. 2009;4(12):839.

[49] Sensale-Rodriguez B, Yan RS, Kelly MM, Fang T, Tahy K, Hwang WS, et al. Broadband Graphene Terahertz Modulators Enabled by Intraband Transitions. Nature Communications. 2012 ;3:780.

[50] Bunch JS, van der Zande AM, Verbridge SS, Frank IW, Tanenbaum DM, Parpia JM, et al. Electromechanical Resonators from Graphene Sheets. Science. 2007;315(5811):490.

[51] Yan Z, Liu G, Khan JM, Balandin AA. Graphene Quilts for Thermal Management of High-Power GaN Transistors. Nature Communications. 2012;3:827.

[52] Hecht DS, Hu L, Irvin G. Emerging Transparent Electrodes Based on Thin Films of Carbon Nanotubes, Graphene, and Metallic Nanostructures. Advanced Materials. 2011;23(13):1482.

[53] Blake P, Hill EW, Neto AHC, Novoselov KS, Jiang D, Yang R, et al. Making Graphene Visible. Applied Physics Letters. 2007;91(6)2768624.

[54] Eda G, Fanchini G, Chhowalla M. Large-area Ultrathin Films of Reduced Graphene Oxide as a Transparent and Flexible Electronic Material. Nature Nanotechnology. 2008;3(5):270.

[55] Kim KS, Zhao Y, Jang H, Lee SY, Kim JM, Ahn JH, et al. Large-Scale Pattern Growth of Graphene Films for Stretchable Transparent Electrodes. Nature. 2009;457(7230):706.

[56] Li XS, Cai WW, An JH, Kim S, Nah J, Yang DX, et al. Large-Area Synthesis of High-Quality and Uniform Graphene Films on Copper Foils. Science. 2009;324(5932):1312.

[57] Kwak J, Chu JH, Choi JK, Park SD, Go H, Kim SY, et al. Near Room-Temperature Synthesis of Transfer-free Graphene Films. Nature Communications. 2012;3:645.

[58] Eklund PC, Holden JM, Jishi RA. Vibrationals-Modes of Carbon Nanotubes - Spectroscopy and Theory. Carbon. 1995;33(7):959.

[59] Robertson J. Diamond-like Amorphous Carbon. Materials Science & Engineering R-Reports. 2002;37(4-6):129.

[60] Ferrari AC, Meyer JC, Scardaci V, Casiraghi C, Lazzeri M, Mauri F, et al. Raman Spectrum of Graphene and Graphene Layers. Physical Review Letters. 2006;97(18):187401.

[61] Hao Y, Wang Y, Wang L, Ni Z, Wang Z, Wang R, et al. Probing Layer Number and Stacking Order of Few-Layer Graphene by Raman Spectroscopy. Small. 2010;6(2):195.

[62] Cuomo JJ, Pappas DL, Bruley J, Doyle JP, Saenger KL. Vapor-Depostions Processes for Amorphous-Carbon Films with sp3 Fractions Approaching Diamond. Journal of Applied Physics. 1991;70(3):1706.

[63] Ferrari AC, Robertson J. Interpretation of Raman Spectra of Disordered and Amorphous Carbon. Physical Review B. 2000;61(20):14095.

[64] Kim DC, Jeon DY, Chung HJ, Woo Y, Shin JK, Seo S. The Structural and Electrical Evolution of Graphene by Oxygen Plasma-induced Disorder. Nanotechnology. 2009; 20(37):375703.

[65] Kalon G, Shin YJ, Truong VG, Kalitsov A, Yang H. The Role of Charge Traps in Inducing Hysteresis: Capacitance-Voltage Measurements on Top Gated Bilayer Graphene. Applied Physics Letters. 2011;99(8):083109.

[66] Dlubak B, Seneor P, Anane A, Barraud C, Deranlot C, Deneuve D, et al. Are Al(2)O(3) and MgO Tunnel Barriers Suitable for Spin Injection in Graphene? Applied Physics Letters. 2010;97(9):092502.

[67] Parkin SSP, Kaiser C, Panchula A, Rice PM, Hughes B, Samant M, et al. Giant Tunnelling Magnetoresistance at Room Temperature with MgO (100) Tunnel Barriers. Nature Materials. 2004;3(12):862.

[68] Maneshian MH, Kuo FL, Mahdak K, Hwang J, Banerjee R, Shepherd ND. The Influence of High Dielectric Constant Aluminum Oxide Sputter Deposition on the Structure and Properties of Multilayer Epitaxial Graphene. Nanotechnology. 2011;22(20):7.

[69] Ni ZH, Wang HM, Ma Y, Kasim J, Wu YH, Shen ZX. Tunable Stress and Controlled Thickness Modification in Graphene by Annealing. ACS Nano. 2008;2(5):1033.

[70] Huang H, Chen W, Chen S, Wee ATS. Bottom-up Growth of Epitaxial Graphene on 6H-SiC(0001). ACS Nano. 2008;2(12):2513.

[71] Ni ZH, Wang HM, Kasim J, Fan HM, Yu T, Wu YH, et al. Graphene Thickness Determination Using Reflection and Contrast Spectroscopy. Nano Letters. 2007;7(9):2758.

[72] Ni ZH, Chen W, Fan XF, Kuo JL, Yu T, Wee ATS, et al. Raman Spectroscopy of Epitaxial Graphene on a SiC Substrate. Physical Review B. 2008;77(11):115416.

[73] Filleter T, McChesney JL, Bostwick A, Rotenberg E, Emtsev KV, Seyller T, et al. Friction and Dissipation in Epitaxial Graphene Films. Physical Review Letters. 2009 ;102(8):086102.

[74] Zhang YB, Tang TT, Girit C, Hao Z, Martin MC, Zettl A, et al. Direct Observation of a Widely Tunable Bandgap in Bilayer Graphene. Nature. 2009;459(7248):820.

[75] Wang SR, Zhang Y, Abidi N, Cabrales L. Wettability and Surface Free Energy of Graphene Films. Langmuir. 2009;25(18):11078.

[76] Feng XJ, Jiang L. Design and Creation of Superwetting/Antiwetting Surfaces. Advanced Materials. 2006;18(23):3063.

[77] Wenzel RN. Resistance of Solid Surfaces to Wetting by Water. Industrial & Engineering Chemistry. 1936;28(8):988.

[78] Kanta A, Sedev R, Ralston J. Thermally and Photoinduced Changes in the Water Wettability of Low-Surface-Area Silica and Titania. Langmuir. 2005;21(6):2400.

[79] Walther F, Davydovskaya P, Zucher S, Kaiser M, Herberg H, Gigler AM, et al. Stability of the Hydrophilic Behavior of Oxygen Plasma Activated SU-8. Journal of Micromechanics and Microengineering. 2007;17(3):524.

[80] Liu L, Ryu SM, Tomasik MR, Stolyarova E, Jung N, Hybertsen MS, et al. Graphene Oxidation: Thickness-dependent Etching and Strong Chemical Doping. Nano Letters. 2008;8(7):1965.

[81] Norimatsu W, Kusunoki M. Transitional Structures of the Interface Between Graphene and 6H-SiC (0001). Chemical Physics Letters. 2009;468(1-3):52.

[82] Kim S, Ihm J, Choi HJ, Son YW. Origin of Anomalous Electronic Structures of Epitaxial Graphene on Silicon Carbide. Physical Review Letters. 2008;100(17):176802.

[83] Liang X, Fu Z, Chou SY. Graphene Transistors Fabricated via Transfer-Printing in device Active-Areas on Large Wafer. Nano Letters. 2007;7(12):3840.

[84] Shin YJ, Wang Y, Huang H, Kalon G, Wee ATS, Shen Z, et al. Surface-Energy Engineering of Graphene. Langmuir. 2010;26(6):3798.

[85] Moser J, Barreiro A, Bachtold A. Current-Induced Cleaning of Graphene. Applied Physics Letters. 2007;91(16):2789673.

[86] Zhou YB, Han BH, Liao ZM, Zhao Q, Xu J, Yu DP. Effect of Contact Barrier on Electron Transport in Graphene. Journal of Chemical Physics. 2010;132(2):3292029.

[87] Levendorf MP, Ruiz-Vargas CS, Garg S, Park J. Transfer-Free Batch Fabrication of Single Layer Graphene Transistors. Nano Letters. 2009;9(12):4479.

[88] Yang JJ, Pickett MD, Li XM, Ohlberg DAA, Stewart DR, Williams RS. Memristive switching mechanism for metal/oxide/metal nanodevices. Nature Nanotechnology. 2008;3(7):429.

[89] Datta S. Quantum Transport: Atom to Transistor: Cambridge 2005.

[90] Datta S. Electrical Resistance: An Atomistic View. Nanotechnology. 2004;15:S433.

[91] Yao J, Jin Z, Zhong L, Natelson D, Tour JM. Two-Terminal Nonvolatile Memories Based on Single-Walled Carbon Nanotubes. ACS Nano. 2009;3(12):4122.

[92] Shin YJ, Kalon G, Son J, Kwon JH, Niu J, Bhatia CS, et al. Tunneling Characteristics of Graphene. Applied Physics Letters. 2010;97(25):252102.

[93] Choi MS, Lee SH, Yoo WJ. Plasma Treatments to Improve Metal Contacts in Graphene Field Effect Transistor. Journal of Applied Physics. 2011;110(7):073305

[94] Martin J, Akerman N, Ulbricht G, Lohmann T, Smet JH, Von Klitzing K, et al. Observation of Electron-Hole Puddles in Graphene Using a Scanning Single-Electron Transistor. Nature Physics. 2008;4(2):144.

[95] Tan YW, Zhang Y, Bolotin K, Zhao Y, Adam S, Hwang EH, et al. Measurement of Scattering Rate and Minimum Conductivity in Graphene. Physical Review Letters. 2007;99(24):246803.

[96] Yan J, Henriksen EA, Kim P, Pinczuk A. Observation of Anomalous Phonon Softening in Bilayer Graphene. Physical Review Letters. 2008;101(13):136804.

[97] Shin YJ, Kwon JH, Kalon G, Lam KT, Bhatia CS, Liang G, et al. Ambipolar Bistable Switching Effect of Graphene. Applied Physics Letters. 2010;97(26):262105.

[98] Joshi P, Romero HE, Neal AT, Toutam VK, Tadigadapa SA. Intrinsic Doping and Gate Hysteresis in Graphene Field Effect Devices Fabricated on SiO2 Substrates. Journal of Physics:Condensed Matter. 2010;22(33):334214.

[99] Lafkioti M, Krauss B, Lohmann T, Zschieschang U, Klauk H, von Klitzing K, et al. Graphene on a Hydrophobic Substrate: Doping Reduction and Hysteresis Suppression under Ambient Conditions. Nano Letters. 2010;10(4):1149.

[100] Wang HM, Wu YH, Cong CX, Shang JZ, Yu T. Hysteresis of Electronic Transport in Graphene Transistors. ACS Nano. 2010;4(12):7221.

[101] Lee YG, Kang CG, Jung UJ, Kim JJ, Hwang HJ, Chung HJ, et al. Fast Transient Charging at the Graphene/SiO_2 Interface Causing Hysteretic Device Characteristics. Applied Physics Letters. 2011;98(18):183508.

[102] Choi R, Song SC, Young CD, Bersuker G, Lee BH. Charge Trapping and Detrapping Characteristics in Hafnium Silicate Gate Dielectric Using an Inversion Pulse Measurement Technique. Applied Physics Letters. 2005;87(12):122901.

[103] Li L, Richter C, Paetel S, Kopp T, Mannhart J, Ashoori RC. Very Large Capacitance Enhancement in a Two-Dimensional Electron System. Science. 2011;332(6031):825.

[104] Abergel DSL, Hwang EH, Das Sarma S. Compressibility of Graphene. Physical Review B. 2011;83(8):085429.

[105] Kalon G, Shin YJ, Yang H. Tunable Metal-Insulator Transitions in Bilayer Graphene by Thermal Annealing. Applied Physics Letters. 2011;98(23):233108.

[106] Barreiro A, Lazzeri M, Moser J, Mauri F, Bachtold A. Transport Properties of Graphene in the High-Current Limit. Physical Review Letters. 2009;103(7):076601.

[107] Pop E, Mann D, Cao J, Wang Q, Goodson K, Dai H. Negative Differential Conductance and Hot Phonons in Suspended Nanotube Molecular Wires. Physical Review Letters. 2005;95(15):155505.

[108] Murali R, Yang Y, Brenner K, Beck T, Meindl JD. Breakdown Current Density of Graphene Nanoribbons. Applied Physics Letters. 2009;94(24):243114.

[109] Waser R, Aono M. Nanoionics-based Resistive Switching Memories. Nature Materials. 2007;6(11):833.

[110] Wang HL, Wang XR, Li XL, Dai HJ. Chemical Self-Assembly of Graphene Sheets. Nano Research. 2009;2(4):336.

[111] Standley B, Bao W, Zhang H, Bruck J, Lau CN, Bockrath M. Graphene-Based Atomic-Scale Switches. Nano Letters. 2008;8(10):3345.

[112] Li Y, Sinitskii A, Tour JM. Electronic two-terminal bistable graphitic memories. Nature Materials. 2008;7(12):966.

[113] Collins PG, Hersam M, Arnold M, Martel R, Avouris P. Current Saturation and Electrical Breakdown in Multiwalled Carbon Nanotubes. Physical Review Letters. 2001;86(14):3128.

[114] Pinto S, Krishna R, Dias C, Pimentel G, Oliveira GNP, Teixeira JM, et al. Resistive Switching and Activity-dependent Modification in Ni-doped Graphene Oixde Thin Films. 2012;101(6):063104.

[115] Late J, Liu B, Ramakrishna H, Dravid V, Rao CNR. Hysteresis in Single-layer MoS_2 Field Effect Transistors. 2012;6(6):5635.

[116] Echtermeyer TJ, Lemme MC, Baus M, Szafranek BN, Geim AK, Kurz H. Nonvolatile Switching in Graphene Field-Effect Devices. IEEE Electron Device Letters. 2008;29(8):952.

[117] Vijayaraghavan A, Kanzaki K, Suzuki S, Kobayashi Y, Inokawa H, Ono Y, et al. Metal−Semiconductor Transition in Single-Walled Carbon Nanotubes Induced by Low-Energy Electron Irradiation. Nano Letters. 2005;5(8):1575.

[118] Marquardt CW, Dehm S, Vijayaraghavan A, Blatt S, Hennrich F, Krupke R. Reversible Metal−Insulator Transitions in Metallic Single-Walled Carbon Nanotubes. Nano Letters. 2008 2008;8(9):2767.

[119] Meir Y, Wingreen NS. Landauer Formula for the Current Through an Interacting Electron Region. Physical Review Letters. 1992;68(16):2512.

[120] Lin YM, Valdes-Garcia A, Han SJ, Farmer DB, Meric I, Sun YN, et al. Wafer-Scale Graphene Integrated Circuit. Science. 2011;332(6035):1294.

[121] Mann D, Kato YK, Kinkhabwala A, Pop E, Cao J, Wang X, et al. Electrically Driven Thermal Light Emission from Individual Single-walled Carbon Nanotubes. Nature Nanotechnology. 2007;2(1):33.